







<b>Title</b>	<b>The Herschel Planetary Nebula Survey (HerPlaNS): A Comprehensive Dusty Photoionization Model of NGC6781</b>
<b>Author(s)</b>	<b>Otsuka, M; Ueta, T; van Hoof, PAM; Sahai, R; Aleman, I; Zijlstra, AA; Chu, YH; Villaver, E; Leal-Ferreira, ML; Kastner, J; Szczerba, R; Exter, KM</b>
<b>Citation</b>	<b>The Astrophysical Journal Supplement Series, 2017, v. 231 n. 2, p. 22:1-29</b>
<b>Issued Date</b>	<b>2017</b>
<b>URL</b>	<b><a href="http://hdl.handle.net/10722/245189">http://hdl.handle.net/10722/245189</a></b>
<b>Rights</b>	<b>The Astrophysical Journal Supplement Series. Copyright © American Astronomical Society.; This work is licensed under a Creative Commons Attribution-NonCommercial-NoDerivatives 4.0 International License.</b>



# The *Herschel* Planetary Nebula Survey (HerPlaNS): A Comprehensive Dusty Photoionization Model of NGC6781\*

Masaaki Otsuka<sup>1</sup> , Toshiya Ueta<sup>2</sup>, Peter A. M. van Hoof<sup>3</sup>, Raghvendra Sahai<sup>4</sup>, Isabel Aleman<sup>5</sup>, Albert A. Zijlstra<sup>6,7</sup> , You-Hua Chu<sup>1</sup>, Eva Villaver<sup>8</sup> , Marcelo L. Leal-Ferreira<sup>9</sup>, Joel Kastner<sup>10</sup> , Ryszard Szczerba<sup>11</sup>, and Katrina M. Exter<sup>12</sup>

<sup>1</sup> Institute of Astronomy and Astrophysics, 11F of Astronomy-Mathematics Building, AS/NTU. No.1, Section 4, Roosevelt Rd., Taipei 10617, Taiwan, ROC; [otsuka@asiaa.sinica.edu.tw](mailto:otsuka@asiaa.sinica.edu.tw)

<sup>2</sup> Department of Physics and Astronomy, University of Denver, 2112 E. Wesley Ave., Denver, CO 80210, USA

<sup>3</sup> Royal Observatory of Belgium, Ringlaan 3, B-1180, Brussels, Belgium

<sup>4</sup> Jet Propulsion Laboratory, 4800 Oak Grove Dr., Pasadena, CA 91109, USA

<sup>5</sup> Instituto de Astronomia, Geofísica e Ciências Atmosféricas (IAG-USP), Universidade de São Paulo, Cidade Universitária, Rua do Matão 1226, São Paulo, SP, 05508-090, Brazil

<sup>6</sup> Jodrell Bank Centre for Astrophysics, Alan Turing Building, University of Manchester, Manchester, M13 9PL, UK

<sup>7</sup> Department of Physics & Laboratory for Space Research, University of Hong Kong, Pok Fu Lam Rd., Hong Kong

<sup>8</sup> Departamento de Física Teórica, Universidad Autónoma de Madrid, Cantoblanco, E-28049, Madrid, Spain

<sup>9</sup> Leiden Observatory, Universiteit Leiden, P.O. Box 9513, NL-2300 RA Leiden, Netherlands

<sup>10</sup> Chester F. Carlson Center for Imaging Science and Laboratory for Multiwavelength Astrophysics,

Rochester Institute of Technology, 54 Lomb Memorial Dr., Rochester, NY, 14623, USA

<sup>11</sup> N. Copernicus Astronomical Centre Rabianska 8, 87–100 Torun, Poland

<sup>12</sup> Instituut voor Sterrenkunde, Katholieke Universiteit Leuven, Celestijnenlaan 200D, B-3001, Leuven, Belgium

Received 2017 April 12; revised 2017 July 19; accepted 2017 July 19; published 2017 August 18

## Abstract

We perform a comprehensive analysis of the planetary nebula (PN) NGC 6781 to investigate the physical conditions of each of its ionized, atomic, and molecular gas and dust components and the object's evolution, based on panchromatic observational data ranging from UV to radio. Empirical nebular elemental abundances, compared with theoretical predictions via nucleosynthesis models of asymptotic giant branch (AGB) stars, indicate that the progenitor is a solar-metallicity, 2.25–3.0  $M_{\odot}$  initial-mass star. We derive the best-fit distance of 0.46 kpc by fitting the stellar luminosity (as a function of the distance and effective temperature of the central star) with the adopted post-AGB evolutionary tracks. Our excitation energy diagram analysis indicates high-excitation temperatures in the photodissociation region (PDR) beyond the ionized part of the nebula, suggesting extra heating by shock interactions between the slow AGB wind and the fast PN wind. Through iterative fitting using the Cloudy code with empirically derived constraints, we find the best-fit dusty photoionization model of the object that would inclusively reproduce all of the adopted panchromatic observational data. The estimated total gas mass (0.41  $M_{\odot}$ ) corresponds to the mass ejected during the last AGB thermal pulse event predicted for a 2.5  $M_{\odot}$  initial-mass star. A significant fraction of the total mass (about 70%) is found to exist in the PDR, demonstrating the critical importance of the PDR in PNe that are generally recognized as the hallmark of ionized/H<sup>+</sup> regions.

*Key words:* dust, extinction – ISM: abundances – planetary nebulae: individual (NGC 6781)

## 1. Introduction

The life cycle of matter in the universe is intimately connected with the stellar evolution because stars are the most fundamental building blocks of the universe. Hence, the chemical evolution of galaxies has always been made possible by stellar nucleosynthesis, convection/dredge-up, and, ultimately, stellar mass loss. This stellar mass loss becomes significant when stars evolve into the final stage of stellar evolution, i.e., the asymptotic giant branch (AGB) stage for low-mass stars (1–8  $M_{\odot}$ ) and core-collapsed supernova explosions for high-mass stars (>8  $M_{\odot}$ ).

Either way, the mass-loss process would expel a significant fraction of mass contained in stars as the circumstellar shells, which would eventually become part of the interstellar medium (ISM). Besides gas, molecules and solid-state particles (i.e., dust grains) participate in the stellar mass loss and make up a significant part of the circumstellar shells as the photodissociation region (PDR). These cold components of the mass-loss

ejecta will provide the seed material for the formation of the next generation of stars and planets. Hence, understanding of stellar mass loss is important in characterizing the cosmic mass recycling and chemical evolution in galaxies.

Planetary nebulae (PNe) are low-mass stars that have completed mass loss during the preceding AGB phase and consist of a hot central star ( $\gtrsim 30,000$  K; evolving to become a white dwarf) and an extensive circumstellar shell. While PNe are famous for their spectacular circumstellar structures seen via bright optical emission lines arising from the ionized gas component of the nebula, the ionized part of PNe is surrounded by the neutral gas and dust components (i.e., the PDR). Therefore, being relatively isolated from surrounding objects, PNe provide unique laboratories to further our understanding of the stellar evolution and the chemical evolution of galaxies, from high-temperature fully ionized plasma to low-temperature dusty molecular gas.

So far, more than 2000 PNe in the Milky Way have been identified (Frew 2008; Parker et al. 2016). The evolutionary history of the progenitor (the central star of a PN, CSPN) is imprinted in the circumstellar shells. Radiation from the CSPN permeates into the circumstellar shells, controlling the physical

\* *Herschel* is an ESA Space Observatory with science instruments provided by European-led Principal Investigator consortia and with important participation from NASA.

conditions and local structures (see, e.g., Villaver et al. 2002). Moreover, PNe are in the evolutionary stage in which the circumstellar shells would reach their largest extent before the material at the periphery begins to dissipate into the ISM. Therefore, by investigating spatially extended emission from each of the ionized, atomic, and molecular gas and dust components, one can infer ionic, elemental, and molecular/dust abundances and the mass-loss and evolutionary histories of the CSPN.

Because PNe are  $H^+$  regions, there is a history of observations that has generated a wealth of archival data in the UV and optical. Similarly, the bright ionized gas in PNe is also bright in the radio continuum. With the advent of new technologies, PN observations in the X-ray, near-IR, and mid-IR follow suit. Recently, a window of opportunity in the far-IR was brought forward by a suite of space telescopes, which filled the remaining hole in the spectral coverage. We seized this opportunity and initiated the *Herschel* Planetary Nebula Survey (HerPlaNS; Ueta et al. 2014, HerPlaNS1 hereafter) and its follow-up archival study, HerPlaNS+, using data collected for a hoard of PNe with the *Herschel Space Observatory* (Pilbratt et al. 2010).

In our previous pilot/demonstration study, we focused on the bipolar PN NGC 6781 to empirically characterize its dusty circumstellar nebula based mainly on far-IR data. We confirmed a nearly pole-on barrel structure of the dust shell (of 26–40 K,  $4 \times 10^{-3} M_{\odot}$ ) rich in amorphous carbon via broadband mapping. We also determined the physical stratification of the nebular gas (of  $0.86 M_{\odot}$ ) in terms of the electron density and temperature via spatially resolved far-IR line diagnostics. Moreover, we yielded a gas-to-dust mass ratio map by a direct comparison between the empirically derived dust and gas distributions. These analyses were made with the adopted distance of 0.95 kpc. Assuming that all mass-loss ejecta were detected and that the present-day core mass was  $\sim 0.6 M_{\odot}$ , we concluded that a  $1.5 M_{\odot}$  initial-mass progenitor was about to complete its PN evolution.

In the present study reported here, we continue our investigation of NGC 6781 by adopting as much panchromatic data as possible in addition to our own HerPlaNS far-IR data. This time, our focus is to generate a coherent model of NGC 6781 that would satisfy the adopted panchromatic data as comprehensively as possible. To this end, we first derive the empirical characteristics of the central star and its circumstellar nebula with a greater amount of self-consistently based on the adopted panchromatic data set. Then, we use these empirically derived quantities as more constraining input parameters for a dusty photoionization model consisting of ionized, atomic, and molecular gas plus dust grains to construct one of the most comprehensive models of the object ever produced. In doing so, preference is given to adopting a panchromatic data set rather than exploiting the spatially resolved nature of the data. This is also because, while the existing multiband images of the nebula certainly help us to empirically establish its 3D structures, the amount of imaging data (especially emission-line maps) is still lacking to fit detailed 3D models of internal stratifications in the nebula.

The organization of the rest of the paper is as follows. We summarize the panchromatic observational data of NGC 6781 adopted in the present study (Section 2) and review each of the ionized, atomic, and molecular gas and dust components of the nebula and the central star to derive empirical parameters that

are pertinent to the subsequent dusty photoionization model fitting (Section 3). Then, we present the best-fit dusty photoionization model of NGC 6781 produced with Cloudy (Ferland et al. 2013) while emphasizing improvements made by adopting the panchromatic data comprehensively and self-consistently (Section 4), before describing conclusions drawn from the empirical analyses and modeling (Section 5). This study would demonstrate that the derived best-fit model is robust enough to empirically constrain theoretical stellar evolutionary predictions and that the cold dusty PDR of PNe is at least equally as important as the ionized part when characterizing their progenitor’s evolution and mass-loss histories, especially in the context of the cosmic mass recycling and chemical evolution of galaxies.

## 2. Adopted Panchromatic Data of NGC 6781

### 2.1. Photometry Data

We collect photometry data—10 and 27 data points for the CSPN alone and the nebula plus the CSPN, respectively—from previous observations made with various ground- and space-based telescopes as listed in Table 1 and plotted in Figure 1. We reduce the archived data ourselves to perform photometry measurements unless science grade images are already made available. The diameter of the adopted photometry aperture for the entire nebula (including the CSPN) is indicated in Table 1. For photometry of the CSPN alone, we use a circular aperture of  $0''.4$  (*Hubble Space Telescope* [*HST*]),  $1''.2$  (EFOC2),  $3''.8$  (WFC), and  $2''.2$  (WFCAM) centered at the CSPN. In Appendix A, we outline the method of data reduction and photometry for the *HST*/WFPC2, INT 2.5 m/WFC, ESO NTT 3.6 m/EFOC2, UKIRT 3.8 m/WFCAM, and INT 2.5 m/IPHAS  $H\alpha$  broadband images.

### 2.2. Spectroscopy Data

We collected spectroscopy data from previous optical, mid-IR, and far-IR observations made as summarized in Table 1 and plotted in Figure 1. Detailed accounts of data reduction and spectroscopic measurements are given in Appendix B for each instrument (William Herschel Telescope [WHT]/Intermediate-dispersion Spectrograph and Imaging System [ISIS] in the optical, *Spitzer Space Telescope* [*Spitzer*]/IRS in the mid-IR, and *Herschel*/PACS and SPIRE in the far-IR). Also given in Appendix B is a detailed description as to how the  $H\beta$  flux of the entire nebula is estimated using the IPHAS  $H\alpha$  image. Our choice of the data sets is motivated to ensure that the adopted spectra represent the bulk of the nebula. Figure 2 shows relative slit positions with respect to the entire nebula.

#### 2.2.1. Optical WHT/ISIS Spectrum

The optical WHT/ISIS spectrum is obtained by scanning the nebula along declination during integrations, with the position angle (P.A., defined to be degrees E of N) of the  $79''.6 \times 1''$  slit set at  $90^\circ$ ; the resulting spectrum, therefore, represents an average of the bulk of the central part of the nebula (X.-W. Liu, private communication). Figure 2 shows the central scanned region of  $79''.6 \times 84''$  with a blue box. Flux densities of the WHT/ISIS spectrum are scaled to match the INT/WFC IPHAS  $H\alpha$  band fluxes (see Appendix B.2).

**Table 1**  
The Log of Panchromatic Observations of NGC 6781 Adopted for the Present Study

Photometry Observations						
Obs. Date	Telescope	Instrument	Band	Aperture (Nebula+CSPN)	Program-ID/PI	References
2011 Jul 25	<i>GALEX</i>	<i>GALEX</i>	NUV	180''		
2008 Jul 31	ING/INT 2.5 m	WFC	RGO <i>U</i> , Sloan <i>g</i> and <i>r</i>	320''	I08AN02/P. Groot	
2015 May 12	ESO/NTT 3.6 m	EFOSC2	Bessel <i>B</i> , <i>V</i> , <i>R</i>	200''	60.A-9700(D)/Calibration	
2009 Aug 09	ING/INT 2.5 m	WFC	IPHAS $H\alpha$	320''	C129/J. Casare	
1995 Jul 24	<i>HST</i>	WFPC2/PC	F555W, F814W (CSPN only)		GO6119/H. E. Bond	
2010 Jun 26	UKIRT 3.8 m	WFCAM	<i>J</i> , <i>H</i> , <i>K</i>	180''		
2010 Apr 13	<i>WISE</i>	<i>WISE</i>	3.4, 11.6, 22.1 $\mu\text{m}$	220''–300''		
2004 Apr 20	<i>Spitzer</i>	IRAC	4.5, 5.8, 8.0 $\mu\text{m}$	240''	68/G. Fazio	
1996 Apr 28	<i>ISO</i>	ISOCAM	14.3 $\mu\text{m}$	240''	COX 1/P. Cox	
2011 Oct 17	<i>Herschel</i>	PACS	70, 100, 160 $\mu\text{m}$	240''	OT1-tueta-2/T. Ueta	1
2011 Oct 11	<i>Herschel</i>	SPIRE	250, 350, 500 $\mu\text{m}$	240''	OT1-tueta-2/T. Ueta	1
	Radio telescopes	Various	1.4, 5, 22, 30, 43 GHz			2, 3, 4, 5, 6
Spectroscopy Observations						
Obs. Date	Telescope	Instrument	Wavelength		Program-ID/PI	References
1997 Aug 09	ING/WHT 4.2 m	ISIS	3600–8010 $\text{\AA}$		W-97B-41/X.-W. Liu	7, 8
2005 Oct 19	<i>Spitzer</i>	IRS	5.2–39.9 $\mu\text{m}$		1425/IRS-Calibration	
2011 Oct 14	<i>Herschel</i>	PACS	51–220 $\mu\text{m}$		OT1-tueta-2/T. Ueta	1
2012 Apr 01	<i>Herschel</i>	SPIRE	194–672 $\mu\text{m}$		OT1-tueta-2/T. Ueta	1

**References.** (1) [HerPlaNS1](#); (2) Condon et al. 1998 (376.5  $\pm$  12 mJy at 1.4 GHz); (3) Stanghellini & Haywood 2010 (323 mJy at 5 GHz); (4) Petrov et al. 2007 (190 mJy at 22 GHz); (5) Pazderska et al. 2009 (264.1  $\pm$  7.1 mJy at 30 GHz); (6) Umana et al. 2008 (710 mJy at 43 GHz); (7) Liu et al. 2004a; (8) Liu et al. 2004b.

### 2.2.2. Mid-IR *Spitzer*/IRS Spectra

The archival *Spitzer*/IRS (Houck et al. 2004) spectra are obtained with the SL (5.2–14.5  $\mu\text{m}$ ; a pair of the vertical light-blue  $3''6 \times 57''$  slits at P.A. of  $-10^\circ$  in Figure 2) and LL (13.9–39.9  $\mu\text{m}$ ; the horizontal  $168'' \times 10''5$  slit at P.A. of  $86^\circ$  in Figure 2) modules. Only the SL spectrum was previously presented (Phillips et al. 2011; Mata et al. 2016), whereas we include the LL spectrum in our analysis. While there is only little flux density offset between the SL and LL spectra, we combine the two spectra by scaling the SL spectrum to match the LL spectrum so that the combined mid-IR spectrum would represent the central part of the nebula (Figure 1). Flux densities of the combined mid-IR spectrum are then scaled using the results of mid-IR photometry (see Appendix B.3).

### 2.2.3. Far-IR *Herschel*/PACS and SPIRE Spectra

Far-IR *Herschel* spectra of the nebula for the present study are adopted from those previously presented ([HerPlaNS1](#)). To define a far-IR spectrum representing the bulk of the nebula, we combine spectra from all PACS IFU spaxels ( $5 \times 5$  in the  $50'' \times 50''$  apertures), while a single spectrum from the central bolometer of the SPIRE array is included (of 21'' and 42'' diameter in the short- and long-wavelength band, respectively; at both the “center” and “rim” positions as depicted with white boxes and gray circles, respectively, in Figure 2). The combined far-IR spectra are then scaled using the flux density ratios between far-IR lines and  $H\beta$  for the entire nebula, with the synthesized  $H\beta$  map constructed from the  $H\alpha$  image (see Appendix B.4).

### 2.2.4. Interstellar Reddening Correction and Flux Measurements

Once we reconstruct spectra in the optical, mid-IR, and far-IR to represent the bulk of the nebula, we measure line fluxes

by Gaussian fitting. For the ISIS spectrum, the line fluxes are corrected for the interstellar extinction with the following formula:

$$I(\lambda) = F(\lambda) \cdot 10^{c(H\beta)(1+f(\lambda))}, \quad (1)$$

where  $I(\lambda)$  is the dereddened line flux,  $F(\lambda)$  is the observed line flux,  $c(H\beta)$  is the reddening coefficient at  $H\beta$ , and  $f(\lambda)$  is the interstellar extinction function at  $\lambda$  computed by the reddening law of Cardelli et al. (1989) with  $R_V = 3.1$ .

We measure the reddening correction factor  $c(H\beta)$  by comparing the observed Balmer line ratios of  $H\gamma$  and  $H\alpha$  to  $H\beta$  with the theoretical ratios given by Storey & Hummer (1995) for an electron temperature  $T_e = 10,000$  K and an electron density  $n_e = 200 \text{ cm}^{-3}$  under the assumption that the nebula is optically thick to  $\text{Ly}\alpha$  (so-called “Case B”; e.g., see Baker & Menzel 1938; also see Section 3.1.1 for the bases of these  $n_e$  and  $T_e$  values). The measured  $c(H\beta)$  turns out to be  $0.951 \pm 0.091$  from the  $F(H\gamma)/F(H\beta)$  ratio and  $1.014 \pm 0.033$  from the  $F(H\alpha)/F(H\beta)$  ratio. Thus, we adopt  $c(H\beta)$  of  $1.007 \pm 0.031$ , which is a weighted mean of the above values. We do not correct for the interstellar extinction at longer wavelengths than  $K$  band because extinction would be negligible at those wavelengths. The final dereddening line fluxes measured in the adopted spectra are listed in Table 12. The quoted fluxes are normalized with respect to  $I(H\beta) = 100$ .

While we adopt these reprocessed 1D panchromatic spectra and duly measured dereddened line fluxes as representative of the bulk of the nebula, a word of caution appears appropriate at this point. As Figure 2 shows, the spatial coverage of the nebula by various spectroscopic apertures is not complete and uniform. As would become apparent later from the model fitting (Section 4), there would be some inconsistencies in line emission strengths, especially in neutral and low-excitation lines such as [N I], [O I], and [S II] (see Section 3.1.2). This is primarily because the highest surface brightness regions (the E



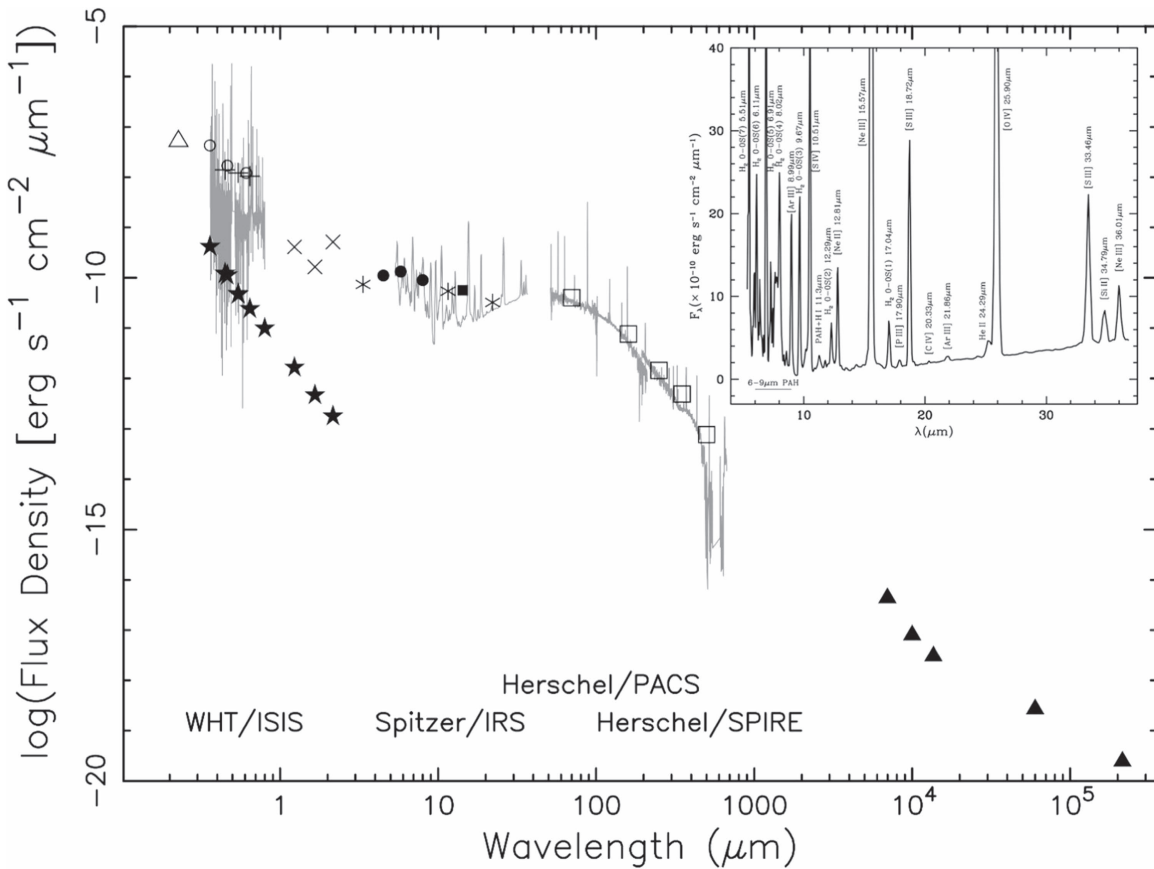


**Figure 1.** Panchromatic photometric and spectroscopic data of NGC 6781 adopted in the present study. Broadband photometry was done over the entire extent of the nebula from the following sources: *GALEX* (open triangle), *ING/INT* (open circles), *ESO/NTT* (plus signs), *UKIRT* (crosses), *WISE* (asterisks), *Spitzer* (filled circles), *ISO* (filled square), *Herschel* (open squares), and radio (filled triangles), while photometry of the CSPN (filled stars) was also done using *HST/WFPC2* images in addition to the above optical and near-infrared *JHK* sources. Spectra (gray lines) were sourced from *WHT/ISIS*, *Spitzer/IRS*, and *Herschel/PACS* and *SPIRE*. The adopted spectra from four instruments are shown in gray lines, with their respective spectral ranges indicated at the bottom. The inset displays the *Spitzer/IRS* spectra in the mid-IR full of H<sub>2</sub>, polycyclic aromatic hydrocarbons (PAHs), and ionized gas emission features/lines, with the dust continuum steadily rising toward longer wavelengths from around 10 μm. See text for how the data were scaled with respect to each other. See also Tables 11 and 12.

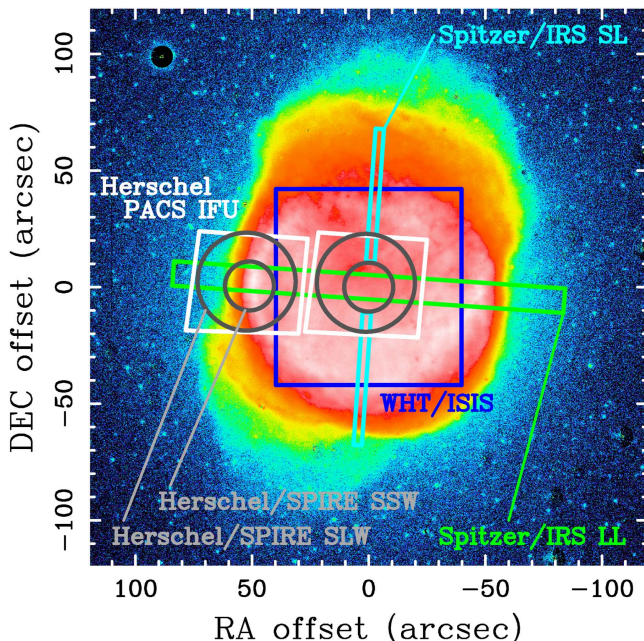


**Figure 2.** Relative slit positions of previous spectroscopic observations with respect to the NGC 6781 nebula shown on the NOT/H $\alpha$  image (previously presented by Phillips et al. 2011), in which field stars are subtracted by PSF fitting. N is up and E is to the left.

and W end of the central ring structure; Figure 2) are missed in the optical data and may be less strongly weighted than they should be in the far-IR data. We will return to these issues when we discuss model fitting in Section 4.

### 3. Anatomy of NGC 6781

#### 3.1. The Ionized/Neutral Gas Component

##### 3.1.1. Plasma Diagnostics

We determine the  $n_e$  and  $T_e$  pairs for the ionized/neutral gas component<sup>13</sup> of NGC 6781 for a few temperature/ionization regions based on various collisionally excited lines (CELs) and recombination lines (RLs) detected in the adopted panchromatic spectra. In the present plasma diagnostics and the subsequent ionic abundance derivations, we adopt the effective recombination coefficients, transition probabilities, and effective collisional strengths listed in Tables 7 and 11 of Otsuka et al. (2010), in which all the original references to all the atomic data are found. The diagnostic line ratios used in the

<sup>13</sup> Strictly speaking, we expect two kinds of ionized (ionized atomic and ionized molecular) gas and two kinds of neutral (atomic and molecular) gas. In the present study, however, we almost exclusively mean ionized atomic gas when we refer to ionized gas and neutral atomic gas when we refer to atomic gas.

**Table 2**  
Summary of Plasma Diagnostics Using Nebular Lines

ID	Ion	$n_e$ -diagnostics	Ratio	Result ( $\text{cm}^{-3}$ )
1	[O I]	$I(63 \mu\text{m})/I(146 \mu\text{m})$	$11.423 \pm 2.039$	$590^{+1190}$
2	[S II]	$I(6716 \text{ \AA})/I(6731 \text{ \AA})$	$1.201 \pm 0.048$	$230 \pm 60$
3	[O II]	$I(3726 \text{ \AA})/I(3729 \text{ \AA})$	$0.848 \pm 0.035$	$270 \pm 50$
4	[N II]	$I(122 \mu\text{m})/I(205 \mu\text{m})$	$4.902 \pm 0.991$	$280 \pm 120$
5	[S III]	$I(18.7 \mu\text{m})/I(33.5 \mu\text{m})$	$0.939 \pm 0.092$	$1020 \pm 300$
6	[Ne III]	$I(15.6 \mu\text{m})/I(36.0 \mu\text{m})$	$13.789 \pm 1.471$	$12\,600 \pm 7590$
7	[O III]	$I(4959 \text{ \AA})/I(88.3 \mu\text{m})$	$1.438 \pm 0.178$	$220 \pm 50$
ID	Ion	$T_e$ -diagnostics	Ratio	Result (K)
8	[S II]	$I(6716/31 \text{ \AA})/I(4069 \text{ \AA})$	$14.891 \pm 3.270$	$10\,520 \pm 1820$
9	[N II]	$I(6548/83 \text{ \AA})/I(5755 \text{ \AA})$	$81.931 \pm 2.956$	$10\,800 \pm 170$
10	[N II]	$I(6548/83 \text{ \AA})/$ $I(122 \mu\text{m}+205 \mu\text{m})$	$57.325 \pm 6.201$	$12\,360 \pm 980$
11	[O II]	$I(3726/29 \text{ \AA})/I(7320/30 \text{ \AA})$	$50.262 \pm 1.949$	$9650 \pm 200$
12	[Ar III]	$I(7135 \text{ \AA}+7751 \text{ \AA})/I(9.0 \mu\text{m})$	$1.211 \pm 0.098$	$9350 \pm 400$
13	[O III]	$I(4959 \text{ \AA})/I(4363 \text{ \AA})$	$52.943 \pm 3.584$	$10\,050 \pm 210$
14	[Ne III]	$I(3868 \text{ \AA}+3967 \text{ \AA})/I(36.0 \mu\text{m})$	$9.578 \pm 0.806$	$10\,340 \pm 250$
	He I	$I(7281 \text{ \AA})/I(6678 \text{ \AA})$	$0.156 \pm 0.021$	$7070 \pm 1880$

present analysis and the resultant  $n_e$  and  $T_e$  values are summarized in Table 2.

The  $n_e$ - $T_e$  plot shown in Figure 3 summarizes how  $n_e$  and  $T_e$  relate to each other in the regions of the nebula, from which the particular CELs involved in the diagnostic line ratios would arise: the solid lines are the  $n_e$ - $T_e$  curves derived from the  $T_e$ -sensitive ratios, while the dashed lines are those from the  $n_e$ -sensitive line ratios. Strictly speaking, the diagnostic lines labeled as (1), (7), (8), (10), and (11) in Figure 3 are sensitive to both  $n_e$  and  $T_e$ . In the present work, however, we used the lines (1) and (7) as  $n_e$  indicators and (8), (10),<sup>14</sup> and (11) as  $T_e$  indicators, respectively. By doing so, we estimated  $T_e$ ([O III]),  $T_e$ ([O II]),  $T_e$ ([N II]), and  $T_e$ ([S II]) by adopting  $n_e$ ([O III]),  $n_e$ ([O II]), Ne([N II]), and  $n_e$ ([S II]). Since we could not deblend [N I]  $\lambda$ 5198/ $\lambda$ 5200 (its ratio is a density indicator for the neutral region), we used the far-IR [O I] ratio.

Liu et al. (2004b) reported five  $n_e$  and four  $T_e$  values based on the CELs seen in the ISIS spectra augmented by lines detected in the ISO spectra (see their Table 7). Taking advantage of the fine-structure lines detected at higher sensitivity and better spatial resolution in the *Spitzer* and *Herschel* spectra, we calculate seven  $n_e$  and eight  $T_e$  values. Our values of the CEL  $n_e$  and  $T_e$  are generally consistent with those determined by Liu et al. (2004b).

The  $n_e$ - $T_e$  diagnostic diagram (Figure 3) suggests that the bulk of the ionized gas appears to have  $T_e$  between  $\sim$ 6000 and  $\sim$ 12,000 K. Thus, we adopt a constant  $T_e = 10,000$  K to derive  $n_e$  values. The derived  $n_e$ ([Ne III]) value is more than one order of magnitude larger than the other  $n_e$  values. To double-check the above, we analyze the *Spitzer*/IRS spectra of the nebula nearby the central star obtained with the higher-dispersion SH and LH modules (of the  $4''.7 \times 11''.3$  and  $11''.1 \times 22''.3$  slit dimensions, respectively; not shown in Figure 2). From the SH and LH spectra alone, we derive  $n_e$ ([Ne III]) =  $4930 \pm 2780 \text{ cm}^{-3}$  and  $n_e$ ([S III]) =  $1240 \pm 60 \text{ cm}^{-3}$ . Because the spatial coverage of the

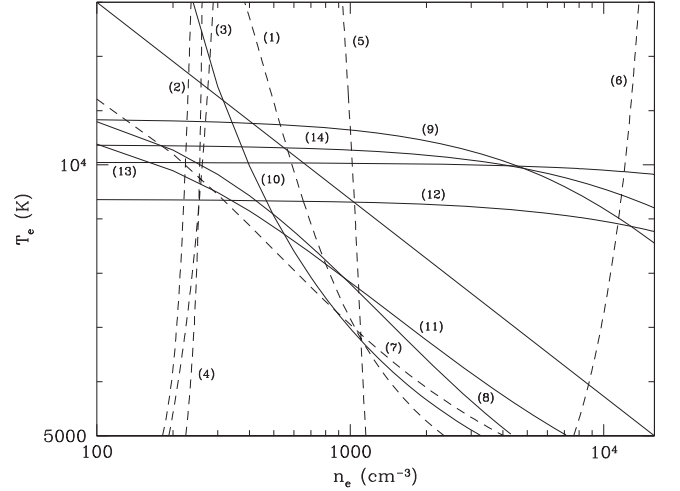


**Figure 3.** The  $n_e$ - $T_e$  diagram based on CEL diagnostic lines. The dashed and solid lines are the  $n_e$  and  $T_e$  indicators, respectively. The ID numbers indicate the corresponding line ratios listed in Table 2.

SH and LH modules is very restrictive around the central star, the higher  $n_e$  and  $T_e$  values may be influenced heavily by the conditions in the vicinity of the central star. Previously, the [O III]  $52/88 \mu\text{m}$  ratio in the central part of the cavity yielded  $350 \text{ cm}^{-3}$ .

Next, we calculate  $T_e$  based on the derived  $n_e$  values. The average of  $n_e = 260 \text{ cm}^{-3}$  among  $n_e$ ([S II], [O II], [N II]) is adopted to calculate  $T_e$ ([S II]) and  $T_e$ ([N II]) (ID: 10). To compute  $T_e$ ([Ar III] and [Ne III]),  $n_e$ ([O III]) of  $220 \text{ cm}^{-3}$  is adopted. To calculate  $T_e$ ([O III]),  $T_e$ ([O II]), and  $T_e$ ([N II]) (ID: 9) accurately, we subtract contributions from  $\text{O}^{3+}$ ,  $\text{O}^{2+}$ , and  $\text{N}^{2+}$  RLs to the [O III]  $\lambda$ 4363, [O II]  $\lambda$ 7320/30, and [N II]  $\lambda$ 5755 lines, respectively, i.e.,  $I_R$ ([O III]  $\lambda$ 4363),  $I_R$ ([O II]  $\lambda$ 7320/30), and  $I_R$ ([N II]  $\lambda$ 5755).

We calculate  $I_R$ ([O III]  $\lambda$ 4363) with

$$\frac{I_R([\text{O III}] \lambda 4363 \text{ \AA})}{I(\text{H}\beta)} = 12.4 \left( \frac{T_e}{10^4} \right)^{0.59} \frac{\text{O}^{3+}}{\text{H}^+} \quad (2)$$

<sup>14</sup> One might think that the [N II]  $I(6548/83 \text{ \AA})/I(122 \mu\text{m} + 205 \mu\text{m})$  ratio is sensitive to  $n_e$ , compared with the diagnostic labeled with IDs (8) and (11). For that case, we calculate  $n_e = 400 \pm 50 \text{ cm}^{-3}$  at  $T_e = 10^4$  K using this [N II] diagnostic ratio. Adopting this  $n_e$  for the following analyses does not change our conclusions.

(Equation (3) in Liu et al. 2000), for which the  $O^{3+}/H^+$  ratio (3.02(−5); see Section 3.1.2) is computed using the  $I([O\text{ IV}] 25.9\ \mu\text{m})/I(H\beta)$  ratio assuming  $T_e([Ne\text{ III}])$  and  $n_e([O\text{ III}])$ . In the end,  $I_R([O\text{ III}] \lambda 4363)$  turns out to be 0.73% of the observed  $I([O\text{ III}] \lambda 4363)$ . After we subtract  $I_R([O\text{ III}] \lambda 4363)$  from the observed  $I([O\text{ III}] \lambda 4363)$ , we obtain  $T_e([O\text{ III}])$  by adopting  $n_e([O\text{ III}])$ .

$I_R([O\text{ II}] \lambda 7320/30)$  is calculated with

$$\frac{I_R([O\text{ II}] 7320/30\ \text{\AA})}{I(H\beta)} = 9.36 \left( \frac{T_e}{10^4} \right)^{0.44} \frac{O^{2+}}{H^+} \quad (3)$$

(Equation (2) in Liu et al. 2000), where we adopt the  $O^{2+}/H^+$  ratio (2.78(−4); see Section 3.1.2) derived from the  $I([O\text{ III}] 88.3\ \mu\text{m})/I(H\beta)$  ratio assuming  $T_e([O\text{ III}])$  and  $n_e([O\text{ III}])$ .  $I_R([O\text{ II}] \lambda 7320/30)$  turns out to be 2.19% of the observed  $I([O\text{ II}] \lambda 7320/30)$ . After we subtract the recombination contribution from the observed  $I([O\text{ II}] \lambda 7320/30)$ , we obtain  $T_e([O\text{ II}])$  by adopting  $n_e = 260\ \text{cm}^{-3}$ .

Finally, we estimate  $I_R([N\text{ II}] \lambda 5755)$  using

$$\frac{I_R([N\text{ II}] 5755\ \text{\AA})}{I(H\beta)} = 3.19 \left( \frac{T_e}{10^4} \right)^{0.33} \frac{N^{2+}}{H^+} \quad (4)$$

(Equation (1) in Liu et al. 2000), where the  $N^{2+}/H^+$  ratio (7.01(−5); see Section 3.1.2) was calculated using the  $I([N\text{ III}] 57\ \mu\text{m})/I(H\beta)$  ratio assuming  $T_e([O\text{ III}])$  and  $n_e([O\text{ III}])$ .  $I_R([N\text{ II}] \lambda 5755)$  is 0.54% of the observed  $I([N\text{ II}] \lambda 5755)$ . After we subtract  $I_R([N\text{ II}] \lambda 5755)$ , we obtain  $T_e([N\text{ II}])$  (ID: 9) by adopting  $n_e = 260\ \text{cm}^{-3}$ . In Section 4 below, we verify the above estimates of the RL contributions based on the best-fit modeling results.

We also determine  $T_e(\text{He I})$ , which is necessary to estimate  $\text{He}^+$  and  $\text{He}^{2+}$  abundances, using the  $\text{He I } I(7281\ \text{\AA})/I(6678\ \text{\AA})$  ratio with the He I recombination coefficients in the case of  $n_e = 100\ \text{cm}^{-3}$  given by Benjamin et al. (1999). The  $n_e$  and  $T_e$  pairs derived and adopted from the present plasma diagnostics are summarized in Table 13.

### 3.1.2. Ionic Abundance Derivations

We calculate CEL ionic abundances by solving the equation of population at multiple energy levels with the adopted  $n_e$  and  $T_e$  (Table 13, which also lists the adopted  $n_e$  and  $T_e$  to calculate RL  $\text{He}^{+2+}$  and  $\text{C}^{2+}$  abundances); the resulting ionic abundances are listed in Table 14. We give the  $1\sigma$  uncertainty for each ionic abundance estimate, which is propagated from  $1\sigma$  uncertainties of line fluxes,  $c(H\beta)$ ,  $n_e$ , and  $T_e$ . Ionic abundances are derived for each of the detected line intensities when more than one line for a particular target ion is detected. In such cases, we adopt the weighted average of all of the derived abundances listed at the last line for that particular ion in italics.

The resulting ionic abundances based on different lines in the optical nebular, auroral, and trans-auroral transitions to IR fine-structure lines turn out to be generally consistent with each other within the associated uncertainties for most of the cases. This indicates that our choice of the  $n_e$ – $T_e$  pair for each ionic species is robust and that the adopted scaling of the mid- and far-IR line fluxes to the optical  $H\beta$  line flux via the adopted photometry data is reasonable. However, there are a few exceptions, which we briefly discuss below.

As pointed out above, the spatial coverage of the nebula in spectroscopic observations is not complete and uniform: especially, the ISIS spatial coverage in the optical missed the brightest E and W “rim” regions, in which low-excitation and neutral lines are particularly strong (Figure 2). This explains why the  $O^0$  abundances derived from optical lines are much smaller than the abundance based on the  $[O\text{ I}] 145\ \mu\text{m}$  line (by a factor of  $7.5 \pm 4.8$ ). Hence, if we were to assume  $O^0/H^+ = (5.38 \pm 1.05)(-4)$  based solely on the  $[O\text{ I}] 145\ \mu\text{m}$  line, we would have  $N^0/H^+ = (3.69 \pm 2.34)(-4)$  and  $S^+/H^+ = (8.97 \pm 6.09)(-6)$  by adopting a factor of  $7.5 \pm 4.8$ . Nevertheless, for the  $O^0/H^+$  abundance we adopt the average of the observed two optical (6300 and 6364  $\text{\AA}$ ) and single far-IR (145  $\mu\text{m}$ ) lines, because there is no way to ascertain how much line flux is missed by incomplete spatial coverage of the nebula.

To determine the  $\text{He}^+$  abundance, we do not include the He I  $\lambda 4712$  line because the blue wing of this line seems to be contaminated by the  $[\text{Ar IV}] \lambda 4711$  line. Assuming that  $\text{He}^+$  is indeed 1.08(−1),  $I(\text{He I } \lambda 4712)$  and  $I([\text{Ar IV}] \lambda 4711)$  have to be  $0.47 \pm 0.18$  and  $0.87 \pm 0.27$ , respectively.<sup>15</sup> The  $\text{Ar}^{3+}$  abundance derived from this expected  $I([\text{Ar IV}] \lambda 4711)$  is  $1.99(-7) \pm 6.41(-8)$ , which is consistent with the  $\text{Ar}^{3+}$  abundance derived from  $I([\text{Ar IV}] \lambda 4740)$ .

To derive the RL  $\text{C}^{2+}$  abundance, we use the C II  $\lambda 4267$  line with its effective recombination coefficient in Case B for  $n_e = 10^4\ \text{cm}^{-3}$  defined as a polynomial function of  $T_e$  by Davey et al. (2000). This is justified because while the effective recombination coefficient is not available for the case of  $n_e = 100\ \text{cm}^{-2}$  that is more appropriate here, the RL abundances are in general insensitive to  $n_e$  for  $\lesssim 10^8\ \text{cm}^{-3}$ . As for  $T_e$ , we adopt  $T_e([\text{Ar III}])$  because the ionization potential (I.P.) of  $\text{C}^{2+}$  is similar to that of  $\text{Ar}^{2+}$ .

Overall, we conclude that our derived ionic abundances are improved with new CEL detections in the mid- and far-IR (such as  $\text{Ne}^{+2+}$ ,  $\text{S}^{2+}$ ,  $\text{Si}^+$ ,  $\text{Cl}^{3+}$ , and  $\text{Ar}^{2+}$ ) made with *Spitzer* and *Herschel* observations, more robust adaptation of  $n_e$  and  $T_e$  for targeting ions, and the use of a larger number of lines in various ionization stages, compared with those calculated previously by Liu et al. (2004a).

### 3.1.3. Elemental Abundance

By introducing the ionization correction factor (ICF; see, e.g., Delgado-Inglada et al. 2014, for more detail), we infer the nebular abundances of the observed nine elements in the ionized part of the nebula based on their observed ionic abundances. In Table 14, the ICF(X) value of the element “X” and the resulting elemental abundance,  $X/H = \text{ICF}(X) \times (\sum_{m=1} X^{m+}/H^+)$ , are listed in bold at the last line for each element. Here, we exclude  $\text{C}^+$ ,  $\text{N}^0$ , and  $\text{O}^0$  from abundance calculations for the respective elements, as these ions are considered to be present mostly in the PDR surrounding the ionized part of the nebula. In Table 3, we compare the derived elemental abundances  $\epsilon(X)$  corresponding to  $\log_{10}(X/H) + 12$ , where  $\log_{10}(H) = 12$  (in column (2)), and the relative solar abundances ( $X/H$ ; in column (3)).

We perform an ionization correction using the ICF based on the I.P. of the element in question, except for He, O, Ne, and S (i.e., ICF for these four elements is taken to be unity because

<sup>15</sup> Our best-fit model using Cloudy predicts  $I(\text{He I } \lambda 4712) = 0.600$  and  $I([\text{Ar IV}] \lambda 4711) = 0.982$ . See Section 4.



**Table 3**

Elemental Abundances  $\epsilon(X)$  of NGC 6781 Derived in the Present Analysis, Compared with the Solar Abundances (Column (3));  $[X/H] = \epsilon(X) - \epsilon_{\odot}(X)$ , Where  $\epsilon_{\odot}(X)$  Is Taken from Lodders (2010), Previous Empirical Analysis (Column (4); by Liu et al. 2004a), and Model Predictions (Columns (5) and (6); by Karakas 2010; see Section 3.1.5)

X	$\epsilon(X)$	$[X/H]$	$\epsilon(X)$	$\epsilon(X)$	$\epsilon(X)$
(1)	(2)	(3)	(4)	(5)	(6)
He	$11.06 \pm 0.17$	$+0.13 \pm 0.17$	11.08	11.05	11.06
C(RL)	$9.61 \pm 0.29$	$+1.22 \pm 0.30$	9.17	8.52	9.06
C(CEL)	8.56–9.00	+0.17–0.61	...	...	...
N	$8.15 \pm 0.09$	$+0.29 \pm 0.15$	8.38	8.39	8.42
O	$8.76 \pm 0.04$	$+0.03 \pm 0.08$	8.65	8.94	8.94
Ne	$8.15 \pm 0.05$	$+0.10 \pm 0.11$	8.22	8.12	8.27
Si	$7.03 \pm 0.27$	$-0.50 \pm 0.28$	...	7.57	7.59
S	$6.91 \pm 0.06$	$-0.25 \pm 0.06$	6.97	7.42	7.44
Cl	$5.16 \pm 0.42$	$-0.09 \pm 0.42$	5.43	...	...
Ar	$6.49 \pm 0.10$	$-0.01 \pm 0.14$	6.35	...	...

**Note.** The number density ratio relative to hydrogen is  $\epsilon(X) = \log_{10}(X/H) + 12$ , where  $\log_{10}(H) = 12$ . The CEL C abundance, C(CEL), is an *expected* value.

unobserved high-excitation lines are considered negligible). We will compare these ICFs based on the I.P. and the predicted ICFs by the best-fit modeling in Section 4.

In performing ionization correction, the ICF for N, Si, Cl, and Ar is set as follows. We assume that the N abundance is the sum of  $N^{+,2+,3+}$  and adopt  $ICF(N) \approx ICF(O)$ , which is equal to the  $O/(O^+ + O^{2+})$  ratio. Similarly, we assume that the Si abundance is the sum of  $Si^{+,2+,3+}$  and adopt  $ICF(Si) \approx ICF(S)$ , which corresponds to the  $S/S^+$  ratio. For Cl and Ar, we assume that the Cl and Ar abundances are the sum of  $Cl^{+,2+,3+}$  and  $Ar^{+,2+,3+}$ , respectively. Then, we adopt  $ICF(Cl) \approx ICF(Ar) \approx ICF(S)$ , which corresponds to the  $S/(S^{2+} + S^{3+})$  ratio.

As for the ICF(C), we originally adopt  $ICF(C) \approx ICF(N)$  corresponding to the  $N/N^{2+}$  ratio. With this ICF(C), the derived RL C abundance using the RL C II  $\lambda 4267$  line would come out to be  $4.06(-3) \pm 1.19(-3)$ . Note that we do not include the CEL C<sup>+</sup> abundance for the elemental C abundance because (1) the [C II] 157  $\mu\text{m}$  line arises mostly from the PDR as stated above and (2) the nature of these lines is different (C<sup>2+</sup> is of RL while C<sup>+</sup> is of CEL).

However, this RL C abundance would be extremely unlikely for NGC 6781. The average abundance between  $[Cl/H]$  and  $[Ar/H]$  derived for NGC 6781 suggests that the metallicity ( $Z$ ) of the object is close to the solar metallicity (see also Section 3.1.5). Then, such a high RL C abundance is very difficult to explain by current AGB nucleosynthesis models (e.g., Karakas 2010) for stars with solar metallicity ( $Z \sim 0.02 Z_{\odot}$ ). Hence, the derived RL C abundance of  $4.06(-3) \pm 1.19(-3)$  appears to be overestimated.

It is known that C, N, O, and Ne ionic abundances derived from RLs are sometimes found to be larger than the corresponding abundances obtained from CELs in PNe and H II regions. This issue is known as the abundance discrepancy problem (see, e.g., Liu 2006, for more detail). In spite of a number of attempts to explain such ionic/elemental abundance discrepancies, no consensus has been reached yet. Thus, we need other options to estimate the C abundance in light of the abundance discrepancy problem. One option is to compute the *expected* CEL C abundance by scaling the *measured* RL C

abundance with the average  $C^{2+}(\text{RL})/C^{2+}(\text{CEL})$  ratio because no UV spectrum is available for NGC 6781.

Previously, Delgado-Inglada & Rodríguez (2014) showed general agreement between *measured* and *scaled* CEL abundances, the latter of which was scaled from *measured* RL abundances with the average  $C^{2+}(\text{RL})/C^{2+}(\text{CEL})$  ratio of  $4.41 \pm 0.81$  among 37 Galactic PNe (their Table 5). While it is yet unknown whether there is a correlation between the RL and CEL C abundances, the relatively small standard deviation of the measured ratios would indicate that this option has some merit. Because there are no other alternatives, we adopt this option for the present study and use the average  $C^{2+}(\text{RL})/C^{2+}(\text{CEL})$  ratio of  $4.10 \pm 0.49$  found among 58 PNe in the Milky Way and Magellanic Clouds (Otsuka et al. 2011) to obtain the scaled *expected* CEL C of  $9.89(-4) \pm 3.14(-4)$ .

This *expected* CEL C of  $9.89(-4) \pm 3.14(-4)$  ( $\epsilon(C) = 9.00$ ) would be more reasonable than the measured RL C abundance of  $4.06(-3) \pm 1.19(-3)$  with respect to current AGB nucleosynthesis models for the solar abundance stars (e.g., Karakas 2010). In addition, Delgado-Inglada & Rodríguez (2014) reported a  $C^{2+}(\text{RL})/C^{2+}(\text{CEL})$  ratio of 3.63 for NGC 6720, which possesses central star and nebula properties very similar to those of NGC 6781 (see Section 3.4.1).

#### 3.1.4. Further on the C and Cl Abundances

Because our present analysis and the previous analysis done by Liu et al. (2004a; listed in Table 3, column (4)) are based on the same ISIS optical spectrum, both results should be consistent with each other. However, this is not the case for C and Cl.

The discrepancy in  $\epsilon(\text{Cl})$  arises because we adopt the  $Cl^{2+,3+}$  abundances of 1.07(-7) and 1.57(-8) and the corresponding ICF(Cl) value of 1.17, while Liu et al. (2004a) used the  $Cl^{2+}$  abundance of 7.92(-8) only with the corresponding ICF(Cl) of 3.394. In addition, the adopted  $T_e$  could contribute to the discrepancy because the Cl ionic abundances are determined using their CEL lines, whose emissivities are sensitive to  $T_e$ . Overall, we would argue again that our  $\epsilon(\text{Cl})$  value is more improved than the previous estimate because we have more robust  $T_e$  for the ionic Cl abundances and we derive a  $Cl^{3+}$  abundance that would reduce uncertainties in ICF(Cl).

The discrepancy in RL  $\epsilon(C)$  is due to different values of I (C II  $\lambda 4267$ ) (which might be caused by different adopted  $c(H\beta)$  and adopted ICF(C): our  $\epsilon(C)$  and ICF(C) values are 2.0(-3) and 2.03, whereas theirs are 9.05(-4) and 1.624, respectively). In general, C is a very important element as a coolant of the ionized gas component and also a source of C-based molecules in PNe. Thus, we would discuss the C abundance further in this section.

Our *expected* C(CEL) of  $9.89(-4) \pm 3.14(-4)$  ( $\epsilon(C) = 9.00$ ) adopted in the previous section, in comparison with the observed O(CEL) of  $5.81(-4) \pm 2.19(-5)$  ( $\epsilon(O) = 8.76$ ), would suggest a slightly C-rich nature for NGC 6781 (C/O number density ratio of  $1.70 \pm 0.54$ ). Indeed, the *Spitzer*/IRS mid-IR spectrum (Figure 1, inset) shows polycyclic aromatic hydrocarbon (PAH) emission at 6–9  $\mu\text{m}$  (mostly from ionized PAH) and at 11.3  $\mu\text{m}$  (from neutral PAH) and dust continuum due to amorphous carbon, while the spectrum does not clearly show any O-rich dust features such as amorphous silicates at  $\sim 9$  and  $\sim 18$   $\mu\text{m}$  and crystalline silicates around 30  $\mu\text{m}$ .

Guzman-Ramirez et al. (2014) reported detection of PAH emission in O-rich PNe in the Galactic bulge and suggested



that PAHs could be formed in the compact/dense torus (i.e., the “waist” region of bipolar PNe) using C atoms liberated from CO molecules by photodissociation. At this point, there is no clear evidence to suggest this possibility for NGC 6781 based on the spatially resolved spectroscopic data.

If we adopt RL  $C^{2+}$  of 9.05(−4) and ICF(C) of 1.634 as previously used by Liu et al. (2004a) and convert the RL C abundance to the CEL C abundance by the average  $C^{2+}$ (RL)/ $C^{2+}$ (CEL) ratio of 4.10 (Otsuka et al. 2011), we would obtain the expected CEL C abundance of 3.61(−4), which would correspond to  $\epsilon$ (C) of 8.56. This would result in a C/O ratio of  $\sim 0.76$ , indicating that NGC 6781 is slightly O-rich. Hence, the possibility of NGC 6781 being O-rich is not completely ruled out.

As seen above, the C abundance depends on many factors, from the  $I(\text{C II } \lambda 4267)$  measurements to the ICF(C) and  $C^{2+}$ (RL)/ $C^{2+}$ (CEL) values adopted. Therefore, in the present work, we opt to allow a range of the expected CEL abundance for NGC 6781 as  $\epsilon$ (C) = 8.56–9.00 (correspondingly,  $[C/H] = 0.17\text{--}0.61$ ) based on the arguments presented above.

### 3.1.5. Comparison with the Previous Model Predictions

We compare the derived  $\epsilon$ (X) with the values predicted by AGB nucleosynthesis models. As for the metallicity  $Z$  of the progenitor of NGC 6781, it is best to reference elements that can never be synthesized within AGB stars. Thus, we adopt Cl and Ar as good  $Z$  indicators. The average between the observed  $[Cl/H]$  and  $[Ar/H]$  values of  $-0.05$  corresponds to  $Z \sim 0.018$ .

However, the S abundance ( $[S/H] = -0.25$ ) suggests a much lower  $Z$ . So far, this S abundance anomaly has been found in many Milky Way and M31 PNe (Henry et al. 2012; see their Figure 1). Henry et al. (2012) concluded that the sulfur deficit in PNe is generally reduced by increasing the  $S^{3+}$  abundance and selecting a proper ICF(S). Such an S depletion may indicate that a significant part of the atomic S mass is locked up as sulfide grains in the nebula (e.g., MgS and FeS in C- and O-rich environments, respectively). However, the *Spitzer*/IRS spectrum displays neither the broad  $30\ \mu\text{m}$  feature often attributed to MgS nor narrower emission features around  $30\ \mu\text{m}$  attributed to FeS. The discrepancy between the observed and the AGB model S abundances may thus be related to the adopted reaction rates; Shingles & Karakas (2013) demonstrated a possibility that the S depletion could be explained by introducing a large  $^{22}\text{Ne}(\alpha, n)^{25}\text{Mg}$  reaction rate. Here, we propose that the apparently low  $[S/H]$  abundance is attributed to missing fluxes of low-excitation  $[S\ \text{II}]$  lines as discussed above (by adopting the revised  $S^+/H^+ = 8.97(-6)$  in Section 3.1.2, we would obtain  $\epsilon$ (S) = 7.20, which is consistent with  $\epsilon$ (S) $_{\odot}$ ).

Now, we compare our empirically derived elemental abundances with those predicted with AGB nucleosynthesis models of  $Z = 0.02$  stars (Karakas 2010) in Table 3: the values in columns (5) and (6) are the predicted values for initially  $2.25$  and  $3.0\ M_{\odot}$  stars, respectively. To assess the goodness of fit of the model prediction, we evaluate chi-square values ( $\chi^2$ ) between our derived abundances and the model-predicted abundances for stars in the initial mass range from  $1.5$  to  $4.0\ M_{\odot}$ . Adopting the lower CEL abundance limit of  $\epsilon$ (C) = 8.56, a good fit to the observed  $\epsilon$ (X) is achieved with the  $2.25\ M_{\odot}$  model (reduced  $\chi^2 = 15.5$ ).

Meanwhile, adopting the upper CEL abundance limit of  $\epsilon$ (C) = 9.00, the  $\chi^2$  values suggest that the observed  $\epsilon$ (X) is

most consistent with the  $2.5\ M_{\odot}$  model (reduced  $\chi^2 = 16.15$ ). The reduced  $\chi^2$  value = 17.5 of the  $3.0\ M_{\odot}$  model is equally good. Therefore, based on these results, we conclude that the initial mass of the CSPN is between  $2.25$  and  $3.0\ M_{\odot}$ .

## 3.2. The Molecular Gas Component

Given the number of molecular lines seen in the spectra, especially with the rare  $\text{OH}^+$  detection (Aleman et al. 2014), NGC 6781 has to be treated as a PN rich in neutral gas. Then, it is critical to include the PDR of the nebula for a complete understanding of all of its components (ions, atoms, molecules, and dust). In this section, therefore, we investigate the physical conditions of the most abundant species in the PDR,  $\text{H}_2$ , to articulate our understanding of the PDR in NGC 6781.

### 3.2.1. Physical Conditions: Spatial Distribution

We obtain the  $\text{H}_2$  image taken with the Wide-field Infrared Camera (WIRCAM; Puget et al. 2004) on the  $3.6\ \text{m}$  Canada–France–Hawaii Telescope (CFHT) from the Canadian Astronomy Data Centre (CADC). The observations were done on 2006 April 14 (PI: S. Kwok, Prop. ID: 06AT03) through Taiwan CFHT time. The basic calibrated data set retrieved from the CADC archive is reduced into a single image after bad-pixel masking and geometric distortion correction using IRAF. Figure 4 shows the  $\text{H}_2\ v = 1 - 0\ \text{S}(1)$  image at  $2.122\ \mu\text{m}$  overlaid with contours of  $[\text{N II}]\ \lambda 6583$  emission and the close-up of the central region from which emission of the spectra adopted in the present study arose (see Figure 2). Figure 4(a) shows that the spatial distribution of the molecular gas component in NGC 6781 seen via  $\text{H}_2$  emission is very similar to that of the cool, low I.P. gas component seen via  $[\text{N II}]$  emission (and also via  $\text{H}\alpha$  emission; Figure 2). The same similarities in the spatial distributions are seen between the dust and ionized gas components delineating the nearly pole-on cylindrical barrel structure (Figure 3 of HerPlaNS1). Highly localized distributions of the molecular gas component are apparent from the filamentary appearance of the  $\text{H}_2$  emission (Figure 4(b)). These  $\text{H}_2$  filaments (and maybe clumps, too) are patches of  $\text{H}_2$  that survived in the ionized region.

### 3.2.2. Physical Conditions: Shocks versus UV Radiation

Table 4 summarizes near- and mid-IR  $\text{H}_2$  lines detected in NGC 6781. As reported by Phillips et al. (2011) and Mata et al. (2016), pure rotational  $\text{H}_2$  lines are detected in the *Spitzer*/IRS spectra (Figure 1, inset). Observations made by Arias & Rosado (2002) show that the intensity of  $\text{H}_2\ v = 2 - 1\ \text{S}(1)$  at  $2.248\ \mu\text{m}$  is much fainter than that of  $\text{H}_2\ v = 1 - 0\ \text{S}(1)$  at  $2.122\ \mu\text{m}$ , which indicates collisional excitation. The kinematic studies of Hiriart (2005) pointed to a post-shock origin for the  $\text{H}_2$  emission. If the observed  $\text{H}_2$  lines are radiatively excited through the absorption of far-UV photons ( $\sim 11\text{--}13\ \text{eV}$ ) in PDRs, the upper vibrational level would have to have a larger population, resulting in a relatively high  $\text{H}_2\ I(2.248\ \mu\text{m})/I(2.122\ \mu\text{m})$  via UV fluorescence (e.g., Kwok 2007). Collisional excitation, on the other hand, can occur in both shocks and PDRs. Excitation mechanisms of  $\text{H}_2$  in PNe are examined by evaluating the  $\text{H}_2\ I(2.248\ \mu\text{m})/I(2.122\ \mu\text{m})$  ratio (e.g., Otsuka et al. 2013), even though it is not easy to do with  $K$ -band data alone.

Interestingly, the expansion velocity of  $\text{H}_2$  ( $\sim 22\ \text{km s}^{-1}$ ; Arias & Rosado 2002; Hiriart 2005) is found to be greater than

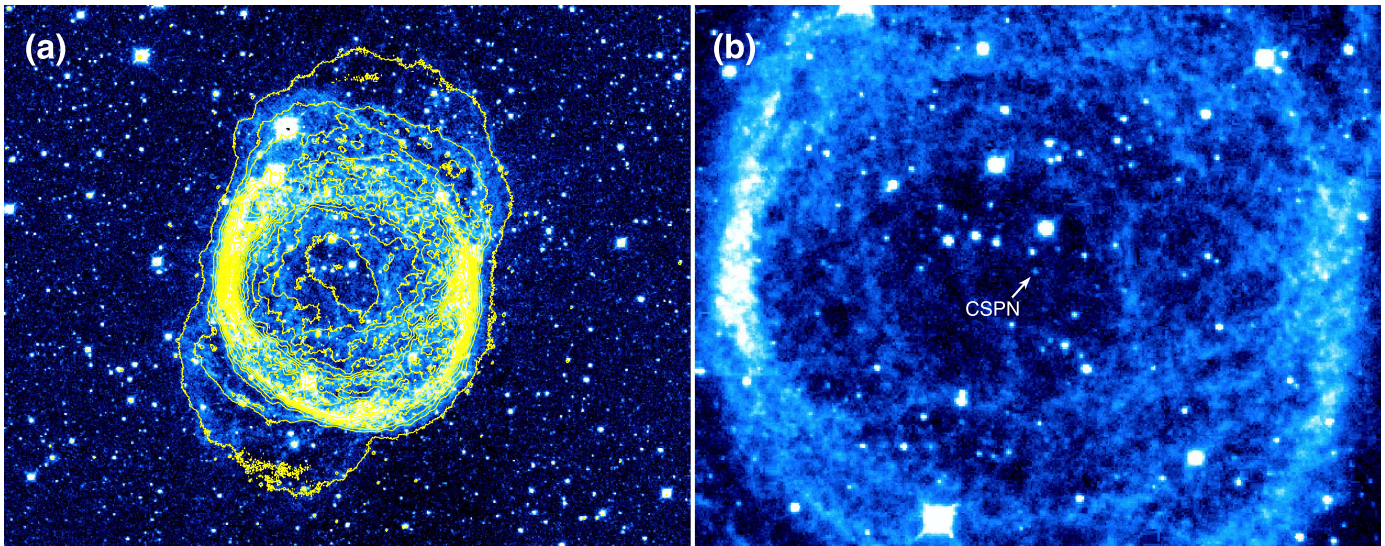


**Figure 4.** (a) Narrowband image of  $\text{H}_2 \nu = 1 - 0 \text{ S}(1)$  at  $2.122 \mu\text{m}$  taken with the 3.6 m CFHT/WIRCAM, overlaid with yellow contours of  $[\text{N II}] \lambda 6583$  emission taken with the 2.5 m NOT/ALFOSC (Phillips et al. 2011; provided to us by M. A. Guerrero). (b) Close-up of the central part of the nebula, showing the filamentary structure of the  $\text{H}_2$  emission in the central region, from which the adopted spectra arose. The location of the central star is also indicated.

**Table 4**

Average  $\text{H}_2$  Intensities of NGC 6781 Measured with *Spitzer*/IRS (See Also Figure 1)

$\lambda$ ( $\mu\text{m}$ )	Transition	Average Intensity ( $\text{erg s}^{-1} \text{cm}^{-2} \text{sr}^{-1}$ )
17.04	0-0 S(1)	$1.90(-5) \pm 5.83(-6)$
12.29	0-0 S(2)	$1.10(-5) \pm 1.08(-6)$
9.67	0-0 S(3)	$5.31(-5) \pm 8.50(-6)$
8.02	0-0 S(4)	$4.00(-5) \pm 4.90(-6)$
6.91	0-0 S(5)	$1.08(-4) \pm 2.63(-5)$
6.11	0-0 S(6)	$3.56(-5) \pm 5.34(-6)$
5.51	0-0 S(7)	$6.19(-5) \pm 1.43(-5)$
2.12 <sup>a</sup>	1-0 S(1)	$2.70(-4)$

**Note.**

<sup>a</sup> The  $\text{H}_2 \nu = 1-0 \text{ S}(1)$  data are from Hiriart (2005).

the expansion velocity measured from the  $[\text{O III}]$  line ( $10 \text{ km s}^{-1}$ ; Weinberger 1989) and  $[\text{N II}]$  line ( $12 \text{ km s}^{-1}$ ; Arias & Rosado 2002). Hiriart (2005) concluded that the average  $\text{H}_2 \nu = 1 - 0 \text{ S}(1)$  surface brightness could be explained by shocks at  $10\text{--}24 \text{ km s}^{-1}$  heading into the pre-shock region of the  $\text{H}_2$  density at  $3400\text{--}14,900 \text{ cm}^{-3}$ .

We investigate the conditions in the  $\text{H}_2$ -emitting regions by comparing the flux ratios of mid-IR  $\text{H}_2$  lines to the  $\nu = 0 - 0 \text{ S}(3)$  line at  $9.67 \mu\text{m}$  with the theoretical continuous shock (C-shock) models by Flower & Pineau (2010). The observed  $I(17.04 \mu\text{m})/I(9.67 \mu\text{m})$  ratio suggests a match for a model with the shock velocity of  $V_s = 10 \text{ km s}^{-1}$  and pre-shock hydrogen density of  $n_s(\text{H}) = 200,000 \text{ cm}^{-3}$ , while the observed  $I(12.29, 8.02, 6.91, 6.11, 5.51 \mu\text{m})/I(9.67 \mu\text{m})$  ratios point to a model with  $V_s = 20 \text{ km s}^{-1}$  and  $n_s(\text{H}) = 20,000 \text{ cm}^{-3}$ . Here, the possible line flux contamination from the  $\text{H I } 12.3 \mu\text{m}$  line to the  $\text{H}_2 12.29 \mu\text{m}$  line, estimated to be  $I(\text{H I } 12.3 \mu\text{m}) = 0.971$  when  $I(\text{H}\beta) = 100$  in the case of  $T_e = 10^4 \text{ K}$  and  $n_e = 200 \text{ cm}^{-3}$ , is removed.

Bachiller et al. (1993) reported a CO expansion velocity of  $22 \text{ km s}^{-1}$ . Recently, Bergstedt (2015) reported a velocity of  $16 \text{ km s}^{-1}$  via 3D structure modeling using CO velocity maps. A model by Flower & Pineau (2010) with a shock velocity of

$V_s = 30 \text{ km s}^{-1}$  and pre-shock hydrogen density of  $n_s(\text{H}) = 20,000 \text{ cm}^{-3}$  would explain the observed far-IR CO line flux ratios with respect to the  $\text{CO } J = 7 - 6$  line at  $371.6 \mu\text{m}$  obtained from our *Herschel* PACS and SPIRE spectra (HerPlaNS1).

Based on the arguments above, excitation of  $\text{H}_2$  and CO lines in NGC 6781 appears to be caused by thermal shocks at a velocity in the range of  $10\text{--}30 \text{ km s}^{-1}$  impinging onto the pre-shock region at  $n_s(\text{H}) \sim 20,000\text{--}200,000 \text{ cm}^{-3}$ . These shocks may be the consequence of interactions between the slow AGB wind and fast PN wind emanating from the CSPN in the context of the PN evolution. The slow-fast wind interactions could cause diffuse X-ray emission in the interaction regions. No X-ray detection in NGC 6781 may thus be because of extinction (see Section 4.2.8). Together with the filamentary/clumpy appearance of the  $\text{H}_2$  emission regions (Figure 4), we would conclude that these structures represent high-density regions delineating the locations of thermal collisional excitation embedded in a lower-density ionized gas. Such high  $\text{H}_2$  clumps (so-called ‘‘cometary knots’’; O’Dell & Handron 1996) within the ionized gas are detected in nearby PNe (see, e.g., O’Dell et al. 2002). Recently, Machado et al. (2015) detected cometary  $\text{H}_2$  knots within the ionized gas region in the bipolar PN NGC 2346.

One might think that the  $\text{H}_2$  distribution in NGC 6781 is similar to that in NGC 7293 (Helix Nebula), in which the  $\text{H}_2$  emission is considered to arise from  $\text{H}_2$  clumps. For NGC 7293, there is no evidence to suggest that the  $\text{H}_2$  emission from its cometary knots is due to shocks (Aleman et al. 2011, and references therein). Another possible  $\text{H}_2$  excitation mechanism is due to the structure and steady-state dynamics of advective ionization front/dissociation front (Henney et al. 2007). However, our Cloudy models with turbulence velocity of  $\leq 10 \text{ km s}^{-1}$  in the nebula by following Henney et al. (2007) failed to reproduce the observed  $\text{H}_2$  line fluxes. While these are definitely issues that need to be resolved in the future, we tentatively conclude that the observed  $\text{H}_2$  emission in NGC 6781 has a shock origin based on the arguments presented above.



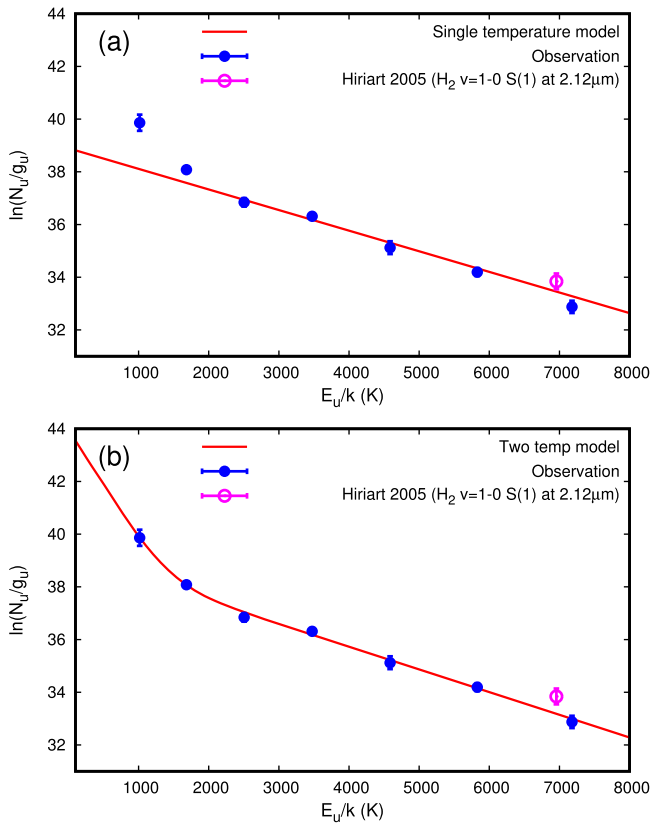


**Figure 5.** Excitation diagram of pure rotational transitions of H<sub>2</sub> lines. We fit the observed data (Table 4) with (a) a single excitation temperature (with all but the 17.04 μm line;  $T(\text{H}_2) = 1279 \pm 109$  K) and (b) two excitation temperatures (with all lines;  $T(\text{H}_2) = 1161 \pm 72$  K and  $236 \pm 50$  K).

### 3.2.3. Physical Conditions: H<sub>2</sub> Excitation Diagram

Assuming that H<sub>2</sub> lines are thermally excited and are in local thermodynamic equilibrium (LTE), the H<sub>2</sub> excitation temperature and column density can be estimated via an excitation diagram. The H<sub>2</sub> column density  $N_u$  in the upper state is written as

$$N_u = \frac{4\pi I(\text{H}_2)}{A} \cdot \frac{\lambda}{hc}, \quad (5)$$

where  $I(\text{H}_2)$  is the H<sub>2</sub> line intensity in  $\text{erg s}^{-1} \text{cm}^{-2} \text{sr}^{-1}$ ,  $A$  is the transition probability taken from Turner et al. (1977),  $h$  is the Planck constant, and  $c$  is the speed of light. In LTE, the Boltzmann equation relates  $N_u$  to the excitation temperature  $T(\text{H}_2)$  via

$$\ln\left(\frac{N_u}{g_u}\right) = -\frac{E_u}{kT(\text{H}_2)} + \ln\left[N(\text{H}_2) \cdot \frac{hcB}{2kT(\text{H}_2)}\right], \quad (6)$$

where  $g_u$  is the vibrational degeneracy,  $E_u$  is the energy of the excited level taken from Dabrowski (1984),  $k$  is the Boltzmann constant, and  $B$  is the rotational constant ( $60.81 \text{ cm}^{-1}$ ).

In Figure 5, we plot the  $\ln(N_u/g_u)$  versus  $E_u/k$  for each of the H<sub>2</sub> lines detected in NGC 6781 (Table 4). The  $E_u/k$  of the H<sub>2</sub>  $v = 2 - 1$  S(1) (magenta circle) is calculated using the average line intensity of  $2.7(-4) \text{ erg cm}^{-2} \text{ s}^{-1} \text{ sr}^{-1}$  (Hiriart 2005). The rotational diagram suggests that the bulk of the H<sub>2</sub> 17.04 μm line emission is produced in a region with different physical conditions from the other H<sub>2</sub> line emitting regions.

First, we determine the conditions of the H<sub>2</sub>-emitting region by fitting the line fluxes at 12.29, 9.67, 8.02, 6.91, 6.11, 5.51, and 2.12 μm (i.e., all but 17.04 μm) with Equation (6) using a single excitation temperature (Figure 5(a)):  $T(\text{H}_2) = 1279 \pm 109$  K and  $N(\text{H}_2) = (2.28 \pm 0.49)(18) \text{ cm}^{-2}$ . The derived  $T(\text{H}_2)$  is comparable to 978 K and  $880 \pm 70$  K, previously derived by Phillips et al. (2011) and Mata et al. (2016), respectively (with a single-temperature model using all but the 2.12 and 17.04 μm lines).

Next, we fit all H<sub>2</sub> lines (including 17.04 μm) using two excitation temperatures (Figure 5(b)). The warm component is found to have  $T(\text{H}_2) = 1161 \pm 72$  K and  $N(\text{H}_2) = (2.72 \pm 0.53)(18) \text{ cm}^{-2}$ , whereas the cold component is found to have  $T(\text{H}_2) = 236 \pm 50$  K and  $N(\text{H}_2) = (6.67 \pm 4.89)(19) \text{ cm}^{-2}$  (while lack of the H<sub>2</sub> 0-0 S(0) line at 28.2 μm makes the fitting results relatively less certain). Nonetheless, the 17.04 μm line is expected to arise from such colder and denser regions.

### 3.2.4. Empirically Determined Molecular Gas Mass

To conclude this subsection, we estimate the mass of the molecular gas component in the nebula by adopting the distance of 0.46 kpc (Section 3.4.1). Based on the H<sub>2</sub> and CO emission maps (Hiriart 2005; Bachiller et al. 1993, respectively), we see that molecular emission increases at  $\sim 54''$ – $55''$  away from the CSPN with the thickness of  $12''$ . Using H<sub>2</sub> densities of the warm and cold components as derived above ( $N(\text{H}_2) = 2.72(18) \text{ cm}^{-2}$  and  $6.67(19) \text{ cm}^{-2}$ , respectively), we estimate the H<sub>2</sub> gas mass of  $2.5(-3) M_\odot$  and  $6.2(-2) M_\odot$  for the warm and cold components, respectively.

Previously, we derived  $N(\text{CO}) = 10^{14.70-15.08} \text{ cm}^{-2}$  (excitation temperature at  $\sim 60$  K) based solely on our *Herschel* spectra (HerPlaNS1). Bachiller et al. (1997) measured  $N(\text{CO}) = 10^{16.16} \text{ cm}^{-2}$  (excitation temperature at  $\sim 25$  K) based on submillimeter data. Assuming that each of the above  $N(\text{CO})$  estimates based on data in the different wavelength/temperature realms would represent the warm and cold component, respectively, the warm and cold CO gas masses are estimated to be  $4.6(-6) M_\odot$  and  $6.6(-5) M_\odot$ , respectively. These estimates are combined to yield the total molecular gas mass (of H<sub>2</sub> and CO) of  $6.46(-2) M_\odot$ .

The empirical  $N(\text{CO})/N(\text{H}_2)$  ratio turns out to be 2.19(-4) and 4.37(-4) for the warm and cold temperature regions, respectively. Assuming that the  $N(\text{CO})/N(\text{H}_2)$  ratio translates roughly to  $2 \times n(\text{C})/n(\text{H})$ , we can estimate  $\epsilon(\text{C})$  of 8.04–8.34 for the molecular gas component. Compared with the adopted CEL expected  $\epsilon(\text{C})$  of 8.56–9.00 for the ionized gas component,  $\sim 11\%$ – $60\%$  of the C atoms were estimated to be locked in as molecules.

### 3.3. The Dust Component: Summary of HerPlaNS I

The surface brightness distribution of thermal dust continuum emission from NGC 6781 is spatially resolved in far-IR *Herschel* broadband images (see Figure 3 of HerPlaNS1). The bright ring structure with  $\sim 60''$  outer radii represents the bulk of the nearly pole-on cylindrical barrel structure (originally proposed by Schwarz & Monteiro 2006), and the elongated nebula of  $\sim 200''$  in the total north–south extent indicates the distribution of dust along the polar axis of the nebula. The spatial extent of thermal dust continuum emission in far-IR wavelengths is nearly identical with that of atomic gas and molecular emission lines in optical and near-IR wavelengths.



Previously, we performed spectral energy distribution (SED) fitting of the *Herschel* 70/160/250/350/500  $\mu\text{m}$  images using a modified blackbody function and found that dust grains are composed mostly of amorphous-carbon-based material (i.e., the power-law dust emissivity index  $\beta$  is  $\sim 1$  across the nebula) having the dust temperature  $T_d$  in the range between 26 and 40 K (HerPlaNS1). Moreover, after removing the contribution to the continuum flux in the far-IR by fine-structure lines and molecular emission lines (amounts to 8%–20% of the total flux), spectral fitting of the integrated far-IR fluxes yielded  $T_d = 37 \pm 5$  K and  $\beta = 0.9 \pm 0.3$ . Indeed, the *Spitzer*/IRS spectrum (Figure 1, inset) shows PAH bands and featureless dust continuum. This is consistent with the dusty nebula of NGC 6781 containing more amorphous carbon dust and PAHs than amorphous silicate dust.

### 3.4. The Central Star

#### 3.4.1. Distance, Luminosity, and Effective Temperature

A vast variety of distance estimates are proposed for NGC 6781, including 0.3 kpc (Tajitsu & Tamura 1998; Phillips 2002), 0.7 kpc (Stanghellini et al. 2008; Frew et al. 2016), 0.9 kpc (Maciel 1984), 0.95 kpc (Schwarz & Monteiro 2006), and 1.27 kpc (Ali et al. 2013), to name a few. For the present study, rather than adopting any of the previous investigations, we elect to determine our own value by comparing the observed photometry of the CSPN (Figure 1, Table 11) with the post-AGB evolutionary tracks produced by Vassiliadis & Wood (1994) augmented with a grid of synthesized spectra by Rauch (2003). Although several new evolutionary tracks have been produced since then, there have been no AGB nucleosynthesis models constructed based on such new tracks. In comparing observed data with theoretical models, we would regard internal consistencies between models more important. Especially when we aim at determining the state of evolution of the CSPN of NGC 6781, the most critical is adopting AGB nucleosynthesis models that are consistent with evolutionary tracks. Therefore, in the following discussion, we adopt the AGB nucleosynthesis models by Karakas (2010) based on Vassiliadis & Wood (1994).

We start by estimating the CSPN luminosity  $L_*$  using a grid of non-LTE line-blanketed plane-parallel hydrostatic atmospheric models generated by Rauch (2003) as templates. We adopt the solar abundance ( $Z = 0.02$ ) models for the CSPN based on the results of our own nebular abundance analysis presented in Section 3.1.5.

To characterize the stellar atmosphere fully, we also need the effective temperature  $T_{\text{eff}}$  and surface gravity  $\log g$  of the CSPN. Previously, Rauch et al. (2004) suggested  $T_{\text{eff}} = 80,000$  K and  $\log g = 6.0 \text{ cm s}^{-2}$  based on the stellar absorption line fitting. If this  $T_{\text{eff}}$  were true, the CSPN would have been still burning hydrogen in a thin surface layer while increasing  $T_{\text{eff}}$ . However, detection of strong He II  $\lambda 4686$  and [O IV] 25.88  $\mu\text{m}$  lines in the ISIS and *Spitzer*/IRS spectra, respectively (Figure 1 and Table 12) requires  $T_{\text{eff}} > 80,000$  K, refuting the previous suggestion. The noisy spectrum due to the faintness of the CSPN might have compromised the previous absorption line fitting analysis.

Thus, we decide to look for the appropriate  $T_{\text{eff}}$  and  $\log g$  values in a PN similar to NGC 6781 in terms of nebula and CSPN properties. Among Galactic PNe, NGC 6720 is very similar to NGC 6781 in many respects, especially in their

abundance pattern, as shown in Table 5. Spectroscopically, both PNe show PAH features and pure rotational  $\text{H}_2$  lines in their *Spitzer*/IRS spectra (Phillips et al. 2011; Cox et al. 2016), as well as rotational-vibrational  $\text{H}_2$  emission (e.g., Hiriart 2005; van Hoof et al. 2010). Both PNe possess a structure due to a heavy equatorial concentration (i.e., a generic bipolar/barrel shape) viewed nearly pole-on (Schwarz & Monteiro 2006; Sahai et al. 2012; Ueta et al. 2014).

The CSPN of NGC 6720 has a  $T_{\text{eff}} > 100$  kK based on the absorption-line analysis done by McCarthy et al. (1997) and Napiwotzki (1999). Thus, based on the similarities listed above, we adopt  $T_{\text{eff}} = 110\text{--}140$  kK and  $\log g = 6.9 \text{ cm s}^{-2}$  for the CSPN of NGC 6781 as well. Consistent results were previously obtained from detailed SED fitting with Cloudy photoionization models of NGC 6720 (van Hoof et al. 2010; see also Section 4).

Then, we scale the synthesized Rauch model spectra of the adopted CSPN characteristics of  $T_{\text{eff}} = 110\text{--}140$  kK with a constant 10 kK step with  $\log g = 6.9 \text{ cm s}^{-2}$  fixed so that the observed photometry from the WFC  $u$  band to WFCAM  $K$  band (see Table 11) matches with the model spectra (Figure 6, showing the  $T_{\text{eff}} = 120$  kK case). The scaled spectra are integrated to yield  $L_*$ , which is then parameterized with  $T_{\text{eff}}$  and the distance  $D$  in the form of

$$L_*(D, T_{\text{eff}}) = [2.29(-7) \cdot T_{\text{eff}}^2 - 4.39(-2) \cdot T_{\text{eff}} + 2510] \cdot D^2, \quad (7)$$

where  $D$  is in kpc and  $T_{\text{eff}}$  is in K. Note that  $L_*$  is not very sensitive to  $\log g$ . For instance,  $L_*$  increases only by  $\sim 0.8\%$  when  $\log g$  is reduced from the adopted  $6.9 \text{ cm s}^{-2}$  to  $6.6 \text{ cm s}^{-2}$ . Thus, our choice of single  $\log g$  value is warranted.

Finally, we compute  $L_*(D, T_{\text{eff}})$  at  $T_{\text{eff}} = 110\text{--}140$  kK and for a range of  $D$  and plot the resulting  $(L_*, T_{\text{eff}})$  pairs over the post-AGB evolutionary tracks of the 1.5, 2.25, 2.5, and 3.0  $M_{\odot}$  initial-mass stars produced by Vassiliadis & Wood (1994), as shown in Figure 7. Our choice of the initial mass of the adopted post-AGB evolutionary tracks is dictated by the results of our abundance analysis that indicated the CSPN initial mass being between 2.25 and 3.0  $M_{\odot}$  (Section 3.1.5). Also, the previous analysis by Schwarz & Monteiro (2006) suggested a CSPN initial mass of 1.5  $M_{\odot}$ .

We find that  $D = 0.34\text{--}0.52$  kpc fits the initially 2.25–3.0  $M_{\odot}$  post-AGB evolutionary tracks the best for the adopted  $T_{\text{eff}}$  range (light-blue box in Figure 7). Therefore, we adopt  $D = 0.46$  kpc, which is the intermediate value between 0.34 and 0.52 kpc (red circles in Figure 7). Accordingly, we find  $L_* = 104\text{--}196 L_{\odot}$ . This evolutionary track fitting suggests that the CSPN of NGC 6781 is in the cooling phase. The results of the fitting are not significantly altered even when we adopt more recent post-AGB evolution tracks such as the ones computed by Miller Bertolami (2016) ( $D = 0.46$  kpc, using the post-AGB evolutionary tracks for 2.0 and 3.0  $M_{\odot}$  stars with  $Z = 0.02$ ; see also Figure 12).

Previously, Schwarz & Monteiro (2006) concluded that the progenitor of NGC 6781 was a  $1.5 \pm 0.5 M_{\odot}$  initial-mass star based on their derived  $L_*$  and  $T_{\text{eff}}$  values, provided that  $D = 0.95$  kpc as suggested from their photoionization model fitting (black triangle in Figure 7; also suggesting that NGC 6781 was in cooling phase). At  $D = 0.95$  kpc, our  $L_*$  estimates would be consistent with the 1.5  $M_{\odot}$  evolutionary track (blue squares in Figure 7). However, the progenitor CSPN mass of NGC 6781 would most likely exceed 1.5  $M_{\odot}$ .

**Table 5**  
Similarities between NGC 6781 and NGC 6720

PNe	$\epsilon(\text{He})$	$\epsilon(\text{C}_{\text{RL}})$	$\epsilon(\text{C}_{\text{CEL}})$	$\epsilon(\text{N})$	$\epsilon(\text{O}_{\text{RL}})$	$\epsilon(\text{O}_{\text{CEL}})$	$\epsilon(\text{Ne})$	$\epsilon(\text{S})$	$\epsilon(\text{Cl})$	$\epsilon(\text{Ar})$	$T_{\text{eff}}$ (kK)	$\log g$ ( $\text{cm s}^{-2}$ )	References
NGC 6781	11.06	9.61	8.56–9.00	8.15	...	8.76	8.15	6.91	5.16	6.49	80–123	6.0–7.0	1, 2, 3, 4
NGC 6720	11.05	9.10	8.59	8.22	9.18	8.80	8.23	6.86	5.19	6.54	80–135	6.9–7.0	5, 6, 7

**References.** (1) This work for abundances (see Section 3.1.3); (2) Schwarz & Monteiro 2006, for  $T_{\text{eff}}$  and  $\log g$  via photoionization modeling; (3) Rauch et al. 2004, for  $T_{\text{eff}}$  and  $\log g$  via stellar absorption fitting; (4) Liu et al. 2004a, for abundances; (5) McCarthy et al. 1997, for  $T_{\text{eff}}$  and  $\log g$  via stellar absorption fitting; (6) Napiwotzki 1999, for  $T_{\text{eff}}$  and  $\log g$  via stellar absorption fitting; (7) van Hoof et al. 2010, for  $T_{\text{eff}}$  via Cloudy photoionization modeling.

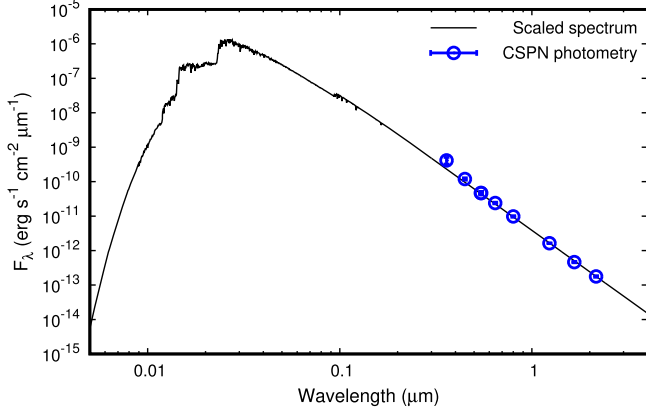


**Figure 6.** Synthesized spectrum of a star with  $Z = 0.02$ ,  $T_{\text{eff}} = 120$  kK, and  $\log g = 6.9$   $\text{cm s}^{-2}$  (Rauch 2003; black solid line) fit with the observed photometry points of the CSPN (blue circles; Table 11).

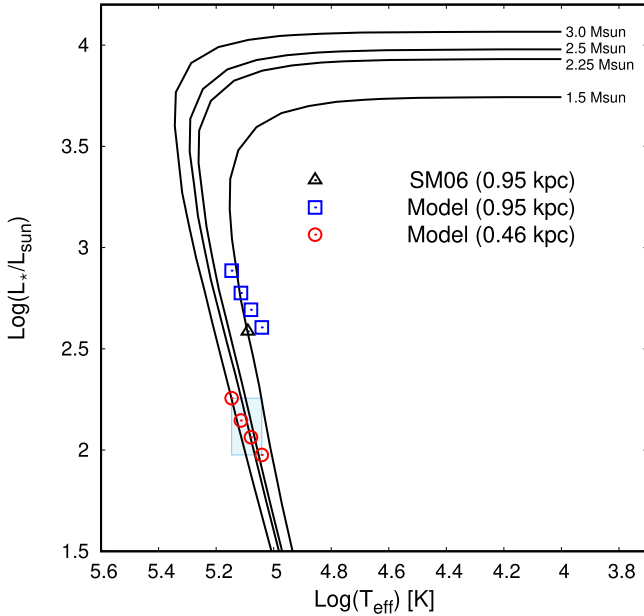


**Figure 7.** Distance-fitting comparison among the post-AGB evolutionary model tracks of 1.5, 2.25, 2.5, and  $3.0 M_{\odot}$  initial-mass stars (Vassiliadis & Wood 1994) and the CSPN luminosity,  $L_*(D, T_{\text{eff}})$ , computed for  $D = 0.95$  and  $0.46$  kpc (blue squares and red circles, respectively) and  $T_{\text{eff}} = 110, 120, 130$ , and  $140$  kK (from right to left, respectively), when  $\log g = 6.9$   $\text{cm s}^{-2}$ . Also shown is the  $L_* - T_{\text{eff}}$  pair adopted by Schwarz & Monteiro (2006), with which they concluded  $D = 0.95$  kpc (black triangle). The light-blue box indicates the  $L_* - T_{\text{eff}}$  parameter range based on our Cloudy model calculations (Section 4) at  $D = 0.46$  kpc. See also Figure 12.

because of its empirically determined elemental abundances (Section 3.1.3) and  $\text{H}_2$  detection in this object (Section 3.2.2).

With a survey of  $\text{H}_2 v = 1 - 0$  S(1) emission in Galactic PNe, Kastner et al. (1996) suggested that  $\text{H}_2$ -rich PNe evolved

from relatively massive progenitors because  $\text{H}_2$  was exclusively detected in bipolar PNe (see also, e.g., Guerrero et al. 2000). Bipolar PNe are known to be associated with massive ( $\geq 1.5 M_{\odot}$ ) progenitors based on the distribution of bipolar PNe in the Milky Way with respect to that of elliptical PNe (Corradi & Schwarz 1995). Hence, the detection of  $\text{H}_2$  supports our adaptation of the  $2.25\text{--}3.0 M_{\odot}$  initial mass for the CSPN of NGC 6781 and the distance of  $0.46$  kpc based on the  $L_*(D, T_{\text{eff}})$  fitting.

The filamentary appearance of the nebula (Figure 4) and low  $n_e$  even in the central ionized regions (Section 3.1.1) are also suggestive that NGC 6781 is a highly evolved PN. Referring back to the similarity to NGC 6720, comparisons between  $L_*$  and  $T_{\text{eff}}$ , where  $L_*$  is based on Cloudy model fitting of the SED by van Hoof et al. (2010) with the evolutionary tracks by Vassiliadis & Wood (1994) for initially  $3.0 M_{\odot}$  stars of  $Z = 0.02$ , also suggest that NGC 6720 is in the cooling phase.

If the CSPN of NGC 6781 were still in the final H-burning phase, the distance estimate would have to be  $\gtrsim 3.6$  kpc. According to Vassiliadis & Wood (1994),  $L_*$  is nearly constant at  $\sim 6300 L_{\odot}$  along the horizontal part of the post-AGB track for a  $2.5 M_{\odot}$  initial-mass star with  $Z = 0.02$ . In this case, the number of the ionizing photons is  $4.25(+47)\text{s}^{-1}$  for  $T_{\text{eff}} = 120,000$  K and  $\log g = 6.9$   $\text{cm s}^{-1}$ . The Strömgren radius for this radiation field in a constant hydrogen density of  $300 \text{ cm}^{-3}$  (see Table 2, Figure 8) with a filling factor ( $f$ ) of unity would be  $\sim 0.41$  pc. This corresponds to the apparent radius of  $23''.7$  at  $D = 3.6$  kpc, which disagrees with the observed ionization radius of  $\sim 55''$ . Because the Strömgren radius is proportional to  $f^{-1/3}$ , it would be consistent with the observed ionization radius at  $D = 3.6$  kpc if  $f$  were  $0.12$ . However, according to the empirical method introduced by Mallik & Peimbert (1988), the  $f$  value of NGC 6781 is estimated to be  $\sim 0.4$  at  $D = 3.6$  kpc and almost unity at  $0.46$  kpc. Therefore, we conclude that the CSPN of NGC 6781 already evolved off to the cooling track currently with  $L_* = 104\text{--}196 L_{\odot}$  and  $T_{\text{eff}} = 110\text{--}140$  kK at  $D = 0.46$  kpc.

### 3.4.2. Possibility of the Presence of a Binary Companion

At present, binary evolution would appear to be one of the most viable explanations for the formation of bipolar nebulae via the inevitable equatorial density enhancement (e.g., Jones & Boffin 2017). Our motivation to collect photometry measurements of the CSPN exhaustively in the UV to near-IR is also intended to establish the presence or absence of a near-IR excess, which would suggest the presence of a cooler binary companion.

From a comparison between the observed colors ( $V - I$  and  $I - J$ ) and the grid of theoretical color indices as a function of  $T_{\text{eff}}$ , Douchin et al. (2015) argued that CSPN of NGC 6781 shows near-IR excess owing to an M1- to M7-type companion

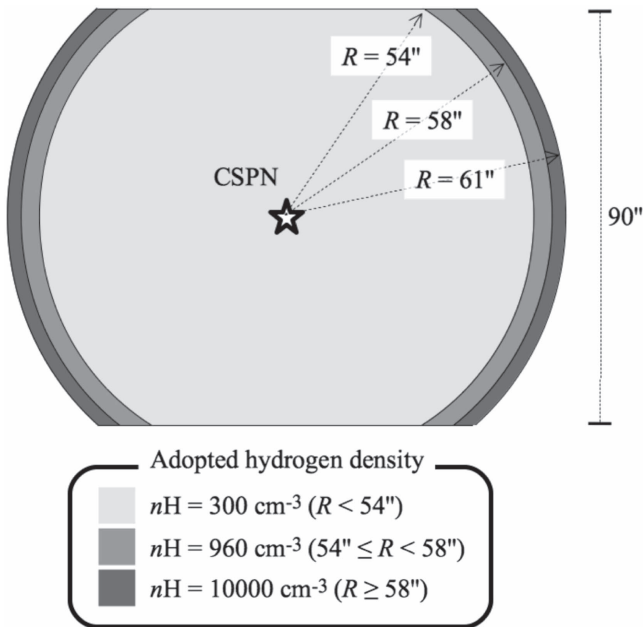


**Figure 8.** Adopted geometry and hydrogen density ( $n(\text{H})$ ) profile of NGC 6781 in the Cloudy model.

star. However, we do not observe any IR excess in the SED of the CSPN (Figures 1 and 6).

It is true that the IR excess detection can be influenced by the way the interstellar extinction is corrected for. With our adopted  $c(\text{H}\beta) = 1.007$ , the extinction-corrected  $V-I$  and  $I-J$  colors of the CSPN were  $-0.44$  and  $-0.90$ , respectively. If we used  $E(B - V) = 0.56$  (corresponding to  $c(\text{H}\beta) = 0.82$ ) as adopted by Douchin et al. (2015), the respective  $V-I$  and  $I-J$  colors would become redder,  $-0.27$  and  $-0.61$ , which would be in perfect agreement with Douchin et al. (2015). This would negate the necessity for an M1- to M7-type companion star.

Thus, whether NGC 6781 possesses a binary central system is still an open question because the evolutionary effects from the secondary, even if it existed, would still be negligible at this point, based on the observed spectra and photometry. Therefore, we would simply keep the adopted  $D = 0.46$  kpc and other quantities for which there is distance dependency in our analyses as outlined in the previous sections and in the subsequent modeling section.

## 4. Cloudy Dusty Photoionization Models

### 4.1. Modeling Approach

In the previous sections, we outlined how we mustered the most comprehensive observational data set yet assembled for NGC 6781 (Section 2) and performed various analyses to determine empirically the CSPN and nebula characteristics for this object (Section 3). In this section, we outline how we construct a *realistic* input numerical model of NGC 6781 for Cloudy (version C13.03; Ferland et al. 2013), comprising the CSPN and the nebula, the latter of which consists of the ionized/neutral/molecular gas and dust components, based on the collected data.

Our aim is to converge on *self-consistent* physical conditions of the entire NGC 6781 system from the highly ionized region to the PDR through iterative model fitting that *comprehensively* reproduces *all* of the observational data that we collected: the spatially integrated fluxes and flux densities from UV to radio

(37 broadband photometry fluxes, 19 flux densities, and 78 emission-line fluxes) plus eight elemental abundances. The empirically derived quantities of the CSPN and nebula provide the input parameters, while the observational data from the UV to radio provide the vital constraints in iterative fittings of the model parameters. For the sake of consistency, we substituted the same transition probabilities and effective collision strengths of CELs used in our plasma diagnostics and nebular abundance analyses in the Cloudy code.

### 4.2. The Input Model

#### 4.2.1. SED of the CSPN

As the incident SED from the CSPN, we adopt the theoretical atmospheric model grid by Rauch (2003) for a star with  $Z = 0.02$  and  $\log g = 6.9 \text{ cm s}^{-2}$  (see Figure 6 for the case of  $Z = 0.02$ ,  $\log g = 6.9 \text{ cm s}^{-2}$ , and  $T_{\text{eff}} = 120 \text{ kK}$ ). We keep the distance of 0.46 kpc to NGC 6781 and vary  $T_{\text{eff}}$  and  $L_*$  within the possible ranges,  $L_* = 104\text{--}196 L_\odot$  and  $T_{\text{eff}} = 110\text{--}140 \text{ kK}$ , as determined in Section 3.4, during the iterative model fitting to search for the best-fit model parameters that would reproduce the observational data.

#### 4.2.2. Nebular Elemental Abundances

For the elemental abundances of the nebula, we adopt the empirically determined abundances (Table 3; Section 3.1) as the input values. The nebular abundances are then refined via model iterations within  $\pm 3\sigma$  of the input values so that the best-fit abundances would reproduce the observed emission line intensities.

It should be pointed out here that the metal abundances would affect cooling of the nebula and hence would alter the nebula's temperature and ionization structures. As we saw in Section 3.1.3, the derivation of the C abundance is definitely a source of uncertainties. The only option of the empirical derivation available to us suggests the expected CEL C abundance  $\epsilon(\text{C})$  of 8.56–9.00 (Table 3). Hence, for the purpose of the present modeling, we set  $\epsilon(\text{C})$  to be at the lower limit of 8.56 and keep it fixed during the model iteration. This will ensure that the best-fit model always satisfies at least the lower limit of the progenitor mass of  $2.25 M_\odot$  (see Section 3.1.5).

The expected CEL  $\epsilon(\text{C})$  of 8.56 is also consistent with the AGB nucleosynthesis model for the  $2.25 M_\odot$  stars (Karakas 2010). As we demonstrated in Section 3.4.1, NGC 6781 is very similar to NGC 6720 in terms of the elemental abundance pattern of the nebula and evolutionary state of the CSPN (Table 5). The adopted CEL  $\epsilon(\text{C})$  of 8.56 for NGC 6781 is indeed very much consistent with that of 8.59 for NGC 6720. In addition, we adopt a constant  $^{12}\text{C}/^{13}\text{C}$  ratio of 20 determined by Bachiller et al. (1997).

As for the unobserved elements including heavy metals, we adopt the abundance values predicted with the AGB nucleosynthesis model of the  $2.5 M_\odot$  initial-mass star with  $Z = 0.02$  (Karakas 2010). However, the Fe abundance is another exception, because we overpredict the Fe lines when setting  $\epsilon(\text{Fe}) = 7.53$  as determined by Karakas (2010). The model  $I$  ( $[\text{Fe II}] 17.9 \mu\text{m}$ ) and  $I$  ( $[\text{Fe III}] \lambda 4880$ ) line fluxes turn out to be 31.2 and 2.6 (with respect to  $I(\text{H}\beta) = 100$ ), respectively.

Nevertheless, such strong Fe lines are seen neither in the WHT/ISIS spectrum nor in the *Spitzer*/IRS spectrum. Therefore, we must adopt a lower Fe abundance. Previously, Liu et al. (2004a) measured  $\epsilon(\text{Fe}) = 6.20$  in NGC 6720. Thus, we



adopt  $\epsilon(\text{Fe}) = 6.20$ , following the same similarity argument between NGC 6781 and NGC 6720 as in Section 3.4.1. For other Fe-peak elements such as Cr, Mn, Co, and Ni, we adopt their solar values simply because their elemental abundances are unknown in NGC 6781.

#### 4.2.3. Geometry of the Nebula

Many authors suggested that NGC 6781 possessed a nearly pole-on cylindrical barrel structure, which surrounds the central cavity filled with tenuous highly ionized gas (e.g., Bachiller et al. 1993; Hiriart 2005; Schwarz & Monteiro 2006; Bergstedt 2015, as well as HerPlaNS1). Hence, with the 1D code Cloudy, we represent the barrel wall structure by thin, concentric layers of ionized gas and dusty PDR. Such an “onion skin” configuration naturally explains the observed co-spatial distributions of various components at different temperatures by the projection effect (Figure 4(a)). While clumps/filaments of  $\text{H}_2$  surviving in the ionized region would be plausible (Figure 4(b)), we simply adopt this “onion skin” configuration for the sake of 1D model calculations, assuming that such molecular clumps/filaments would not significantly alter the nebular energetics.

However, we do take into account the barrel geometry of NGC 6781 by invoking the “cylinder” option of Cloudy, which approximates the cylindrical structure by removing polar caps from a hollow sphere (which is the default 1D spherically symmetric configuration). We set the polar height of the cylinder to  $90''$ , which is the average value between  $72''$  (suggested from the velocity channel maps in  $\text{H}_2$ ; Hiriart 2005) and  $117''$  (suggested from the velocity channel maps taken in  $\text{CO } J = 3-2$  at 345.796 GHz [866.96  $\mu\text{m}$ ]; Bergstedt 2015), assuming that the  $\text{H}_2$  and  $\text{CO}$  emission arose from the same regions because of the similarities between  $\text{H}_2$  and  $\text{CO}$  maps (Bachiller et al. 1993; Bergstedt 2015). Figure 8 shows a schematic of the adopted geometry.

#### 4.2.4. Hydrogen Density Radial Profile of the Nebula

The input radial hydrogen density profile,  $n_{\text{H}}(R)$  (where  $R$  is the distance from the CSPN), is adopted from our previous analysis (HerPlaNS1). In the central cavity surrounded by the barrel wall structure ( $R < 54''$ )  $n_{\text{H}}(R) = 300 \text{ cm}^{-3}$ , whereas in the barrel wall ( $54'' \leq R < 58''$ )  $n_{\text{H}}(R) = 960 \text{ cm}^{-3}$  (Figure 8).

Unfortunately,  $n_{\text{H}}(R)$  beyond  $58''$  cannot be determined directly from the observed data, because this radial region is where the surface brightness of the nebula decreases sharply to the detection limit in the narrow- and broadband images of the object (and hence the observational constraints are scarce). Hence, as discussed in Section 3.2.3, we simply adopt a constant density of  $n_{\text{H}}(R) = 10^4 \text{ cm}^{-3}$  beyond  $58''$ . The outer radius is then determined iteratively by increasing the thickness of this dusty PDR layer until the model flux at  $170 \mu\text{m}$  would reproduce the observed value, which is one of our model calculation termination criteria. In the end, the outer radius is set to  $61''$ . The radial density profile of the nebula is also provided in Figure 8.

#### 4.2.5. Constant Pressure Model

One might surmise that the adopted  $n_{\text{H}}(R)$  radial profile would allow for a constant gas pressure model. Therefore, we test a constant gas pressure model, for which we adopt the

average  $\log_{10}(T_e n_e) = 6.81 \text{ K cm}^{-3}$  based on the radial  $T_e$  and  $n_e$  profiles measured previously (HerPlaNS1). The result is similar to the nonconstant gas pressure model, except for He II and [O IV] lines. In order to avoid a collapse of the nebula, the inner radius of the nebula has to be set larger. This correspondingly results in underestimates of the line fluxes of these high I.P. lines. Also, NGC 6781 does not seem to be embedded in a dense ISM region. Because of these reasons, we conclude that the nonconstant gas pressure model that we adopt in the present investigation is a better approximation to NGC 6781 than a constant gas pressure model.

#### 4.2.6. Dust Grains and PAH Molecules

As we summarized in Section 3.3, NGC 6781 is determined to be a PN rich in amorphous carbon. Thus, the nebula’s dusty PDR is expected to consist largely of amorphous carbon (AC) plus neutral (and possibly ionized) PAHs, even though the C-richness of the nebula remains uncertain (see Section 3.1.4). Rouleau & Martin (1991) provided two types of optical constants measured from samples “BE” (soot produced from benzene burned in air) and “AC” (soot produced by striking an arc between two amorphous carbon electrodes in a controlled Ar atmosphere). We test both of these BE and AC amorphous carbon grain models, and we find that the AC-type grain models yield generally better overall fit to the observed mid-IR to far-IR dust continuum. Thus, we adopt the AC-type grain optical constants by Rouleau & Martin (1991). We assume spherical grains and adopt the modified interstellar size distribution (i.e.,  $n(a) \propto a^{-3.5}$ ; Mathis et al. 1977) with  $a = 0.005\text{--}0.50 \mu\text{m}$ , which are divided into 20 bins in model calculations.

For PAHs, we adopt the radius  $a$  in the range of  $0.0004 \mu\text{m}$  (30 C atoms) to  $0.0081 \mu\text{m}$  (250 C atoms) with the same size distribution as dust ( $a^{-3.5}$ ; Mathis et al. 1977), approximating the overall shape by a sphere (separated into the same 20 size bins). We include both the neutral and charged PAH grains. The optical constants for PAH-carbonaceous grains are adopted from the theoretical work by Draine & Li (2007). We permit the stochastic heating mechanism of PAH molecules in model calculations.

#### 4.2.7. Density-bounded versus Ionization-Bounded PNe

Figure 9 shows the SED of the CSPN plus PN based on the observed photometry from GALEX  $0.22 \mu\text{m}$  to radio 1.4 GHz (Table 1; Figure 1). Using this empirical SED, we measure the integrated luminosity of  $114 L_{\odot}$  at  $D = 0.46 \text{ kpc}$  for the CSPN plus PN. The contribution to this SED only from the CSPN for the wavelength range of  $\gtrsim 0.2 \mu\text{m}$  is estimated to be  $4.6 L_{\odot}$ . Hence, the remainder has to come from the nebula, i.e.,  $L_{\text{Neb}} \approx 110 L_{\odot}$ .

As for the luminosity of the CSPN, we already determined the empirical value of  $L_* = 104\text{--}196 L_{\odot}$  based on Equation (7) (Section 3.4.1). Thus, NGC 6781 could be a density-bounded PN (i.e.,  $L_{\text{Neb}} < L_*$ ) as previously claimed by Schwarz & Monteiro (2006). However, the fact that NGC 6781 possesses massive molecular gas and dust components indicates that it is more likely an ionization-bounded PN (i.e.,  $L_{\text{Neb}} \approx L_*$ ). Realistically speaking, whether a PN is density- or ionization-bounded is not necessarily straightforward, because both situations could be present in one PN. In bipolar PNe such as NGC 6781, both ionization- and density-bounded conditions

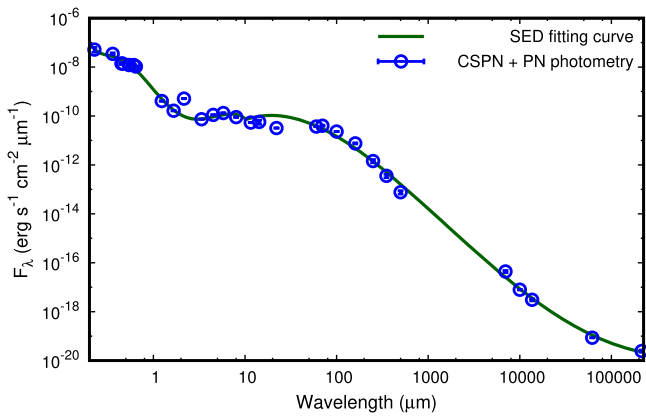


**Figure 9.** Empirical SED of the CSPN plus PN (blue circles; Table 1) with the polynomial fitting (green curve). See Figure 1 and Table 1 for the origins of the empirical data.

are expected to be present in the nebula along the equatorial and polar directions, respectively.

Based on the resemblance between the observed spatial distribution of the ionized gas and that of the other (molecules and dust) components (Figure 4; Zuckerman et al. 1990; Hiriart 2005; HerPlaNS1), the transition from the ionized region to the PDR must be happening quite rapidly over a small radial range. Hence, we start model calculations with a nebula that is ionization bounded at around  $R = 55''$ , which corresponds to the outer radius of the central ring structure of the nebula and also the intensity peak of  $H_2$  and CO emission (see Section 3.2.4). The use of the cylinder option is also corroborated by the density-bounded nature of the nebula expected in the polar directions of the nebula.

#### 4.2.8. Additional Heating Source of $H_2$

We introduce a high-density PDR wall beyond the ionization front in the model geometry (Figure 8) to explain the observed molecular emission. However, this causes significant underestimates of the observed  $H_2$  and high- $J$  CO line fluxes, as well as their column densities. This failure suggests the presence of an additional heating source in the PDR.

An obvious extra PDR heating source is the interstellar radiation field (ISRF). However, no meaningful heating of the PDR can be achieved by the ISRF in the present model for NGC 6781: only  $\lesssim 1\%$  of the observed  $H_2$  flux is reproduced by the nominal Galactic ISRF. Hence, it is unrealistic to expect to generate enough heating to reproduce *all* of the observed  $H_2$  flux by the ISRF alone unless it is unrealistically enhanced. Thus, it is reasonable to expect something other than the ISRF for a PDR heating source to explain the observed  $H_2$  fluxes. By the same token, the Galactic background cosmic ray cannot possibly work as a PDR heating source unless it is unrealistically enhanced.

*Soft X-rays.*—Another extra heating source is soft X-ray emission from a high-temperature CSPN as suggested by the presence of PNe in which X-rays were detected (e.g., Chu et al. 2001; Kastner et al. 2012; Montez et al. 2015). Soft X-rays (50 eV–10 keV) from a CSPN of  $T_{\text{eff}} > 100$  kK can strengthen  $H_2$  line emission, because such high-energy photons would penetrate into the PDR beyond the ionization front (Natta & Hollenbach 1998). Using data from the *Chandra X-ray Observatory*, Montez et al. (2015) examined the X-ray luminosities for a group of Galactic PNe including

NGC 6781. They found that no X-rays were detected from NGC 6781 in the 0.3–8.0 keV energy band, while a simple blackbody of  $T_{\text{eff}} \sim 120$ –130 kK at 0.46 kpc is sufficient for detectable X-ray fluxes in the 0.3–8.0 keV energy band (their Figure 14). Hence, the nondetection of X-ray emission in NGC 6781 is indicative of strong interstellar extinction or metal line blanketing, either of which can suppress the X-ray emission to below the detection limit.

We examine whether X-ray emission possible from the CSPN of NGC 6781 can result in a better fit to the observed  $H_2$  line fluxes under the following two scenarios: (1) if the X-ray luminosity ( $L_X$ ) of the CSPN were to power the entire observed mid-IR  $H_2$  luminosity ( $\sim 5.59 \times 10^{33}$  erg  $s^{-1}$  at  $D = 0.46$  kpc; Table 4), but were to be suppressed completely by the extinction, and (2) if the CSPN possessed an atmosphere of subsolar metallicity to circumvent metal line blanketing. The predicted  $H_2$  line fluxes with these X-ray emission enhancements would not reproduce the observed line fluxes even if we adopted (1) an extra blackbody emitting in the range of 0.27–10.4 keV with a luminosity of  $\sim 10^{33}$  erg  $s^{-1}$  at  $10^3$  kK or (2) an atmosphere of Galactic halo metallicity for the CSPN. Therefore, we conclude that extra soft X-ray would not possibly produce the observed  $H_2$  line fluxes in NGC 6781.

*Shock heating in the PDR.*—Yet another extra heating source is a mechanical heat input by shocks as suggested from the  $H_2$  excitation diagram analysis (Sections 3.2.2 and 3.2.3). This idea, previously used in a study of the C-rich PN NGC 7027 by Hasegawa et al. (2000), can work to excite  $H_2$  lines in regions far enough away from the CSPN. As Cloudy does not handle shocks, the desired extra heating by shocks is achieved by invoking the “temperature floor” option, which forces the predetermined value of the electron temperature  $T_e$  over a specific region (see Section 4.3). We iteratively search for the optimum floor temperature in the PDR ( $R \geq 58''$ ) between 800 and 1600 K. This temperature range is suggested by the  $H_2$  excitation temperatures derived from the excitation diagram analysis (Section 3.2.3).

While the use of a “temperature floor” helps to reproduce the observed warm  $H_2$  lines (except for 17.04  $\mu\text{m}$ ), as well as high- $J$  CO and OH lines,<sup>16</sup> the adaptation of the “temperature floor” also introduces negative side effects such as (1) suppression of molecular lines with lower excitation temperatures and (2) overestimation of atomic gas line fluxes such as far-IR [O I] and [C II] lines that have low-excitation energy at the upper levels. These side effects would make the mass fraction of the atomic and molecular gas with respect to the neutral (atomic + molecular) gas highly uncertain, primarily because the model would fail to account for the cold molecular component while introducing the corresponding amount of extra atomic gas (as the total amount of neutral gas was practically set by the input hydrogen density profile; Figure 8). However, the proper amount of the warm and cold molecular components, as well as the atomic gas component, can be recovered (Section 4.3.4).

### 4.3. The Best-fit Model

#### 4.3.1. Model Iteration

To find the best-fit model, we vary 13 parameters— $T_{\text{eff}}$ ,  $L_*$ , the inner radius of the shell ( $R_{\text{in}}$ ), elemental abundances ( $\epsilon(\text{He}/\text{N}/\text{O}/\text{Ne}/\text{Si}/\text{Cl}/\text{Ar})$ , except for  $\epsilon(\text{C})$ , which was fixed), dust

<sup>16</sup> Because  $\text{OH}^+$  is not available in Cloudy, we are unable to use the observed  $\text{OH}^+$  line fluxes.

and PAH mass fraction, and the floor temperature of the PDR—within a given range by using the *optimize* command available in Cloudy. We terminate iterative calculations when any one of the predicted flux densities,  $F_{\nu}(170\ \mu\text{m})$ ,  $F_{\nu}(250\ \mu\text{m})$ , or  $F_{\nu}(350\ \mu\text{m})$ , reaches the corresponding observed value. Practically, the terminating conditions would determine the maximum  $R_{\text{out}}$ , i.e., the thickness of the dense PDR beyond the inner ionized region, by setting the amount of far-IR continuum emission. The flux densities at 170, 250, 350  $\mu\text{m}$  are selected as constraints because there are no strong emission lines in these bands and they can be compared with measurements made in the PACS 160 and SPIRE 250 and 350  $\mu\text{m}$  bands. In this sense,  $R_{\text{out}}$  is not a free parameter.

The best-fit model is determined by the minimum  $\chi^2$  (16 for the best-fit model) calculated from the following 136 observational constraints: 37 broadband fluxes, 78 gas emission line fluxes relative to  $H\beta$  as well as  $I(H\beta)$ , 19 flux densities in mid-IR, far-IR, and radio wavelengths, and the ionization boundary radius ( $R_{\text{IB}}$ ). We define  $R_{\text{IB}}$  as the radial distance from the CSPN at which  $T_e$  drops below 4000 K; below such a temperature, no ionized gas emission lines except for [C II] and [S II] would be measurable.

In Table 6, we summarize the best-fit parameters. The SED of the best-fit model, in comparison with the observational data, is presented in Figure 10. Figure 11 is also provided to show the quality of the best-fit model with blow-ups of various wavelength ranges with major emission lines. In Table 15, we list the best-fit model versus observed quantities of gas emission line fluxes relative to  $H\beta$ , broadband fluxes relative to  $H\beta$ , and flux densities.

Here, we can retroactively check whether the empirical estimates and adaptation of certain quantities in determining the input model parameters are actually corroborated by the best-fit model. In Section 3.1.1, we used the empirical formulae to estimate the amount of RL contributions to [O III]  $\lambda 4363$ , [O II]  $\lambda 7320/30$ , and [N II]  $\lambda 5755$  lines in deriving  $T_e$ . The best-fit model yields  $I_{\text{R}}/I([\text{O III}] \lambda 4363) = 0.67\%$ ,  $I_{\text{R}}/I([\text{O II}] \lambda 7320/30) = 1.13\%$ , and  $I_{\text{R}}/I([\text{N II}] \lambda 5755) = 0.31\%$ , which are consistent with the empirical determinations adopted (0.73%, 2.19%, and 0.54%, respectively).

As for the ICFs used in determining the elemental abundances, we can compare the adopted ICFs based on I.P. and the ICFs calculated by the best-fit Cloudy model based on the ionization fraction of each element in the volume average in Table 7. While the values turn out to be consistent in general, discrepancies are found in Cl from the uncertain  $\text{Cl}^+$  fraction and in Si from the largely uncertain  $\epsilon(\text{Si})$  and ICF(I.P.). According to the best-fit model, the fraction of  $\text{Cl}^+$  to Cl is 0.38 and of  $\text{Si}^+$  to Si is 0.668.

As mentioned in the previous section (Section 4.2.8), the best-fit model is achieved by forcing the region of constant temperature at 1420 K in the PDR. This constant-temperature region is established from  $58''.06$  to  $61''$ , that is, the radial temperature drops precipitously from 2750 K at  $58''$  to 1420 K at  $58.06''$ , but is maintained at 1420 K from  $58''.06$  to  $61''$  to reproduce the observed molecular ( $\text{H}_2$ , CO, and OH) line fluxes. In this region, the relative proportion of molecular gas is maintained. So is the relative proportion of atomic gas.

In reality (of the presumed shocked  $\text{H}_2$  scenario), however, shocked molecular regions are highly localized, and hence the relative proportion of molecular gas would keep increasing radially while that of atomic gas would keep decreasing.

**Table 6**  
Characteristics of the Best-fit Cloudy Model of NGC 6781

Parameters of the CSPN	Values
$L_{\ast}/T_{\text{eff}}/\log g$	121 $L_{\odot}/120\ 870\ \text{K}/6.9\ \text{cm s}^{-2}$
$D$	0.46 kpc
Parameters of the Nebula	Values
$\epsilon(\text{X})$	He:11.02, C:8.56, N:8.10, O:8.64, Ne:8.00, Si: 6.25, S:6.82, Cl:5.01, Ar:6.22, Fe:6.20 Others: Karakas (2010)
Geometry (Figure 8)	“Cylinder” with height = $90''$ (0.201 pc) Inner radius ( $R_{\text{in}}$ ) = $0.52''$ (0.001 pc) Ionization boundary ( $R_{\text{IB}}$ ) = $55''$ (0.123 pc) Outer radius ( $R_{\text{out}}$ ) = $61''$ (0.135 pc)
Adopted $n_{\text{H}}$ (Figure 8)	Inner cavity ( $R < 54''$ ): $300\ \text{cm}^{-3}$ Barrel wall ( $54'' \leq R < 58''$ ): $960\ \text{cm}^{-3}$ PDR ( $58'' \leq R < 61''$ ): $10^4\ \text{cm}^{-3}$
Temperature $T_e$	Inner cavity ( $R < 54''$ ): 23 820–10 260 K Barrel wall ( $54'' \leq R < 58''$ ): 10 260–2 750 K PDR ( $58'' \leq R < 61''$ ): 2 750–1 420 K
Filling factor ( $f$ )	1.0
$\log_{10} I(H\beta)$	$-9.890\ \text{erg s}^{-1}\ \text{cm}^{-2}$ (de-reddened)
Temperature floor	1420 K
Mass	Ionized gas: $0.094 M_{\odot}$ Neutral (atomic + molecular) gas: $0.31 M_{\odot}^{\text{a}}$
Parameters of the Dust and PAHs	Values
Particle size	PAH (neutral & ionized): $0.0004\text{--}0.011\ \mu\text{m}$ , AC: $0.005\text{--}0.50\ \mu\text{m}$
Temperature	PAH (neutral): 71–515 K, PAH (ionized): 72–367 K, AC: 22–299 K
Mass	PAH (neutral): $3.30(-7)M_{\odot}$ PAH (ionized): $2.46(-6)M_{\odot}$ AC: $1.53(-3)M_{\odot}$
GDR	268

**Note.**

<sup>a</sup> We corrected the molecular gas mass of  $0.11 M_{\odot}$  and the atomic gas mass of  $0.20 M_{\odot}$ . See Section 4.3.4 and Table 10.

Therefore, with the presence of this constant-temperature PDR, the amount of the atomic gas component is bound to be overestimated in the PDR, i.e., the [C II] and [O I] line fluxes are overpredicted (by a factor of 3–9; Figure 11, Table 15).

While our Cloudy model extends as far out as  $R_{\text{out}} = 61''$ , the optical ISIS and far-IR *Herschel*/PACS observations do not detect these [C II] and [O I] lines with a sufficient signal level this far out in the PDR (i.e., the detection limit is reached at  $R \approx 55''$ ). If we stopped model calculation at  $R_{\text{IB}}$  of  $55''$ , we would obtain reasonable predictions of atomic line fluxes: for instance,  $I([\text{O I}] 63\ \mu\text{m}) = 25.07$  (33.18, observed),  $I([\text{O I}] 145\ \mu\text{m}) = 2.21$  (2.90, observed), and  $I([\text{C II}] 157\ \mu\text{m}) = 8.25$  (15.9, observed). However, of course, we would not be able to fit molecular lines at all (e.g.,  $I(\text{H}_2 9.67\ \mu\text{m}) = 8(-5)$  for the model versus 25.79 observed).

In the present work, we adopt the average [C II] and [O I] line fluxes measured in the entire PACS IFU field of view (over both of the “center” and “rim” positions; Figure 2), and the model-predicted [C II] and [O I] line fluxes are deemed overestimated as a result. However, we actually measure fluxes as high as  $I([\text{O I}] 63\ \mu\text{m}) = 103$ ,  $I([\text{O I}] 145\ \mu\text{m}) = 8.69$ , and  $I$



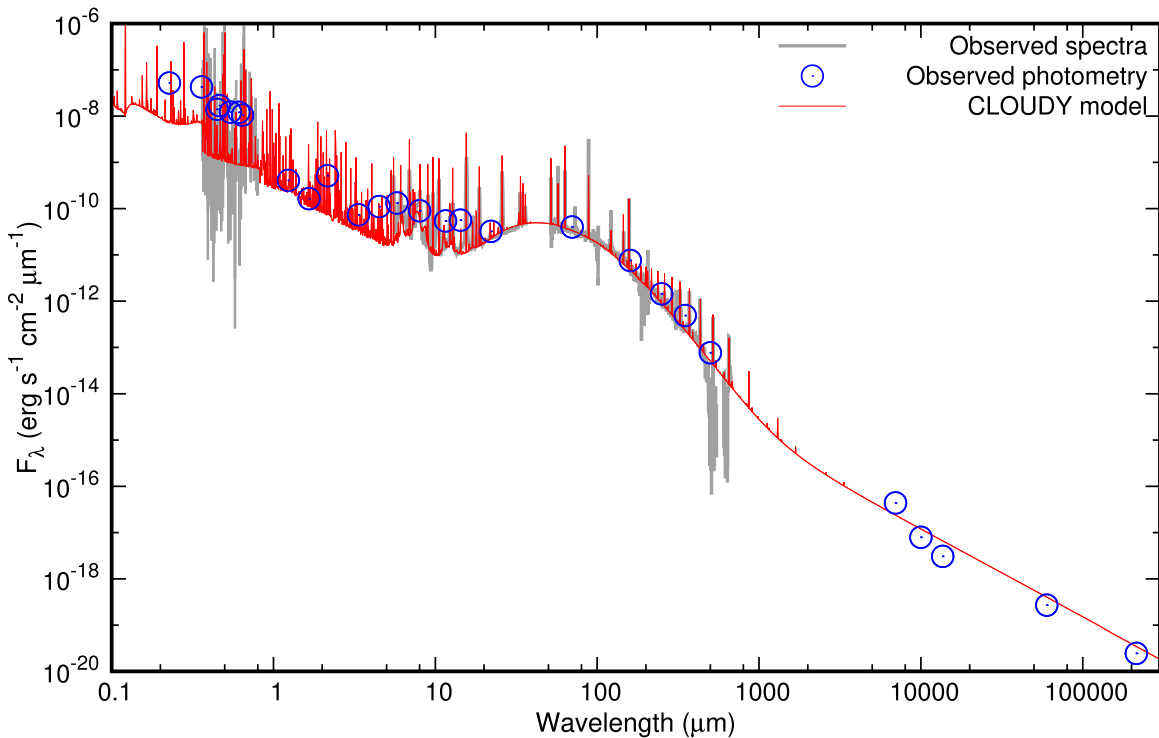


**Figure 10.** Full SED of the best-fit Cloudy model of NGC 6781 (red line;  $R = 300$ ), compared with the observational constraints (Table 15): photometry data (blue circles) and spectroscopy data (gray line).

$[\text{C II}] 157 \mu\text{m}) = 27.24$  in individual PACS spaxels over the barrel wall. Because there are no more data available to fit the model, especially the atomic component of the PDR, we have to leave these remaining discrepancies as issues to be resolved in the future when we obtain more sensitive data of the PDR and beyond. We will discuss the molecular component in detail later in Section 4.3.4.

#### 4.3.2. Amorphous Silicate Grain Model

To explore the possible O-rich nature of NGC 6781 (Section 3.1.4), we also construct the other “best-fit” model with amorphous silicate grains, adopting spherical grains of  $0.05\text{--}0.50 \mu\text{m}$  radius (Figure 13). Overall, the best-fit model with amorphous carbon grains fit the observed continuum much better than the best-fit model with amorphous silicates. To fit the observed dust continuum with amorphous silicate grains, we have to reduce the amount of small grains in order not to produce any recognizable  $10 \mu\text{m}$  silicate feature while achieving reasonable continuum fluxes in the far-IR. It is almost impossible to fit the dust continuum both in the mid-IR ( $10\text{--}40 \mu\text{m}$ ) and in the far-IR ( $>70 \mu\text{m}$ ) simultaneously with amorphous silicate grains because amorphous silicates emit continuum only weakly beyond  $70 \mu\text{m}$ . Therefore, we conclude that NGC 6781 was more likely C-rich in terms of the circumstellar dust composition.

#### 4.3.3. Evolutionary Status and Age of the Object

Figure 12 shows how the best-fit model compares with the adopted post-AGB evolutionary tracks of Vassiliadis & Wood (1994). In the same plot, the best-fit model of NGC 6720 by van Hoof et al. (2010) is also displayed to confirm the similarity between the two in terms of the evolutionary status. A comparison between the evolutionary tracks implies that the

progenitor of both NGC 6781 and NGC 6720 is a  $\sim 2.5 M_{\odot}$  star of  $Z = 0.02$  and that the post-AGB age (i.e., the time since the cessation of AGB mass loss) is  $\sim 9400$  yr for NGC 6781.

In addition, we plot in Figure 12 the evolutionary tracks of Miller Bertolami (2016, orange tracks of  $2.0$  and  $3.0 M_{\odot}$  stars). These newer tracks are computed to address the shorter-than-expected timescales for Galactic bulge PNe. Their models with  $Z = 0.01$  would take  $\sim 3000$ ,  $\sim 2700$ , and  $\sim 8000$  yr to reach  $T_{\text{eff}} = 120,870$  K for  $2.0$ ,  $2.5$ , and  $3.0 M_{\odot}$  stars, respectively, while models with  $Z = 0.02$  would take  $\sim 2600$  to  $\sim 12,000$  yr to reach the same temperature for the  $2.0$  and  $3.0 M_{\odot}$  models of  $Z = 0.02$  for the same mass stars, respectively (no model track is given for  $2.5 M_{\odot}$ ). Thus, the post-AGB age of a  $2.5 M_{\odot}$  progenitor with  $Z = 0.02$  would be  $\sim 3000$  yr.

Following the method suggested by O’Dell et al. (2007), the empirical dynamical age of a PN can be approximated simply by

$$t_{\text{dyn}} \simeq R / \frac{V_{\text{exp}}(\text{today}) + V_{\text{exp}}(\text{AGB})}{2}, \quad (8)$$

where  $V_{\text{exp}}(\text{today})$  is the present-day shell expansion velocity and  $V_{\text{exp}}(\text{AGB})$  is the shell expansion velocity at the beginning of the AGB phase. In this formulation, the shell expansion velocity is taken to be the rough “average” between the AGB wind velocity and the fast wind velocity. Assuming  $V_{\text{exp}}(\text{AGB}) = 16\text{--}22 \text{ km s}^{-1}$  (corresponding to the observed expansion velocity of the cold CO gas; Bachiller et al. 1993; Bergstedt 2015),  $V_{\text{exp}}(\text{today}) = 12 \text{ km s}^{-1}$  (from the  $[\text{N II}]$  line; Arias & Rosado 2002), and  $R_{\text{IB}} = 55''$  (the ionization front radius), the dynamical age would be roughly  $7100\text{--}8600$  yr.

Gesicki et al. (2016) suggested  $t_{\text{dyn}} \simeq (5/7) \times (R_{\text{IB}}/V_{\text{exp}})$  based on hydrodynamical model calculations. Adopting  $V_{\text{exp}} = 12 \text{ km s}^{-1}$  as above, the hydrodynamical age would be  $7140$  yr. Thus, the theoretical post-AGB age inferred from

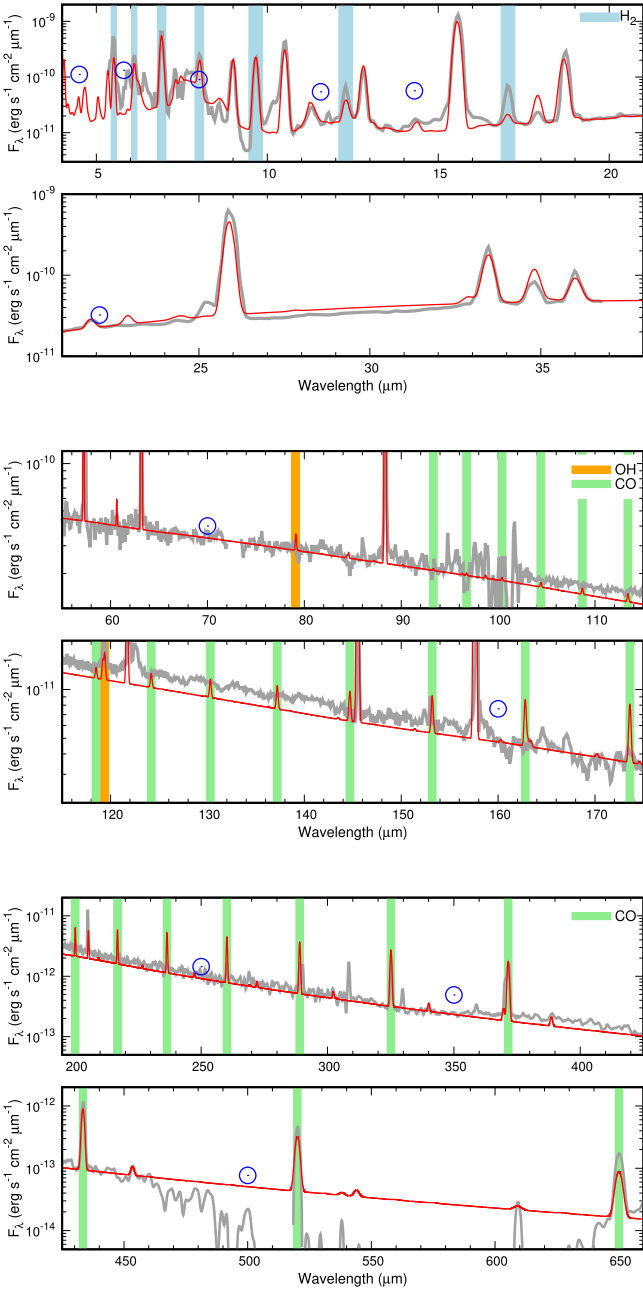


**Figure 11.** Comparison between the SED of the best-fit Cloudy model (red line, with undetectable atomic and molecular lines [ $<10^{-2}\%$  of the  $H\beta$  flux] removed;  $R = 100$  in the top two frames and  $R = 480$  in the other frames, corresponding to the resolution of the instrument in the respective bands) and the observational data (spectra in gray line and photometry in blue circles) in IR regions (top: *Spitzer*/IRS; middle: *Herschel*/PACS; bottom: *Herschel*/SPIRE). The positions of molecular line emission are highlighted: rotational  $H_2$  lines (light blue), OH (yellow), and  $^{12}CO$  (light green). See Table 15.

**Table 7**

Comparison between the ICFs Estimated Based on I.P. (Adopted for Elemental Abundance Derivations in Section 3.1.3) and Predicted by the Cloudy Model

X	ICF(I.P.)	ICF(Model)	X	ICF(I.P.)	ICF(Model)
He	1.00	1.00	Si	$6.80 \pm 1.75$	1.50
C	$2.03 \pm 0.32$	1.89	S	1.00	1.01
N	$1.05 \pm 0.06$	1.08	Cl	$1.17 \pm 0.09$	1.66
O	1.00	1.00	Ar	$1.17 \pm 0.09$	1.15
Ne	1.00	1.03	...	...	...

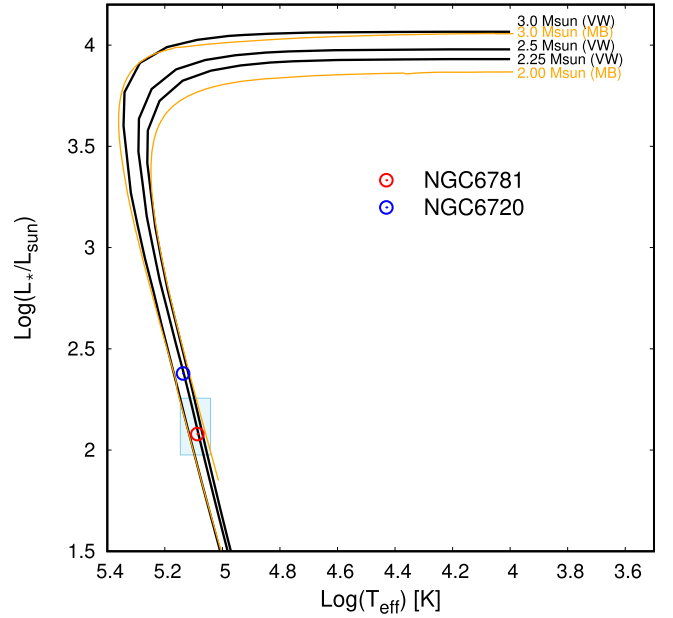


**Figure 12.** Comparison between the best-fit Cloudy model of NGC 6781 (red circle;  $L_*$  and  $T_{\text{eff}}$  of the CSPN) and the post-AGB evolutionary tracks (black lines) of 2.25, 2.5, and  $3.0 M_{\odot}$  initial-mass stars (Vassiliadis & Wood 1994, also shown in Figure 7). We also plot the post-AGB evolutionary tracks (orange lines) of 2.0 and  $3.0 M_{\odot}$  stars with  $Z = 0.02$  by Miller Bertolami (2016). The light-blue box indicates the empirical  $L_* - T_{\text{eff}}$  parameter range as discussed in Section 3.4.1. The best-fit Cloudy model of NGC 6720 (blue circle;  $L_*$  and  $T_{\text{eff}}$  of the CSPN; van Hoof et al. 2010) is also plotted for comparison.

the Cloudy best-fit model and the evolutionary tracks by Vassiliadis & Wood (1994) is comparable to these (hydro) dynamical age estimates. Meanwhile, the much shorter post-AGB evolutionary time suggested by the evolutionary tracks by Miller Bertolami (2016) is more problematic to reconcile because the observed PN size would not be consistent with the observed expansion velocity, provided that the best-fit distance is 0.46 kpc (Section 3.4.1)

#### 4.3.4. Molecular Gas Components

Here, we look into the molecular component of the best-fit model, especially into the PDR. We begin by comparing the model-predicted and empirically derived molecular column densities of  $H_2$ , CO, and  $OH^+$  (Table 8). The model-predicted results are derived by taking into account all of the gas components (i.e., molecular, atomic, and ionized), self-consistently allowing molecular formation processes (e.g., formation on dust grain surfaces and in the gas phase, and so on).

As discussed above (Section 4.2.8), we introduced the warm-temperature component in the PDR as a necessary extra heating source to reproduce the observed  $H_2$ , CO, and OH lines. However, the achieved general agreement between the model and empirical column densities (Table 8) and line intensities (Figure 11; Table 15) permit qualitative characterization of the PDR in NGC 6781.

The best-fit floor temperature of 1420 K is consistent with the empirical estimates of  $T(H_2) = 1279 \pm 109$  K and  $1161 \pm 72$  K by the single- and two-temperature excitation diagram fitting, respectively (Section 3.2.3). This suggests that  $H_2$  is most likely in LTE and its kinetic temperature is about

**Table 8**

Comparison between the Best-fit Model-predicted and Empirically Derived Molecular Column Densities

Molecule	$\log_{10} N(\text{Model})$ ( $\text{cm}^{-2}$ )	$\log_{10} N(\text{Obs})$ ( $\text{cm}^{-2}$ )	Obs. References
H <sub>2</sub>	18.18	18.36 ± 0.09	This work
CO	15.13	14.70–15.08	HerPlaNS1
OH <sup>+</sup>	13.00	10.54	Aleman et al. (2014)

1420 K. With this kinetic temperature, CO and OH lines are fit reasonably well. If we are to fit just the high- $J$  CO lines, the best-fit floor temperature for CO would be 680 K. Either way (fitting with or without H<sub>2</sub>), the (kinetic) temperature of CO gas would still be very much higher than an excitation temperature of  $\sim 60$  K (HerPlaNS1). This discrepancy can be mitigated if CO is assumed to be in non-LTE. Given the difference in the number density between H<sub>2</sub> and CO, CO could yet be being thermalized while H<sub>2</sub> already is.

Thus, we examine the excitation temperature of each CO line using the 1D non-LTE radiative transfer code RADEX (van der Tak et al. 2007). In RADEX calculations, we adopt the kinetic temperature of 1420 K, a constant  $n(\text{H}) = 10^4 \text{ cm}^{-3}$ , and  $\log_{10} N(\text{CO}) = 15.13 \text{ cm}^{-2}$  as in the Cloudy model. The RADEX results (Table 9) suggest that the excitation temperature of high- $J$  CO lines is 70–80 K on average, supporting the non-LTE condition for CO. We therefore conclude that the best-fit Cloudy model properly accounts for the presence of the warm component.

The best-fit model predicts the amount of molecular gas in the PDR to be  $4.15(-3) M_{\odot}$ , which accounts only for the warm H<sub>2</sub> component (i.e., there are no other “cold” molecular components in the best-fit model). Meanwhile, this model prediction is actually consistent with the empirical estimate of  $2.5(-3) M_{\odot}$  for the warm component (Section 3.2.4). However, the presence of the cold molecular component is very much expected based on the excitation diagram analysis (Section 3.2.3), as well as the non-LTE analysis we just saw above. In reality, there is probably a temperature gradient in the PDR along the polar direction, which empirically manifests itself as the multitemperature fit of the excitation diagram analysis and the non-LTE nature of the CO distribution.

Now, given that the best-fit model already properly accounts for the amount of ionized and neutral (atomic + molecular) gas, the cold molecular component that should exist must have been treated as part of the atomic gas component, as mentioned earlier (Section 4.2.8). Here, by adopting the ratio of the empirically determined cold H<sub>2</sub> mass to warm H<sub>2</sub> mass ( $24.8 = 6.2(-2) M_{\odot} / 2.5(-3) M_{\odot}$ ; Section 3.2.4), we can infer the amount of the cold molecular component to be expected in the best-fit model,  $1.12(-1) M_{\odot}$  ( $= 4.15(-3) M_{\odot} \times 24.8$ ). From this, we conclude that the modified best-fit model estimates of the mass of the cold molecular, warm molecular, and atomic gas components are  $1.12(-1) M_{\odot}$ ,  $4.15(-3) M_{\odot}$ , and  $1.99(-1) M_{\odot}$  ( $= 3.11(-1) M_{\odot} - 1.12(-1) M_{\odot}$ ), respectively (see also Table 10).

We end the discussion on the molecular component in NGC 6781 by pointing out two lesser issues to be resolved that are beyond the scope of the present work. One is obviously the presence of the extra heating source. We incorporated the warm-temperature component in the model PDR assuming that

shock interactions between the slower AGB wind and faster PN wind would provide sufficient extra heating to the PDR at the required level. Nonetheless, this extra heating source should be identified and self-consistently incorporated in the future. The other issue is the discrepancy in the OH<sup>+</sup> column densities. This may well be due to a relatively more uncertain chemical network around OH<sup>+</sup> and/or outdated reaction parameters in the astrochemistry network installed in Cloudy. However, the cause of the OH<sup>+</sup> column density discrepancy is also unclear at this moment.

#### 4.3.5. Comparison between Theoretical and Observed Gas Masses

It is of interest to compare the amount of mass ejected during the AGB phase that is empirically accounted for with the adopted panchromatic data set (observational detection + model fitting via the present analyses) to our previous estimates based on an incomplete data set and to a theoretical prediction. As summarized in Table 10, the total gas mass empirically accounted for in NGC 6781 was  $0.41 M_{\odot}$ , comprising  $0.09 M_{\odot}$  of ionized gas,  $0.20 M_{\odot}$  of atomic gas, and  $0.11 M_{\odot}$  of molecular gas. These values are based on the adopted volume filling factor  $f$  of unity (Section 3.4.1).

Previously, using almost exclusively far-IR line data and under the assumption of  $D = 0.95$  kpc, the total gas mass was estimated to be  $0.86 M_{\odot}$ , which consisted of  $0.54 M_{\odot}$  of ionized gas (only H<sup>+</sup>, He<sup>+</sup>, and He<sup>2+</sup>),  $0.12 M_{\odot}$  of atomic gas, and  $0.20 M_{\odot}$  of molecular gas (only H<sub>2</sub> based on  $N(\text{H}_2)$  calculated from the excitation diagram), while adopting  $f = 0.5$  (HerPlaNS1). With the updated distance of  $D = 0.46$  kpc and  $f = 1$ , these previous estimates correspond to the total gas mass of  $0.40 M_{\odot}$ . While the total mass turns out to be consistent with the present result, the relative proportion of the individual gas components in the previous result is very different. This is, of course, because of the fact that we have to scale the relative proportion to fill gaps of the absence of sufficiently constraining observational data.

According to Karakas & Lattanzio (2007) and Karakas (2010), a  $2.5 M_{\odot}$  initial-mass star with  $Z = 0.02$  would experience 25 AGB thermal pulse (TP) episodes while ejecting the total mass of  $\sim 1.25 M_{\odot}$ . However, the predicted amount of the mass-loss ejecta would remain small ( $< 0.01 M_{\odot}$ ) until the 22nd TP episode. Over the last three TP episodes, the amount of the ejecta would increase precipitously, reaching  $\simeq 0.70 M_{\odot}$  during the last TP episode. Hence, our best-fit model accounts for roughly 60% of the amount of mass theoretically predicted to have been ejected during the last TP episode.

Meanwhile, the total gas mass within the ionization bound,  $R_{\text{IB}} = 55''$ , is  $0.12 M_{\odot}$  (consisting of  $0.09 M_{\odot}$  and  $0.03 M_{\odot}$  ionized and atomic gas, respectively), accounting for about 23% of the total gas mass. This proportion is consistent with a previous theoretical prediction made by Villaver et al. (2002), in which the evolution of the ejecta was modeled based on the stellar evolution tracks by Vassiliadis & Wood (1993). They concluded that the bright ionized shell would contain about  $0.5 M_{\odot}$  of gas for a  $2.5 M_{\odot}$  initial mass (their Figure 25), which roughly translates to 25% of the total ejecta mass.

Comparisons among these quantities indicate that the bulk of the nebular mass is found to be in the PDR of the nebula beyond  $R_{\text{IB}}$  in the form of neutral (atomic/molecular) gas. This finding is quite intriguing given the fact that PNe are generally known as the hallmark of the presence of ionized gas as H<sup>+</sup> regions. The present work also demonstrates that PNe would



**Table 9**  
RADEX Non-LTE CO Model Results, and Comparison with the Observed Line Intensities

$J$	( $\mu\text{m}$ )	$T_{\text{ex}}$ (RADEX) (K)	Intensity (RADEX) ( $\text{erg s}^{-1} \text{cm}^{-2}$ $\text{sr}^{-1}$ )	Intensity (Obs) ( $\text{erg s}^{-1} \text{cm}^{-2} \text{sr}^{-1}$ )
4–3	650.3	209	3.51(–7)	3.73(–7) $\pm$ 6.35(–8)
5–4	520.2	85	7.71(–7)	7.67(–7) $\pm$ 2.03(–8)
6–5	433.6	70	1.19(–6)	1.17(–6) $\pm$ 1.51(–7)
7–6	371.7	70	1.47(–6)	1.99(–6) $\pm$ 2.49(–7)
8–7	325.2	74	1.58(–6)	9.71(–7) $\pm$ 1.38(–8)
9–8	289.1	82	1.55(–6)	1.08(–6) $\pm$ 2.91(–7)

provide a unique window of opportunities to investigate the mass-loss history of the progenitor star, because PNe should allow (1) access to a significant fraction of the AGB mass-loss ejecta when observed with sufficiently sensitive instruments (as opposed to AGB stars themselves) and (2) spatially resolved investigations more into the past (i.e., regions of larger radii) due to much larger energy input by the central star to illuminate the PDR of the nebula (as opposed to proto-PNe).

#### 4.3.6. The Far-IR/Cold Dust Component of the Nebula

The best-fit model yields the dust mass ( $m_{\text{dust}}$ ) of 1.53(–3)  $M_{\odot}$ , while the empirically determined value obtained by fitting far-IR broadband images (HerPlaNS1), scaled to the present distance estimate of  $D = 0.46$  kpc, is 9.4(–4)  $M_{\odot}$ . In both estimates, dust grain properties are the same (i.e., AC grains). This discrepancy is expected because the previous empirical estimate considered only the cold dust component detected in the far-IR ( $\sim 20$ –40 K; HerPlaNS1), missing the higher-temperature component emitting mainly in the shorter wavelength (e.g., mid-IR). The present best-fit model includes the entire (warm + cold) dust component ( $\sim 22$ –299 K).

To assess the consistency between the best-fit model and the empirical measurements, we estimate the mass of the cold/far-IR dust component in the best-fit model. Similar to the discussion in the previous section, we consider the cold dust component existing in the PDR beyond the IB, over which the model-predicted dust temperature would be 23–38 K. In the best-fit model, the dust mass beyond  $R_{\text{IB}}$  is 1.06(–3)  $M_{\odot}$ , which is consistent with the empirical cold dust mass of 9.4(–4)  $M_{\odot}$ .

The circumstellar dust mass is typically estimated via SED fitting of the thermal dust excess in the near- and mid-IR wavelengths. However, the present study reveals that there is a larger amount of cold dust (of 1.06(–3)  $M_{\odot}$ ) than warm dust (of 4.61(–4)  $M_{\odot}$ ) around NGC 6781. This finding suggests that the far-IR/cold dust component could take up a significant portion of the circumstellar dust in PNe ( $\sim 69\%$  for the case of NGC 6781), and hence far-IR fluxes must always be incorporated in studying PNe, especially when considering the energetics in the whole volume of the nebula (especially the PDR and beyond).

#### 4.3.7. Gas-to-dust Mass Ratio

In Cloudy model calculations, the presence of dust is scaled with the hydrogen density profile by the gas-to-dust mass ratio (GDR). The dust radiative transfer is done at each radial bin taking into account all the radiation available locally for dust

**Table 10**  
Comparison of Each of the Mass Components between This Work and the HerPlaNS1 Results

Parameters	This Work	HerPlaNS1	HerPlaNS1 (Scaled)
$D$ (kpc)	0.46	0.95	0.46
Filling factor	1.0	0.5	1.0
Total gas ( $M_{\odot}$ )	0.41	0.86	0.40
Ionized gas ( $M_{\odot}$ )	0.09	0.54	0.25
Atomic gas ( $M_{\odot}$ )	0.20	0.12	0.05
Total molecular gas ( $M_{\odot}$ )	0.11	0.20	0.09
Warm molecular gas ( $M_{\odot}$ )	4.15(–3)	...	...
Cold molecular gas ( $M_{\odot}$ ) <sup>a</sup>	1.12(–1)	...	...
Total dust mass ( $M_{\odot}$ )	1.53(–3)	...	...
Dust mass beyond $R_{\text{IB}}$ ( $M_{\odot}$ )	1.06(–3)	4.0(–3) <sup>b</sup>	9.4(–4) <sup>b</sup>
GDR	268	335 (median)	335 (median)

#### Notes.

<sup>a</sup> The model-predicted cold molecular mass was scaled from the model-predicted warm molecular mass in this work. In HerPlaNS1, the molecular component was not subdivided by temperature.

<sup>b</sup> The empirical dust mass estimate was for the cold dust of 20–40 K.

heating (i.e., radiation from the ambient gas as well as from the CSPN). However, there is no mechanism to produce/destroy dust grains in the code. The best-fit model yields the “mean” GDR of 268 over the entire volume. The derived GDR is comparable to the average GDR of  $386 \pm 90$  among 18 C-rich evolved stars (Knapp 1985) based on the direct comparison between the gas component (via CO  $J = 1 - 0$  observations in the radio, i.e., the cold gas component) and the dust component (via SED fitting of IR excess in the  $N$  band, i.e., the warm dust component). From our discussion in the previous section, it is likely that the Knapp work may have missed the cold dust component and hence their GDR may have been overestimated.

In our previous empirical estimate (HerPlaNS1), the GDR distribution in NGC 6781 shows a 10-fold decrease of the GDR from around 500 near the inner radius of the barrel wall to around 50 beyond the IB into the PDR with a median of 335. Caution needs to be exercised to compare these numbers because the empirical GDR distribution is susceptible to the projection effect (i.e., the gas and dust components being ratioed may not be present at the same location along the line of sight). Nevertheless, the median value is certainly consistent with the modeling results.

#### 4.3.8. 3D Effects on the Dusty Photoionization Models

Gesicki et al. (2016) reported that 3D photoionization models could reproduce the observed emission line fluxes with ionized gas mass that is several times less than 1D models may suggest. This is because in 3D models there is usually a greater amount of “surfaces” at which ionization can happen. In 1D models, radiation would always have to be attenuated before penetrating into the next/outer radial layer of the nebula. However, in 3D models, attenuation may not even occur along some lines of sight (e.g., along the polar direction vs. equatorial directions in the case of a bipolar nebula), providing means to ionize the outer parts of the nebula to a greater extent. Indeed, we already saw some indication of the 3D effects especially in the PDR based on the multitemperature fit of the excitation diagram analysis and the non-LTE nature of the CO

distribution, suggesting a temperature gradient along the polar direction of the nebula.

While 3D photoionization codes are available, we adopt the 1D Cloudy code because at this point no 3D photoionization codes would satisfactorily incorporate lower-temperature components (i.e., the dusty PDR) to be fit with the broad array of the adopted constraining observational data. For the case of NGC 6781 in particular, this 1D/3D issue implies that there could be a distribution of ionized gas extending along the polar directions (i.e., the regions of the polar caps and beyond), which would alter the overall proportion of the ionized gas in terms of the total mass of the nebula. However, these 3D effects on the ionized gas mass are considered to be minor in the present work. This is because model parameters that are critical in determining line fluxes and hence masses, such as the hydrogen density profile  $n_{\text{H}}(R)$ ,  $D$ ,  $L_*$ ,  $T_{\text{eff}}$ , nebular elemental abundances, and spatial distributions of various gas/dust components, were fixed to empirically derived values based on the spatially resolved data and not treated as free parameters, which is often the case in typical 1D models based on spatially unresolved data.

## 5. Conclusions

We have investigated the physical conditions and evolution of a bipolar PN NGC 6781 by (1) collecting the most comprehensive panchromatic data set for the object assembled sourced from various data archives covering from UV to radio, including our own *Herschel* data (Figure 1, Tables 11 and 12), and (2) performing dusty photoionization pseudo-2D model SED/line fitting with the Cloudy code using this panchromatic data set, which yielded 136 constraints. The primary aim of the investigation was therefore to generate the best-fit model that satisfies *all* of the adopted panchromatic data self-consistently.

Using nebular lines detected in the optical, mid-IR, and far-IR, we have performed detailed plasma diagnostics and derived  $n_e$  and  $T_e$  for nine diagnostic lines based on 15 different line ratios computed from 28 individual line fluxes (Figure 3, Tables 2 and 13), ionic abundances for 19 species (Table 14), and elemental abundances for 9 species (Table 3).

By comparing the empirically derived elemental abundances (Table 3) with the theoretically predicted abundances of the AGB nucleosynthesis models (Karakas 2010), the progenitor of NGC 6781 has been determined as a 2.25–3.0  $M_{\odot}$  initial-mass star of  $Z \simeq 0.02$ . By fitting the CSPN luminosity (Figure 6) as a function of the distance ( $D$ ) and effective temperature ( $T_{\text{eff}}$ ) with the post-AGB evolutionary tracks of 2.25–3.0  $M_{\odot}$  initial-mass stars (Vassiliadis & Wood 1994), we have derived a best-fit  $D$  of 0.46 kpc and  $L_*$  of 104–196  $L_{\odot}$  (Figure 7).

We have also performed the excitation diagram analysis to probe the physical conditions of the  $\text{H}_2$ -emitting PDR of the nebula. The excitation diagram for the observed  $\text{H}_2$  lines can be fit reasonably with a single- and double-temperature model at around 1300 K and 1200 K/240 K, respectively (Table 4, Figure 5). Comparisons with theoretical shock models by Flower & Pineau (2010) indicated that  $\text{H}_2$  could be excited by shocks caused by interactions between the remnant AGB circumstellar envelope and the fast wind emanating from the CSPN.

The results of our analyses of the observational data suggest that the apparent ring shape of NGC 6781 was best represented by a pole-on spherical cylinder structure (of 54'' inner radius and the ‘‘barrel’’ height of 90''), with a physically thin (of 4''

thickness) but dense ( $n_{\text{H}} = 960 \text{ cm}^{-3}$ ) wall surrounding a tenuous ionized gas ( $n_{\text{H}} = 300 \text{ cm}^{-3}$ ), all of which is surrounded by an even denser PDR ( $n_{\text{H}} = 10^4 \text{ cm}^{-3}$ ; Figure 8).

Armed with the empirically established CSPN characteristics and input model of the nebula, plus the most comprehensive panchromatic observational constraints ever compiled (37 broadband fluxes from UV to mid-IR, 19 flux densities from mid-IR to radio, 78 emission lines in four spectral ranges, and 8 elemental abundances, totaling 142 constraints; Tables 15 and 3), we have arrived at the best-fit photoionization model of NGC 6781 using the Cloudy code (Ferland et al. 2013) through iterative model fitting (Table 6, Figures 10–12).

The best-fit model indicates that the circumstellar nebula of NGC 6781 is illuminated by the CSPN of  $L_* = 121 L_{\odot}$  and  $T_{\text{eff}} = 121 \text{ kK}$  so that the ionization front is settled at  $R_{\text{IB}} = 55''$  (i.e., the nebula is ionization bounded along the equatorial direction but density bounded along the polar directions), with the outer radius of the PDR at 61''. To explain the observed  $\text{H}_2$  and CO line fluxes, the PDR would have to possess an extra heating source to keep the PDR temperature at about 1400 K. However, there must also be a component of cold molecules in the PDR, suggested by the excitation diagram analysis of  $\text{H}_2$  and CO and by non-LTE radiative transfer calculations of CO, which could not be simultaneously modeled in the present study because of a lack of observational data that probe/constrain the even colder part of the PDR. It is likely that a temperature gradient in the PDR along the polar direction contributes to the multitemperature characteristic of the PDR that was not fully constrained by the present pseudo-2D model.

This best-fit model can account for about 60% of the theoretically predicted gas mass of  $\sim 0.70 M_{\odot}$  (Table 10) ejected during the last AGB thermal pulse episode of a 2.5  $M_{\odot}$  initial-mass star of  $Z = 0.02$  (Karakas & Lattanzio 2007; Karakas 2010), of which only 20% of the total mass appears to be contained within the ionized region of the nebula. This finding emphasizes that while PNe are known as the hallmark of ionized gas in  $\text{H}^+$  regions, the colder dusty PDR that surrounds the ionized gas carries greater significance in terms of the progenitor’s mass-loss history and cannot be neglected to account for the full energetics of the nebula. Nonetheless, the present work has demonstrated that PNe can indeed serve as (1) empirical constraints for stellar evolutionary models, because empirically derived CSPN and nebula parameters can now comprehensively confront theoretical predictions (and the present AGB models are shown to be correct in general), and (2) important probes of mass recycling and chemical evolution in galaxies because PNe would permit one of the most thorough mass accountings of the mass-loss ejecta in the circumstellar environments.

Our present investigation has also demonstrated that detailed dusty photoionization PN models can explain a wide variety of observational data self-consistently and that the PDR is critically important to characterize PNe comprehensively. However, our work has also revealed that there is still a considerable lack of observational data to constrain the input parameters, especially those that probe the PDR (i.e., the coldest realm of PNe) and the X-ray emission properties of the CSPN and highly ionized gas in its vicinity (i.e., the hottest realm of PNe). Moreover, ideally 3D models would have to be used. In the future, critical issues to be investigated in PNe will be (1) far-IR and submillimeter spatially resolved spectroscopy

of the cold molecular component with ALMA, EVLA, and SKA, as well as *SPICA*; (2) mid-IR spatially resolved spectroscopy of the warm molecular component with *JWST*; (3) optical spatially resolved spectroscopy of the atomic gas component; and (4) X-ray/far-UV observations to better characterize the CSPN and possible accompanying extra high-energy sources.

This work is partly based on observations made with the *Herschel* Space Observatory, a European Space Agency (ESA) Cornerstone Mission with significant participation by National Aeronautics and Space Administration (NASA), and the *Spitzer Space Telescope*, obtained from the NASA/IPAC Infrared Science Archive, both of which are operated by the Jet Propulsion Laboratory (JPL), California Institute of Technology (Caltech), under a contract with NASA, as well as the *Infrared Space Observatory (ISO)*, an ESA project with instruments funded by ESA Member States and with the participation of the Institute of Space and Aeronautical Science/Japan Aerospace exploration Agency (ISAS/JAXA) and NASA.

Some of the data presented in this paper were obtained from the *Wide-field Infrared Survey Explorer*, which is a joint project of the University of California, Los Angeles, and JPL/Caltech, funded by NASA; the European Southern Observatory Science Archive Facility; the Isaac Newton Group Archive, which is maintained as part of the CASU Astronomical Data Centre at the Institute of Astronomy, Cambridge, UK; and the Mikulski Archive for Space Telescopes (MAST) at the Space Telescope Science Institute (STScI), which is operated by the Association of Universities for Research in Astronomy, Inc., under NASA contract NAS5-26555. Support for MAST for *GALEX* data is provided by the NASA Office of Space Science via grant NNX09AF08G and by other grants and contracts. When some of the data reported here were acquired, UKIRT was operated by the Joint Astronomy Centre on behalf of the Science and Technology Facilities Council of the UK. A portion of this work was based on the use of the ASIAA clustering computing system.

We are grateful to the anonymous referee for a careful reading and valuable suggestions. M.O. was supported by the research funds 104-2811-M-001-138 and 104-2112-M-001-041-MY3 from the Ministry of Science and Technology (MOST), R.O.C. M.O. sincerely expresses his thanks to Drs. Naomi Hirano and Tatsuhiro Hasegawa for fruitful discussion on molecular gas excitation. T.U. was partially supported by an award to the original *Herschel* observing program (OT1\_tueta\_2) under Research Support Agreement (RSA) 1428128 issued through JPL/Caltech, and by NASA under grant NNX15AF24G issued through the Science Mission Directorate. P.A.M.v.H. was funded by the Belgian Science Policy Office under contract no. BR/154/PI/MOLPLAN. I.A. acknowledges the support of CNPq, Conselho Nacional de Desenvolvimento Científico e Tecnológico—Brazil, process no. 157806/2015-4. A.A.Z. was supported by the UK Science and Technology Facility Council, through grant ST/L000768/1. Y.-H.C. was supported by the research fund 104-2112-M-001-044-MY3 from the MOST. E.V. acknowledges support from Spanish Ministerio de Economía y Competitividad under grant AYA2014-55840-P. M.L.L.-F. was supported by CNPq, Conselho Nacional de Desenvolvimento Científico e Tecnológico—Brazil, process no. 248503/2013-8.

*Facilities:* *Herschel*, *Spitzer*, *WISE*, *ISO*, *HST*, *GALEX*, ING/INT 2.5-m, ING/WHT 4.2-m, ESO/NTT 3.6-m, UKIRT 3.8-m.

*Software:* Cloudy (v C13.03; Ferland et al. 2013), IRAF (v.2.16), SMART (v.8.2.9; Higdon et al. 2004), IRSCLEAN (v.2.1.1; Ingalls 2011), Multidrizzle (Koekemoer et al. 2003).

## Appendix A Photometry Data and Measurements

### A.1. INT 2.5 m/WFC Photometry

We downloaded raw broadband imaging data at RGO *U*, Sloan *g*, and Sloan *r* and narrowband imaging data at IPHAS H $\alpha$  ( $\lambda_c = 6568.2 \text{ \AA}$  with the 93.97  $\text{\AA}$  equivalent width), taken with the Wide Field Camera (WFC) mounted on the 2.5 m Isaac Newton Telescope (INT) at the Roque de Los Muchachos Observatory, La Palma, Spain, from the Cambridge Astronomical Survey Unit (CASU) Astronomical Data Centre.

We reduced the downloaded raw data using IRAF following the standard procedure (i.e., bias subtraction, flat-fielding, bad-pixel masking, cosmic-ray removal, detector distortion correction, and sky subtraction) and performed point-spread function (PSF) fitting and aperture photometry using the IRAF `noao.digiphot` package. The gain and readout noise of the detector, determined from the IRAF task `findgain`, were  $0.65 \text{ e}^- \text{ ADU}^{-1}$  and  $1.48 \text{ e}^-$ , respectively.

Photometry was performed for the CSPN and two standard stars, SA110–246 and BD +28°4211 ( $m_u = 14.521$ ,  $m_g = 10.277$ ,  $m_r = 13.103$  and  $m_u = 9.977$ ,  $m_g = 10.277$ ,  $m_r = 14.440$ , respectively, in the SDSS system; Ahn et al. 2012), of which the standard stars were used to do flux calibration and PSF fitting. Then, we removed field stars in the vicinity of NGC 6781 and carried out photometry of the entire nebula (CSPN plus PN) using the residual images. In the end, the respective instrumental magnitudes of  $m_U$ ,  $m_g$ , and  $m_r$  were converted into the SDSS magnitudes of  $u$ ,  $g$ , and  $r$  with the following formulae:

$$m_u = -26.878 + r + 2.844 \sec(z_U) + 10.924(u - g), \quad (9)$$

$$m_g = -27.724 + r + 2.573 \sec(z_g) + 0.816(g - r), \quad (10)$$

$$m_r = -26.794 + r + 1.534 \sec(z_r) + 0.653(g - r), \quad (11)$$

where  $z_{\text{band}}$  stands for the airmass at the time of observations.

To obtain the flux density in the IPHAS H $\alpha$  band, we made measurements in the count rates (i.e.,  $\text{e}^-$  per second), while the measurement procedure itself was the same as the other broadbands. The count rate to flux density conversion factor was calculated by (1) measuring the count rate of the standard star BD +17°4708 in the IPHAS H $\alpha$  image and (2) computing the flux density per count rate in this band using the spectrum of BD +17°4708 from the *HST* CALSPEC Calibration Database,<sup>17</sup> taking into account the filter transmission curve of the H $\alpha$  band. Then, we converted the H $\alpha$  photometry of NGC 6781 in count rates into the flux density using this conversion factor.

### A.2. ESO NTT 3.6 m/EFOSC2

We downloaded raw broadband imaging data at Bessel *B*, *V*, and *R*, taken with the ESO Faint Object Spectrograph and Camera 2 (EFOSC2) mounted on the 3.58 m New Technology Telescope (NTT) at the La Silla Observatory, Chile, from the ESO Science Archive Facility.

We reduced the data and performed photometry of the CSPN and CSPN plus PN with the standard star PG 1657+078 and

<sup>17</sup> <http://www.stsci.edu/hst/observatory/crds/calspec.html>



**Table 11**  
Broadband Flux Densities of NGC 6781 Adopted in the Present Study

CSPN					
Instruments	$\lambda$ ( $\mu\text{m}$ )	Band	$m$	$F_{\lambda}$ ( $\text{erg s}^{-1} \text{cm}^{-2} \mu\text{m}^{-1}$ )	$I_{\lambda}^a$ ( $\text{erg s}^{-1} \text{cm}^{-2} \mu\text{m}^{-1}$ )
WFC	0.3595	<i>u</i>	$16.67 \pm 0.21$	$1.82(-11) \pm 3.52(-12)$	$4.14(-10) \pm 8.94(-11)$
EFOSC2	0.4481	<i>B</i>	$17.15 \pm 0.02$	$9.07(-12) \pm 1.51(-13)$	$1.20(-10) \pm 9.69(-12)$
WFC	0.4640	<i>g</i>	$16.82 \pm 0.21$	$9.47(-12) \pm 1.83(-12)$	$1.11(-10) \pm 2.31(-11)$
EFOSC2	0.5423	<i>V</i>	$16.96 \pm 0.01$	$6.21(-12) \pm 5.72(-14)$	$4.70(-11) \pm 2.95(-12)$
WFPC2	0.5443	F555W	$16.90 \pm 0.11$	$6.21(-12) \pm 6.47(-13)$	$4.66(-11) \pm 5.64(-12)$
EFOSC2	0.6441	<i>R</i>	$16.75 \pm 0.02$	$4.54(-12) \pm 7.54(-14)$	$2.40(-11) \pm 1.29(-12)$
WFPC2	0.7996	F814W	$16.52 \pm 0.04$	$2.97(-12) \pm 1.05(-13)$	$9.79(-12) \pm 4.99(-13)$
WFCAM	1.235	<i>J</i>	$16.32 \pm 0.02$	$9.24(-13) \pm 1.70(-14)$	$1.64(-12) \pm 4.18(-14)$
WFCAM	1.662	<i>H</i>	$16.34 \pm 0.05$	$3.25(-13) \pm 1.45(-14)$	$4.64(-13) \pm 2.13(-14)$
WFCAM	2.159	<i>K</i>	$16.21 \pm 0.05$	$1.41(-13) \pm 7.09(-15)$	$1.77(-13) \pm 9.04(-15)$
CSPN+PN					
GALEX	0.2274	NUV		$1.46(-10) \pm 1.74(-11)$	$5.19(-8) \pm 1.12(-8)$
WFC	0.3595	<i>u</i>	$11.63 \pm 0.01$	$1.87(-9) \pm 1.88(-11)$	$4.27(-8) \pm 4.13(-9)$
EFOSC2	0.4481	<i>B</i>	$11.97 \pm 0.04$	$1.07(-9) \pm 3.87(-11)$	$1.40(-8) \pm 1.22(-9)$
WFC	0.4640	<i>g</i>	$11.37 \pm 0.01$	$1.44(-9) \pm 1.43(-11)$	$1.69(-8) \pm 1.29(-9)$
EFOSC2	0.5423	<i>V</i>	$10.93 \pm 0.02$	$1.61(-9) \pm 2.96(-11)$	$1.22(-8) \pm 7.88(-10)$
WFC	0.6122	<i>r</i>	$10.37 \pm 0.01$	$2.07(-9) \pm 1.15(-11)$	$1.21(-8) \pm 6.61(-10)$
EFOSC2	0.6441	<i>R</i>	$10.15 \pm 0.03$	$1.98(-9) \pm 5.29(-11)$	$1.05(-8) \pm 6.06(-10)$
WFCAM	1.235	<i>J</i>	$10.33 \pm 0.01$	$2.30(-10) \pm 1.06(-12)$	$4.08(-10) \pm 7.42(-12)$
WFCAM	1.662	<i>H</i>	$9.96 \pm 0.01$	$1.15(-10) \pm 1.38(-12)$	$1.64(-10) \pm 2.66(-12)$
WFCAM	2.159	<i>K</i>	$7.55 \pm 0.01$	$4.09(-10) \pm 3.55(-12)$	$5.16(-10) \pm 5.81(-12)$
WISE	3.353	W1	...	...	$7.38(-11) \pm 1.16(-12)$
IRAC	4.500	Band2	...	...	$1.11(-10) \pm 3.33(-12)$
IRAC	5.800	Band3	...	...	$1.32(-10) \pm 3.97(-12)$
IRAC	8.000	Band4	...	...	$8.99(-11) \pm 2.70(-12)$
WISE	11.56	W3	...	...	$5.41(-11) \pm 7.71(-13)$
ISOCAM	14.30	LW3	...	...	$5.65(-11) \pm 1.13(-11)$
WISE	22.09	W4	...	...	$3.23(-11) \pm 5.78(-13)$
PACS	70.00	BLUE	...	...	$4.01(-11) \pm 2.01(-12)$
PACS	160.00	RED	...	...	$7.60(-12) \pm 3.84(-13)$
SPIRE	250.00	PSW	...	...	$1.44(-12) \pm 2.21(-13)$
SPIRE	350.00	PMW	...	...	$4.90(-13) \pm 5.51(-14)$
SPIRE	500.00	PLW	...	...	$7.69(-14) \pm 1.22(-14)$
Radio	6972	43 GHz	...	...	$4.38(-17)$
Radio	9993	30 GHz	...	...	$7.93(-18) \pm 2.13(-19)$
Radio	13627	22 GHz	...	...	$3.07(-18)$
Radio	59959	5 GHz	...	...	$2.70(-19)$
Radio	214138	1.4 GHz	...	...	$2.46(-20) \pm 7.85(-22)$

**Note.** The flux densities at *K* or shorter wavelengths are corrected for the interstellar reddening.

<sup>a</sup> We corrected the observed flux densities  $F_{\lambda}$  in the fifth column by the method explained in Section 2.2 to obtain the dereddened flux densities  $I_{\lambda}$  in the sixth column.  $A(B)$  means  $A \times 10^{-B}$ .

four nearby field stars PG 1657+078A, B, C, and D (Landolt 2009) as calibration standards using IRAF packages in the same procedure used for the INT/WFC data. The gain and readout noise were measured to be  $1.26 \text{ e}^{-} \text{ ADU}^{-1}$  and  $8.27 \text{ e}^{-}$  in the NGC 6781 images and  $1.22 \text{ e}^{-} \text{ ADU}^{-1}$  and  $11.55 \text{ e}^{-}$  in the standard-star images, respectively.

We converted the respective instrumental magnitudes of  $m_B$ ,  $m_V$ , and  $m_R$  into the Landolt system *B*-, *V*-, and *R*-band magnitudes with the following formulae:

$$m_B = -26.659 + V - 0.242 \sec(z_B) + 0.967(B - V), \quad (12)$$

$$m_V = -25.746 + V - 0.425 \sec(z_V) - 0.016(B - V), \quad (13)$$

$$m_R = -25.780 + V - 0.483 \sec(z_R) - 0.968(V - R). \quad (14)$$

### A.3. UKIRT 3.8 m/WFCAM

We downloaded raw broadband imaging data products at *J*, *H*, and *Ks*, taken with the Wide Field Camera (WFCAM) mounted on the 3.8 m United Kingdom Infra-Red Telescope (UKIRT) at the Mauna Kea Observatory, Hawai'i, from the UKIRT WFCAM Science Archive (WSA).

We measured *J*-, *H*-, and *Ks*-band magnitudes of the CSPN and CSPN plus PN based on our own photometry of 96 nearby field stars and converted the respective instrumental magnitudes of  $m_J$ ,  $m_H$ , and  $m_{Ks}$  into the Two Micron All Sky Survey system *J*-, *H*-, and *Ks*-band magnitudes with the following

formulae:

$$m_J = -26.091 + J - 0.047(J - H), \quad (15)$$

$$m_H = -26.444 + J - 0.859(J - H), \quad (16)$$

$$m_K = -25.477 + J - 0.886(J - K_s). \quad (17)$$

#### A.4. HST/WFPC2 Photometry

We downloaded raw broadband imaging data at F555W and F814W (roughly corresponding to Johnson–Cousins  $V$  and  $I_c$ , respectively), taken with the Wide-Field Planetary Camera 2 (WFPC2) on board the 2.4 m *HST*, from the Mikulski Archive for Space Telescopes (MAST). The raw data sets were processed with the `stdas.multidrizzle` package (Koekemoer et al. 2003) included in PYRAF. We performed aperture photometry for the CSPN after we subtracted the nearby stars by the PSF fitting using the IRAF packages `noao.digiphot`.

## Appendix B Spectroscopy Data and Measurements

### B.1. WHT 4.2 m/ISIS Optical Spectrum

We downloaded raw long-slit spectroscopic data in the optical taken with the ISIS mounted on the 4.2 m WHT at the Observatorio del Roque de los Muchachos, La Palma, Spain, from the CASU Astronomical Data Centre.

The observations covered spatially the bulk of the nebula by scanning the central part of the nebula with the  $79''.6 \times 1''.0$  slit during integration (Figure 2). The spectral coverage was 4170–4970/5190–6670 Å and 360–4400/6520–8010 Å with the R600B (blue) and R316R (red) gratings, respectively, at an airmass of  $\sim 1.1$  with a seeing of  $0''.7$ – $0''.8$ , according to the observation log. Before and after observing NGC 6781, the CuAr+CuNe lamp frames were taken for the wavelength calibration. The standard star BD +28°4211 was observed with the  $6''.1$ -wide slit at the airmass of  $\sim 1.0$ .

Plasma diagnostics and chemical abundance analyses based on these data in conjunction with data taken with *ISO* were presented by Liu et al. (2004a, 2004b). We re-reduced the data by ourselves so that we could perform our own calculations of ionic and elemental abundances with measurements made with the *Spitzer*/*IRS* and *Herschel*/*PACS* spectra in terms of the line fluxes per arcsec<sup>2</sup>. Data reduction was done with the two-dimensional spectra reduction package `NOAO.TWODSPEC` in IRAF following the standard procedure, i.e., bias subtraction, flat-fielding, spectra aperture alignment, distortion correction along the spatial direction, wavelength calibration, and cosmic-ray subtraction.

We corrected the count rates reduced by airmass extinction using the atmospheric extinction table provided by the La Palma Observatory and performed the flux calibrations. We extracted 199 and 181 spatial pixels in the blue and red arm, respectively, and summed up all the spatial pixels. In the end, we obtained a single 3600–8010 Å spectrum of a  $79''.6 \times 1''.0$  region of the nebula.

### B.2. The $H\alpha$ and $H\beta$ Line Fluxes of the Entire Nebula

Because the filter transmission of the IPHAS  $H\alpha$  band includes contributions from the  $H\alpha$  and neighboring [N II]  $\lambda 6527/\lambda 6548/\lambda 6583$  lines, as well as the nebular and stellar continuum, we have to subtract the contributions other than the  $H\alpha$  line itself as much as possible in order to obtain the clean  $H\alpha$  line flux. We used the ISIS spectrum to estimate contributions to the  $H\alpha$ -band line flux by the neighboring lines. Taking into account the IPHAS  $H\alpha$  filter

transmission, we compared the  $H\alpha$  line flux of NGC 6781 measured from the IPHAS image of the entire nebula,  $F_\lambda(\text{IPHAS}, H\alpha)$ , with that measured from the ISIS spectrum covering a  $79''.6 \times 1''.0$  region,  $F_\lambda(\text{ISIS}, H\alpha)$ . The resulting scaling factor  $F_\lambda(\text{IPHAS}, H\alpha)/F_\lambda(\text{ISIS}, H\alpha)$  turned out to be 133.33. Using this factor, the ISIS spectrum over 3600–8010 Å was scaled to represent the spectrum of the entire nebula, and the clean  $H\alpha$  and  $H\beta$  line fluxes of the entire nebula,  $F(H\alpha)$  of  $6.95(-11) \pm 8.61(-13) \text{ erg s}^{-1} \text{ cm}^{-2}$  and  $F(H\beta)$  of  $1.22(-11) \pm 1.59(-12) \text{ erg s}^{-1} \text{ cm}^{-2}$ , were determined. We used these  $H\alpha$  and  $H\beta$  line fluxes of the entire NGC 6781 nebula to normalize the line fluxes detected in the *Spitzer*/*IRS* and *Herschel*/*PACS* and *SPIRE* spectra.

### B.3. Spitzer/IRS Mid-IR Spectrum

We downloaded long-slit spectroscopic data in the mid-IR taken with the Infra-Red Spectrograph (IRS) on board the 0.85 m *Spitzer* as part of the IRS Calibration Program (AOR-KEY:16099072), from the *Spitzer* Heritage Archive<sup>18</sup> (SHA).

As indicated in Figure 2, we only used the spectra taken from the central parts of the nebula, covering the  $57'' \times 3''.7 \times 2$  regions along the N–S direction and  $168'' \times 10''.7$  region along the E–W direction in the Short-Low (5.1–14.3  $\mu\text{m}$ ) and Long-Low (13.9–39.9  $\mu\text{m}$ ) bands, respectively. We reduced the adopted raw data using the data reduction packages SMART v.8.2.9 (Higdon et al. 2004) and IRSCLEAN v.2.1.1 (Ingalls 2011), provided by the *Spitzer* Science Center.

Then, we scaled the measured flux densities of the single 5.2–39.9  $\mu\text{m}$  spectrum by a constant factor of 14.40, which was determined to match the flux densities of the entire PN (see Figure 2) at the *Spitzer*/*IRAC* Band-4 ( $\lambda_c = 8.0 \mu\text{m}$ ,  $1.92 \pm 0.058 \text{ Jy}$ ), *WISE* W3 ( $\lambda_c = 11.56 \mu\text{m}$ ,  $2.41 \pm 0.034 \text{ Jy}$ ), the *ISO*/*ISOCAM* 14.3  $\mu\text{m}$  ( $3.85 \pm 0.77 \text{ Jy}$ ), and *WISE* W4 ( $\lambda_c = 22.1 \mu\text{m}$ ,  $5.25 \pm 0.094 \text{ Jy}$ ).

### B.4. Herschel Far-IR Spectrum

We adopted *Herschel* far-IR spectra presented by Ueta et al. (2014), especially those that covered the central part of the nebula (Figure 2). To scale the line fluxes detected by *PACS* and *SPIRE* for the entire nebula, we synthesized the  $H\beta$  image based on the the  $H\alpha$  image taken with the Andalucia Faint Object Spectrograph and Camera (ALFOSC) mounted on the 2.5 m Nordic Optical Telescope (NOT) at the Observatorio del Roque de los Muchachos, La Palma, Spain, presented by Phillips et al. (2011). Because the ALFOSC  $H\alpha$  filter (IAC # 40<sup>19</sup>) has a central wavelength of 6567 Å with a bandwidth of 8 Å, the contributions from the [N II]  $\lambda 6548/\lambda 6583$  lines and the underlying continuum are considered to be negligible. After field stars overlapped with the nebula were removed by PSF fitting, we scaled the  $H\alpha$  map so that photometry of the entire nebula would yield  $I(H\beta)$ . This scaled  $H\alpha$  map would represent the  $H\beta$  map under the assumption that the emitting regions of  $H\alpha$  and  $H\beta$  are the same. Using this synthesized  $H\beta$  image, we measured the counts in the regions covered by the *PACS* and *SPIRE* observations and scaled the measured line fluxes according to the  $H\beta$  fluxes.

<sup>18</sup> <http://sha.ipac.caltech.edu/applications/Spitzer/SHA/>

<sup>19</sup> <http://www.not.iac.es/instruments/filters/filters.php>

**Table 12**  
Relative Emission Line Fluxes of NGC 6781 Adopted in the Present Study

$\lambda$ (Å)	Line	$I(\lambda)$ ( $I(H\beta) = 100$ )	$\lambda$ ( $\mu\text{m}$ )	Line	$I(\lambda)$ ( $I(H\beta) = 100$ )
ING/WHT ISIS			<i>Spitzer</i> IRS		
3726.03	[O II]	$268.177 \pm 8.139$	5.51	H <sub>2</sub> 0-0 S(7)	$30.757 \pm 7.120$
3728.82	[O II]	$316.109 \pm 8.809$	6.11	H <sub>2</sub> 0-0 S(6)	$17.269 \pm 2.594$
3750.15	H12	$5.048 \pm 0.678$	6.91	H <sub>2</sub> 0-0 S(5)	$52.628 \pm 12.762$
3770.63	H11	$3.885 \pm 0.677$	8.02	H <sub>2</sub> 0-0 S(4)	$19.413 \pm 2.378$
3797.90	H10	$5.055 \pm 0.880$	8.99	[Ar III]	$22.867 \pm 1.731$
3835.38	H9	$9.414 \pm 1.037$	9.67	H <sub>2</sub> 0-0 S(3)	$25.792 \pm 4.127$
3869.07	[Ne III]	$125.764 \pm 3.150$	10.51	[S IV]	$49.677 \pm 3.516$
3888.86	H8+He I	$27.314 \pm 1.517$	11.30	PAH+H I	$3.119 \pm 0.282$
3967.79	[Ne III]	$37.177 \pm 1.290$	12.29	H <sub>2</sub> 0-0 S(2)	$6.314 \pm 0.619$
3970.07	H7	$20.340 \pm 0.882$	12.81	[Ne II]	$14.802 \pm 1.017$
4026.32	He I	$2.932 \pm 1.099$	15.55	[Ne III]	$234.571 \pm 16.147$
4068.60	[S II]	$3.230 \pm 0.706$	17.04	H <sub>2</sub> 0-0 S(1)	$9.241 \pm 0.657$
4101.74	H6(H $\delta$ )	$31.011 \pm 0.846$	17.88	[P III]+[Fe II]?	$1.736 \pm 0.131$
4267.26	C II	$2.070 \pm 0.495$	18.71	[S III]	$46.998 \pm 3.277$
4340.46	H5(H $\gamma$ )	$47.863 \pm 1.481$	20.30	[Cl IV]	$0.333 \pm 0.061$
4363.21	[O III]	$5.225 \pm 0.343$	21.82	[Ar III]	$1.622 \pm 0.131$
4471.46	He I	$5.099 \pm 0.407$	25.88	[O IV]	$174.473 \pm 12.154$
4641.10	N III	$0.943 \pm 0.634$	33.47	[S III]	$50.073 \pm 3.480$
4685.76	He II	$8.201 \pm 0.284$	34.81	[Si II]	$12.287 \pm 1.143$
4712.62	He I	$1.341 \pm 0.198$	36.00	[Ne III]	$17.011 \pm 1.387$
4740.17	[Ar IV]	$0.671 \pm 0.262$	<i>Herschel</i> PACS		
4861.33	H4(H $\beta$ )	$100.000 \pm 1.562$	57.32	[N III]	$78.829 \pm 9.712$
4958.91	[O III]	$274.612 \pm 4.087$	63.17	[O I]	$33.175 \pm 4.186$
5198.84	[N I]	$6.341 \pm 0.782$	88.33	[O III]	$190.944 \pm 23.417$
5517.72	[Cl III]	$0.838 \pm 0.381$	119.20	OH	$0.590 \pm 0.105$
5537.89	[Cl III]	$0.577 \pm 0.467$	119.40	OH	$0.655 \pm 0.116$
5577.95	[O I]	$3.510 \pm 0.599$	121.73	[N II]	$7.880 \pm 0.973$
5754.64	[N II]	$6.674 \pm 0.194$	145.50	[O I]	$2.904 \pm 0.367$
5875.58	He I	$16.406 \pm 0.552$	153.00	OH <sup>+</sup>	$0.296 \pm 0.070$
5888.49	[Mn V]?	$0.576 \pm 0.203$	157.64	[C II]	$15.915 \pm 1.955$
6300.28	[O I]	$32.959 \pm 0.765$	<i>Herschel</i> SPIRE		
6312.10	[S III]	$1.698 \pm 0.450$	205.40	[N II]	$1.607 \pm 0.257$
6363.79	[O I]	$10.804 \pm 0.301$	289.10	CO $J = 9-8$	$0.528 \pm 0.142$
6548.04	[N II]	$132.950 \pm 4.709$	290.20	OH <sup>+</sup>	$0.539 \pm 0.143$
6562.80	H3(H $\alpha$ )	$286.124 \pm 7.646$	308.40	OH <sup>+</sup>	$0.495 \pm 0.067$
6583.46	[N II]	$410.904 \pm 10.523$	325.30	CO $J = 8-7$	$0.473 \pm 0.067$
6678.14	He I	$4.405 \pm 0.322$	329.70	OH <sup>+</sup>	$0.083 \pm 0.051$
6716.44	[S II]	$26.242 \pm 0.738$	370.30	[C I]	$0.354 \pm 0.045$
6730.82	[S II]	$21.854 \pm 0.620$	371.60	CO $J = 7-6$	$0.969 \pm 0.121$
7065.33	He I	$3.844 \pm 0.321$	433.50	CO $J = 6-5$	$0.572 \pm 0.074$
7135.80	[Ar III]	$22.349 \pm 0.707$	520.30	CO $J = 5-4$	$0.374 \pm 0.099$
7281.72	He I	$0.688 \pm 0.078$	650.30	CO $J = 4-3$	$0.182 \pm 0.031$
7320.03	[O II]	$6.490 \pm 0.279$	...	...	...
7330.27	[O II]	$5.396 \pm 0.261$	...	...	...
7751.10	[Ar III]	$5.351 \pm 0.277$	...	...	...

### Appendix C Ionic Abundance Derivations

Tables 13 and 14 support our ionic and elemental abundance derivations.



**Table 13**  
Adopted  $T_e$  and  $n_e$  Pairs for Ionic Abundance Calculations

Type of Line	$T_e$ (K)	$n_e$ ( $\text{cm}^{-3}$ )	Ions
RL	7070 $\pm$ 1880	100	He <sup>+</sup> , He <sup>2+</sup>
RL	9350 $\pm$ 400	10,000	C <sup>2+</sup>
CEL	9350 $\pm$ 400	220 $\pm$ 50	Ne <sup>+</sup> , S <sup>2+</sup> , Cl <sup>2+</sup> , Ar <sup>2+</sup>
CEL	9650 $\pm$ 200	260 $\pm$ 80	O <sup>+</sup>
CEL	10 050 $\pm$ 210	220 $\pm$ 50	O <sup>2+</sup>
CEL	10 050 $\pm$ 210	1020 $\pm$ 300	S <sup>3+</sup>
CEL	10 340 $\pm$ 250	220 $\pm$ 50	O <sup>3+</sup> , Ne <sup>2+</sup> , Cl <sup>3+</sup>
CEL	10 520 $\pm$ 1820	260 $\pm$ 80	C <sup>+</sup> , N <sup>0</sup> , O <sup>0</sup> , Si <sup>+</sup> , S <sup>+</sup>
CEL	10 800 $\pm$ 170	260 $\pm$ 80	N <sup>+</sup>

**Table 14**  
Ionic Abundances and Elemental Abundance Derivations Using the ICFs

X	X <sup>m+</sup>	$\lambda$	$I(\lambda)$	X <sup>m+</sup> /H <sup>+</sup>	X	X <sup>m+</sup>	$\lambda$	$I(\lambda)$	X <sup>m+</sup> /H <sup>+</sup>	
He	He <sup>+</sup>	4026.32 Å	2.932 $\pm$ 1.099	1.26(−1) $\pm$ 6.89(−2)	Ne	Ne <sup>+</sup>	12.81 $\mu\text{m}$	14.802 $\pm$ 1.017	2.06(−5) $\pm$ 1.50(−6)	
		4471.46 Å	5.099 $\pm$ 0.407	1.01(−1) $\pm$ 3.95(−2)			Ne <sup>2+</sup>	3869.07 Å	125.764 $\pm$ 3.15	1.22(−4) $\pm$ 1.22(−5)
		4712.62 Å	1.341 $\pm$ 0.198	3.06(−1) $\pm$ 9.55(−2)		3967.79 Å		37.177 $\pm$ 1.29	1.19(−4) $\pm$ 1.23(−5)	
		5875.58 Å	16.406 $\pm$ 0.552	1.14(−1) $\pm$ 4.48(−2)		15.55 $\mu\text{m}$	234.571 $\pm$ 16.147	1.48(−4) $\pm$ 1.03(−5)		
		6678.14 Å	4.405 $\pm$ 0.322	1.07(−1) $\pm$ 4.50(−2)		36.00 $\mu\text{m}$	17.011 $\pm$ 1.387	1.20(−4) $\pm$ 9.87(−6)		
		7065.33 Å	3.844 $\pm$ 0.321	1.86(−1) $\pm$ 5.45(−2)		ICF(Ne)		1.00		
	7281.72 Å	0.688 $\pm$ 0.078	1.07(−1) $\pm$ 3.41(−2)	ICF(Si)		1.41(−4) $\pm$ 6.67(−6)				
	He <sup>2+</sup>	4685.76 Å	8.201 $\pm$ 0.284	6.48(−3) $\pm$ 2.58(−3)		Si	Si <sup>+</sup>	34.81 $\mu\text{m}$	12.287 $\pm$ 1.143	1.59(−6) $\pm$ 1.49(−7)
		ICF(He)		1.00				ICF(Si)		6.80 $\pm$ 1.75
	C	C <sup>+</sup>	157.64 $\mu\text{m}$	15.915 $\pm$ 1.955		2.70(−4) $\pm$ 5.13(−5)	S	S <sup>+</sup>	4068.60 Å	3.23 $\pm$ 0.706
4267.26 Å			2.070 $\pm$ 0.495	2.00(−3) $\pm$ 4.95(−4)	6716.44 Å	26.242 $\pm$ 0.738			1.17(−6) $\pm$ 4.31(−7)	
ICF(C)		2.03 $\pm$ 3.19(−1)	4.06(−3) $\pm$ 1.19(−3) <sup>†</sup>	6730.82 Å	21.854 $\pm$ 0.62	1.17(−6) $\pm$ 4.75(−7)				
		<b>9.89(−4) <math>\pm</math> 3.14(−4)<sup>†</sup></b>	1.19(−6) $\pm$ 2.97(−7)	ICF(S)		1.00				
N	N <sup>0</sup>	5198/200 Å	6.341 $\pm$ 0.782	4.90(−5) $\pm$ 2.95(−6)	S <sup>2+</sup>	6312.10 Å	1.698 $\pm$ 0.45	5.78(−6) $\pm$ 1.12(−6)		
		5754.64 Å	6.638 $\pm$ 0.194	6.57(−5) $\pm$ 5.50(−6)			18.71 $\mu\text{m}$	46.998 $\pm$ 3.277	5.87(−6) $\pm$ 4.37(−7)	
		6548.04 Å	132.950 $\pm$ 4.709	6.35(−5) $\pm$ 3.34(−6)		33.47 $\mu\text{m}$	50.073 $\pm$ 3.48	5.80(−6) $\pm$ 6.12(−7)		
		6583.46 Å	410.904 $\pm$ 10.523	6.63(−5) $\pm$ 3.10(−6)		S <sup>3+</sup>	10.51 $\mu\text{m}$	49.677 $\pm$ 3.516	5.84(−6) $\pm$ 3.50(−7)	
	121.73 $\mu\text{m}$	7.880 $\pm$ 0.973	5.36(−5) $\pm$ 1.20(−5)	ICF(S)				1.00		
	N <sup>2+</sup>	57.32 $\mu\text{m}$	78.829 $\pm$ 9.712	7.01(−5) $\pm$ 9.08(−6)	Cl	Cl <sup>2+</sup>	5517.72 Å	0.838 $\pm$ 0.381	1.07(−7) $\pm$ 5.03(−8)	
			ICF(N)				1.05 $\pm$ 5.76(−2)	Cl <sup>3+</sup>	20.30 $\mu\text{m}$	0.333 $\pm$ 0.061
				<b>1.42(−4) <math>\pm</math> 1.27(−5)</b>		ICF(Cl)			1.17 $\pm$ 9.07(−2)	
		<b>1.43(−7) <math>\pm</math> 6.01(−8)</b>								
O	O <sup>0</sup>	6300.28 Å	32.959 $\pm$ 0.765	7.05(−5) $\pm$ 4.03(−5)	Ar	Ar <sup>2+</sup>	7135.80 Å	22.349 $\pm$ 0.707	2.45(−6) $\pm$ 2.73(−7)	
		6363.79 Å	10.804 $\pm$ 0.301	7.23(−5) $\pm$ 4.14(−5)			7751.10 Å	5.351 $\pm$ 0.277	2.45(−6) $\pm$ 2.90(−7)	
		145.50 $\mu\text{m}$	2.904 $\pm$ 0.367	5.38(−4) $\pm$ 1.05(−4)		8.99 $\mu\text{m}$	22.867 $\pm$ 1.731	2.43(−6) $\pm$ 1.94(−7)		
				<b>1.04(−4) <math>\pm</math> 2.78(−5)</b>		21.82 $\mu\text{m}$	1.622 $\pm$ 0.131	2.56(−6) $\pm$ 2.19(−7)		
	O <sup>+</sup>	3726.04 Å	268.177 $\pm$ 8.139	2.74(−4) $\pm$ 3.09(−5)	Ar <sup>3+</sup>	4740.20 Å	0.671 $\pm$ 0.262	2.44(−6) $\pm$ 1.39(−7)		
			3728.82 Å	316.109 $\pm$ 8.809			2.72(−4) $\pm$ 1.56(−5)	ICF(Ar)		1.17 $\pm$ 9.07(−2)
		7320/30 Å	11.625 $\pm$ 0.382	2.77(−4) $\pm$ 5.01(−5)				<b>3.10(−6) <math>\pm</math> 3.06(−7)</b>		
				<b>2.72(−4) <math>\pm</math> 1.34(−5)</b>						
	O <sup>2+</sup>	4363.21 Å	5.187 $\pm$ 0.343	2.79(−4) $\pm$ 4.35(−5)						
			4958.91 Å	274.612 $\pm$ 4.087	2.78(−4) $\pm$ 2.07(−5)					
		88.33 $\mu\text{m}$	190.944 $\pm$ 23.417	2.78(−4) $\pm$ 4.30(−5)						
	O <sup>3+</sup>	25.88 $\mu\text{m}$	174.473 $\pm$ 12.154	3.02(−5) $\pm$ 2.10(−6)						
ICF(O)			1.00							
		<b>5.81(−4) <math>\pm</math> 2.19(−5)</b>								

**Note.** The RL C abundance using the RL C II  $\lambda$ 4267 line is 4.06(−3), and the *expected* CEL C abundance using the average C<sup>2+</sup>(RL)/C<sup>2+</sup>(CEL) ratio of 4.10  $\pm$  0.49 among 58 PNe (Otsuka et al. 2011) is 9.89(−4). The ICF(X) value of the element “X” and the resulting elemental abundance, X/H = ICF(X)  $\times$  ( $\sum_{m=1} X^{m+}/H^+$ ), are shown in bold.

## Appendix D

### Comparison of Relative Line Fluxes, Band Fluxes, and Flux Densities between the Observation and the Cloudy Model

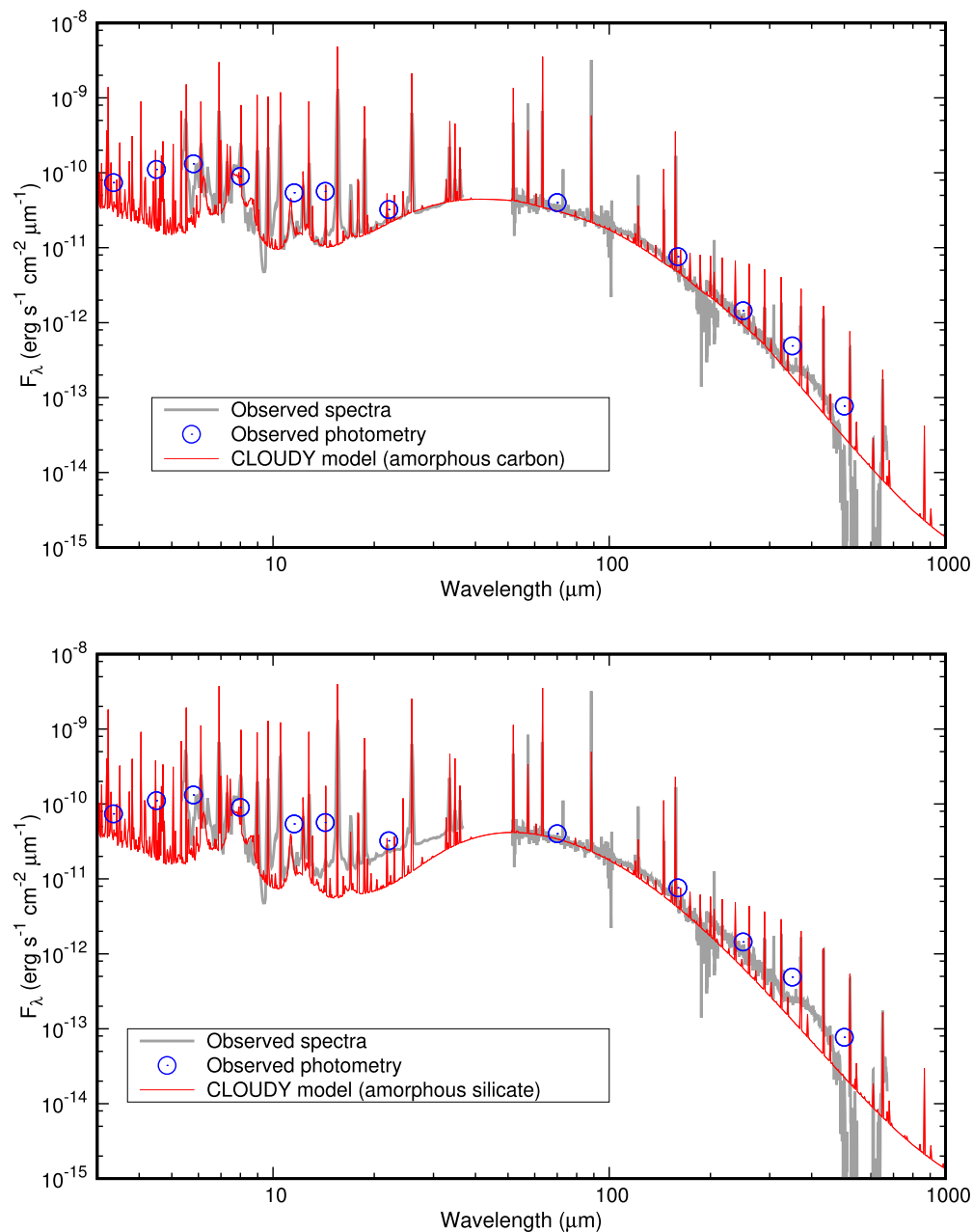
Table 15 and Figure 13 support our photoionization model.

**Table 15**  
Comparison between the Observed and Cloudy Model Predicted Line Fluxes, Band Fluxes, and Band Flux Densities

$\lambda_{\text{lab}}$ (Å)	Line	$I_{\text{model}}(\lambda)$ ( $I(\text{H}\beta) = 100$ )	$I_{\text{obs}}(\lambda)$ ( $I(\text{H}\beta) = 100$ )	$\lambda_{\text{lab}}$ ( $\mu\text{m}$ )	Line	$I_{\text{model}}(\lambda)$ ( $I(\text{H}\beta) = 100$ )	$I_{\text{obs}}(\lambda)$ ( $I(\text{H}\beta) = 100$ )
3726	[O II]	269.526	268.117	2.12	H <sub>2</sub> 1-0S(1)	39.911	57.189
3729	[O II]	274.987	316.109	5.51	H <sub>2</sub> 0-0S(7)	13.856	30.064
3750	H12	3.048	5.048	6.11	H <sub>2</sub> 0-0S(6)	9.834	19.021
3771	H11	3.964	3.885	6.91	H <sub>2</sub> 0-0S(5)	43.037	56.328
3798	H10	5.293	5.055	8.02	H <sub>2</sub> 0-0S(4)	13.637	31.052
3835	H9	7.299	9.414	8.99	[Ar III]	19.674	22.867
3869	[Ne III]	138.608	125.764	9.67	H <sub>2</sub> 0-0S(3)	24.196	25.792
3889	H8+He I	23.293	27.314	10.51	[S IV]	35.542	49.677
3967	[Ne III]	41.775	37.177	12.29	H <sub>2</sub> 0-0S(2)	2.723	5.314
3970	H7	15.876	20.340	12.81	[Ne II]	20.408	14.802
4026	He I	2.693	2.932	15.57	[Ne III]	164.303	234.571
4069	[S II]	10.332	3.230	17.04	H <sub>2</sub> 0-0S(1)	1.281	9.241
4102	H $\delta$	25.847	31.011	18.72	[S III]	37.567	46.998
4267	C II	0.261	2.070	20.33	[C IV]	0.232	0.333
4340	H $\gamma$	46.714	47.863	21.86	[Ar III]	1.430	1.622
4363	[O III]	6.757	5.225	25.90	[O IV]	102.632	174.473
4471	He I	5.725	5.099	33.46	[S III]	39.736	50.073
4686	He II	10.954	8.201	34.79	[Si II]	22.045	12.287
4713	He I+[Ar IV]	1.580	1.341	36.01	[Ne III]	13.943	17.011
4740	[Ar IV]	0.746	0.671	57.00	[N III]	47.680	78.829
4861	H $\beta$	100.000	100.000	63.00	[O I]	282.115	33.175
4959	[O III]	272.773	274.612	88.00	[O III]	121.725	190.944
5199	[N I]	32.473	6.341	119.2	OH	0.561	0.590
5518	[Cl III]	0.783	0.838	119.4	OH	0.784	0.650
5538	[Cl III]	0.594	0.577	121.0	[N II]	6.627	7.880
5578	[O I]	1.257	3.510	146.0	[O I]	19.410	2.904
5755	[N II]	5.897	6.674	158.0	[C II]	49.076	15.915
5876	He I	16.425	16.406	205.0	[N II]	1.161	1.607
6300	[O I]	76.664	32.959	289.1	CO $J = 9-8$	1.611	0.528
6312	[S III]	2.426	1.698	325.3	CO $J = 8-7$	1.480	0.473
6364	[O I]	24.449	10.804	370.3	[C I]	0.082	0.354
6548	[N II]	136.031	132.950	371.6	CO $J = 7-6$	1.221	0.969
6563	H $\alpha$	283.796	286.124	433.5	CO $J = 6-5$	0.861	0.241
6583	[N II]	401.428	410.904	520.3	CO $J = 5-4$	0.477	0.374
6678	He I	4.629	4.405	650.3	CO $J = 4-3$	0.185	0.182
6716	[S II]	72.423	26.242	...	...	...	...
6731	[S II]	69.778	21.854	...	...	...	...
7065	He I	3.277	3.844	...	...	...	...
7136	[Ar III]	21.948	22.349	...	...	...	...
7282	He I	0.871	0.688	...	...	...	...
7320	[O II]	8.122	6.490	...	...	...	...
7330	[O II]	6.481	5.396	...	...	...	...
7751	[Ar III]	5.296	5.351	...	...	...	...
0.2274(0.073)	NUV	1032.146	3045.783	13.20(0.30)	IRS-g	3.243	3.244
0.3595(0.056)	<i>u</i>	1285.318	1921.023	14.00(0.20)	IRS-h	2.534	2.974
0.464(0.116)	<i>g</i>	1793.895	1577.160	14.65(0.20)	IRS-i	1.643	2.389
0.5423(0.088)	<i>V</i>	1149.396	859.786	16.50(0.40)	IRS-j	4.326	4.913
0.6122(0.111)	<i>r</i>	1364.283	1084.993	17.50(0.30)	IRS-k	3.419	3.495
0.6441(0.170)	<i>R</i>	1709.897	1434.254	18.30(0.20)	IRS-l	2.342	2.626
1.235(0.162)	<i>J</i>	81.943	53.230	19.75(0.70)	IRS-m	9.667	10.167
1.662(0.251)	<i>H</i>	41.969	23.302	20.00(0.30)	IRS-n	4.221	4.467
2.159(0.262)	<i>K</i>	65.999	34.696	21.00(0.30)	IRS-o	4.773	4.956
3.353(0.663)	W1	36.711	39.400	22.50(0.40)	IRS-p	7.625	7.643
4.50(0.86)	IRAC-2	22.251	76.892	23.50(0.40)	IRS-q	8.268	8.028
5.80(1.26)	IRAC-3	71.323	134.290	27.00(0.40)	IRS-r	10.790	9.471
8.00(2.53)	IRAC-4	194.977	183.207	28.00(0.50)	IRS-s	14.412	12.840
7.70(0.30)	IRS-a	20.084	28.010	29.00(0.50)	IRS-t	15.044	13.318
8.60(0.20)	IRS-b	6.274	4.248	30.00(0.50)	IRS-u	15.787	14.200
9.35(0.15)	IRS-c	1.497	0.622	31.00(0.50)	IRS-v	16.379	14.469
10.90(0.20)	IRS-d	1.921	2.010	32.00(0.50)	IRS-w	16.988	15.703
11.30(0.50)	IRS-e	10.094	8.517	35.40(0.20)	IRS-y	7.830	7.571
12.00(0.20)	IRS-f	2.414	2.836	...	...	...	...
$\lambda$	Band	$F_{\nu}(\text{model})$ (Jy)	$F_{\nu}(\text{obs})$ (Jy)	$\lambda$	Band	$F_{\nu}(\text{model})$ (Jy)	$F_{\nu}(\text{obs})$ (Jy)
17.0 $\mu\text{m}$	IRS-1	1.371	2.688	300.0 $\mu\text{m}$	SPIRE-2	13.250	14.770
20.0 $\mu\text{m}$	IRS-2	2.386	5.421	350.0 $\mu\text{m}$	SPIRE-3	9.506	14.560



**Table 15**  
(Continued)

$\lambda$	Band	$F_{\nu}(\text{model})$	$F_{\nu}(\text{obs})$	$\lambda$	Band	$F_{\nu}(\text{model})$	$F_{\nu}(\text{obs})$
30.0 $\mu\text{m}$	IRS-3	12.170	10.510	400.0 $\mu\text{m}$	SPIRE-4	7.022	8.539
70.0 $\mu\text{m}$	PACS-1	54.970	55.360	450.0 $\mu\text{m}$	SPIRE-5	5.411	5.551
80.0 $\mu\text{m}$	PACS-2	58.710	60.520	43 GHz/7 mm	Radio-1	0.378	0.710
100.0 $\mu\text{m}$	PACS-3	60.610	65.810	30 GHz/1 cm	Radio-2	0.395	0.264
110.0 $\mu\text{m}$	PACS-4	57.910	66.010	22 GHz/1.3 cm	Radio-3	0.409	0.190
130.0 $\mu\text{m}$	PACS-5	50.590	61.740	5 GHz/6 cm	Radio-4	0.481	0.323
170.0 $\mu\text{m}$	PACS-6	36.820	36.800	1.4 GHz/21 cm	Radio-5	0.531	0.377
250.0 $\mu\text{m}$	SPIRE-1	18.940	22.410				

**Note.** $\Delta\lambda$  Indicates the Bandwidth of Each Band.**Figure 13.** Best-fit model SEDs: with amorphous carbon grains only (top) and with amorphous silicate grains only (bottom). The amorphous carbon grain model gives better fitting to the observed continuum fluxes than the amorphous silicate grain model, especially in the mid-IR (10–40  $\mu\text{m}$ ) and far-IR (>70  $\mu\text{m}$ ).



## ORCID iDs

Masaaki Otsuka  <https://orcid.org/0000-0001-7076-0310>  
 Albert A. Zijlstra  <https://orcid.org/0000-0002-3171-5469>  
 Eva Villaver  <https://orcid.org/0000-0003-4936-9418>  
 Joel Kastner  <https://orcid.org/0000-0002-3138-8250>

## References

- Ahn, C. P., Alexandroff, R., Allende Prieto, C., et al. 2012, *ApJS*, **203**, 21  
 Aleman, I., Ueta, T., Ladjal, D., et al. 2014, *A&A*, **566**, A79  
 Aleman, I., Zijlstra, A. A., Matsuura, M., Gruenwald, R., & Kimura, R. K. 2011, *MNRAS*, **416**, 790  
 Ali, A., Ismail, H. A., Snaid, S., & Sabin, L. 2013, *A&A*, **558**, A93  
 Arias, L., & Rosado, M. 2002, *RMxAC*, **12**, 158  
 Bachiller, R., Forveille, T., Huggins, P. J., & Cox, P. 1997, *A&A*, **324**, 1123  
 Bachiller, R., Huggins, P. J., Cox, P., & Forveille, T. 1993, *A&A*, **267**, 177  
 Baker, J. G., & Menzel, D. H. 1938, *ApJ*, **88**, 52  
 Benjamin, R. A., Skillman, E. D., & Smits, D. P. 1999, *ApJ*, **514**, 307  
 Bergstedt, J. 2015, Master's thesis, Uppsala Univ., Department of Physics and Astronomy  
 Cardelli, J. A., Clayton, G. C., & Mathis, J. S. 1989, *ApJ*, **345**, 245  
 Chu, Y.-H., Guerrero, M. A., Gruendl, R. A., Williams, R. M., & Kaler, J. B. 2001, *ApJL*, **553**, L69  
 Condon, J. J., Cotton, W. D., Greisen, E. W., et al. 1998, *AJ*, **115**, 1693  
 Corradi, R. L. M., & Schwarz, H. E. 1995, *A&A*, **293**, 871  
 Cox, N. L. J., Pilleri, P., Berné, O., Cernicharo, J., & Joblin, C. 2016, *MNRAS*, **456**, L89  
 Dabrowski, I. 1984, *CaJPh*, **62**, 1639  
 Davey, A. R., Storey, P. J., & Kisielius, R. 2000, *A&AS*, **142**, 85  
 Delgado-Inglada, G., Morisset, C., & Stasińska, G. 2014, *MNRAS*, **440**, 536  
 Delgado-Inglada, G., & Rodríguez, M. 2014, *ApJ*, **784**, 173  
 Duchin, D., De Marco, O., Frew, D. J., et al. 2015, *MNRAS*, **448**, 3132  
 Draine, B. T., & Li, A. 2007, *ApJ*, **657**, 810  
 Ferland, G. J., Porter, R. L., van Hoof, P. A. M., et al. 2013, *RMxAA*, **49**, 137  
 Flower, D. R., & Pineau Des Forêts, G. 2010, *MNRAS*, **406**, 1745  
 Frew, D. J. 2008, PhD thesis, Macquarie Univ.  
 Frew, D. J., Parker, Q. A., & Bojičić, I. S. 2016, *MNRAS*, **455**, 1459  
 Gesicki, K., Zijlstra, A. A., & Morisset, C. 2016, *A&A*, **585**, A69  
 Guerrero, M. A., Villaver, E., Machado, A., Garcia-Lario, P., & Prada, F. 2000, *ApJS*, **127**, 125  
 Guzman-Ramirez, L., Lagadec, E., Jones, D., Zijlstra, A. A., & Gesicki, K. 2014, *MNRAS*, **441**, 364  
 Hasegawa, T., Volk, K., & Kwok, S. 2000, *ApJ*, **532**, 994  
 Henney, W. J., Williams, R. J. R., Ferland, G. J., Shaw, G., & O'Dell, C. R. 2007, *ApJL*, **671**, L137  
 Henry, R. B. C., Speck, A., Karakas, A. I., Ferland, G. J., & Maguire, M. 2012, *ApJ*, **749**, 61  
 Higdon, S. J. U., Devost, D., Higdon, J. L., et al. 2004, *PASP*, **116**, 975  
 Hiriart, D. 2005, *A&A*, **434**, 181  
 Houck, J. R., Roellig, T. L., van Cleve, J., et al. 2004, *ApJS*, **154**, 18  
 Ingalls, J. G. 2011, *IRSCLEAN User's Guide*, Spitzer Heritage Archive Documentation  
 Jones, D., & Boffin, H. M. J. 2017, *NatAs*, **1**, 0117  
 Karakas, A., & Lattanzio, J. C. 2007, *PASA*, **24**, 103  
 Karakas, A. I. 2010, *MNRAS*, **403**, 1413  
 Kastner, J. H., Montez, R., Jr., Balick, B., et al. 2012, *AJ*, **144**, 58  
 Kastner, J. H., Weintraub, D. A., Gatley, I., Merrill, K. M., & Probst, R. G. 1996, *ApJ*, **462**, 777  
 Knapp, G. R. 1985, *ApJ*, **293**, 273  
 Koekemoer, A. M., Fruchter, A. S., Hook, R. N., & Hack, W. 2003, in *HST Calibration Workshop: Hubble after the Installation of the ACS and the NICMOS Cooling System*, ed. S. Arribas, A. Koekemoer, & B. Whitmore (Baltimore, MD: STScI), 337  
 Kwok, S. 2007, *Physics and Chemistry of the Interstellar Medium* (Mill Valley, CA: Univ. Science Books)  
 Landolt, A. U. 2009, *AJ*, **137**, 4186  
 Liu, X.-W., Storey, P. J., Barlow, M. J., et al. 2000, *MNRAS*, **312**, 585  
 Liu, X.-W. 2006, in *IAU Symp. 234, Planetary Nebulae in Our Galaxy and Beyond*, ed. M. J. Barlow & R. H. Méndez (Cambridge: Cambridge Univ. Press), 219  
 Liu, Y., Liu, X.-W., Barlow, M. J., & Luo, S.-G. 2004a, *MNRAS*, **353**, 1251  
 Liu, Y., Liu, X.-W., Luo, S.-G., & Barlow, M. J. 2004b, *MNRAS*, **353**, 1231  
 Lodders, K. 2010, in *Principles and Perspectives in Cosmochemistry*, ed. A. Goswami & B. E. Reddy (Berlin: Springer), 379  
 Maciel, W. J. 1984, *A&AS*, **55**, 253  
 Mallik, D. C. V., & Peimbert, M. 1988, *RMxAA*, **16**, 111  
 Machado, A., Stanghellini, L., Villaver, E., et al. 2015, *ApJ*, **808**, 115  
 Mata, H., Ramos-Larios, G., Guerrero, M. A., et al. 2016, *MNRAS*, **459**, 841  
 Mathis, J. S., Ruml, W., & Nordsieck, K. H. 1977, *ApJ*, **217**, 425  
 McCarthy, J. K., Mendez, R. H., & Kudritzki, R.-P. 1997, in *IAU Symp. 180, Planetary Nebulae*, ed. H. J. Habing & H. J. G. L. M. Lamers (Dordrecht: Kluwer), 120  
 Miller Bertolami, M. M. 2016, *A&A*, **588**, A25  
 Montez, R., Jr., Kastner, J. H., Balick, B., et al. 2015, *ApJ*, **800**, 8  
 Napiwotzki, R. 1999, *A&A*, **350**, 101  
 Natta, A., & Hollenbach, D. 1998, *A&A*, **337**, 517  
 O'Dell, C. R., Balick, B., Hajian, A. R., Henney, W. J., & Burkert, A. 2002, *AJ*, **123**, 3329  
 O'Dell, C. R., & Handron, K. D. 1996, *AJ*, **111**, 1630  
 O'Dell, C. R., Sabbadin, F., & Henney, W. J. 2007, *AJ*, **134**, 1679  
 Otsuka, M., Kemper, F., Hyung, S., et al. 2013, *ApJ*, **764**, 77  
 Otsuka, M., Meixner, M., Riebel, D., et al. 2011, *ApJ*, **729**, 39  
 Otsuka, M., Tajitsu, A., Hyung, S., & Izumiura, H. 2010, *ApJ*, **723**, 658  
 Parker, Q. A., Bojicic, I., & Frew, D. J. 2016, arXiv:1612.00167  
 Pazderska, B. M., Gawronski, M. P., Feiler, R., et al. 2009, *A&A*, **498**, 463  
 Petrov, L., Hirota, T., Honma, M., et al. 2007, *AJ*, **133**, 2487  
 Phillips, J. P. 2002, *ApJS*, **139**, 199  
 Phillips, J. P., Ramos-Larios, G., & Guerrero, M. A. 2011, *MNRAS*, **415**, 513  
 Pilbratt, G. L., Riedinger, J. R., Passvogel, T., et al. 2010, *A&A*, **518**, L1  
 Puget, P., Stadler, E., Doyon, R., et al. 2004, *Proc. SPIE*, **5492**, 978  
 Rauch, T. 2003, *A&A*, **403**, 709  
 Rauch, T., Kerber, F., Furlan, E., & Werner, K. 2004, in *ASP Conf. Ser. 313, Asymmetrical Planetary Nebulae III: Winds, Structure and the Thunderbird*, ed. M. Meixner et al. (San Francisco, CA: ASP), 296  
 Rouleau, F., & Martin, P. G. 1991, *ApJ*, **377**, 526  
 Sahai, R., Morris, M. R., Werner, M. W., et al. 2012, *A&A*, **542**, L20  
 Schwarz, H. E., & Monteiro, H. 2006, *ApJ*, **648**, 430  
 Shingles, L. J., & Karakas, A. I. 2013, *MNRAS*, **431**, 2861  
 Stanghellini, L., & Haywood, M. 2010, *ApJ*, **714**, 1096  
 Stanghellini, L., Shaw, R. A., & Villaver, E. 2008, *ApJ*, **689**, 194  
 Storey, P. J., & Hummer, D. G. 1995, *MNRAS*, **272**, 41  
 Tajitsu, A., & Tamura, S. 1998, *AJ*, **115**, 1989  
 Turner, J., Kirby-Docken, K., & Dalgarno, A. 1977, *ApJS*, **35**, 281  
 Ueta, T., Ladjal, D., Exter, K. M., et al. 2014, *A&A*, **565**, A36  
 Umama, G., Leto, P., Trigilio, C., et al. 2008, *A&A*, **482**, 529  
 van der Tak, F. F. S., Black, J. H., Schöier, F. L., Jansen, D. J., & van Dishoeck, E. F. 2007, *A&A*, **468**, 627  
 van Hoof, P. A. M., van de Steene, G. C., Barlow, M. J., et al. 2010, *A&A*, **518**, L137  
 Vassiliadis, E., & Wood, P. R. 1993, *ApJ*, **413**, 641  
 Vassiliadis, E., & Wood, P. R. 1994, *ApJS*, **92**, 125  
 Villaver, E., Machado, A., & García-Segura, G. 2002, *ApJ*, **581**, 1204  
 Weinberger, R. 1989, *A&AS*, **78**, 301  
 Zuckerman, B., Kastner, J. H., Balick, B., & Gatley, I. 1990, *ApJL*, **356**, L59